Cerebellar Structure Segmentation and Shape Analysis with Application to Cerebellar Ataxia

Zhen Yang

A dissertation submitted to the Johns Hopkins University
in conformity with the requirements for the Doctor of Philosophy

Baltimore, Maryland

October 2015

Abstract

The cerebellum plays an important role in motor control and cognitive functions. Cerebellar dysfunction can lead to a wide range of movement disorders. Despite the significant impact on the lives of patients, the current standard of diagnosis, prognosis, and treatment for cerebellar disease is limited. Magnetic resonance (MR) imaging based morphometric analysis of the cerebellum, which studies the brain structural pattern associated with disease and functional decline, is of great interest and importance. It sets the stage for developing disease-modifying therapies, monitoring individual patient progress, and designing efficient therapeutic trials. Compared to the cerebrum, morphometric analysis in the cerebellum has been limited. Automated and accurate volumetric analysis techniques are lacking. Methods using MR based morphometric biomarkers to predict disease type and functional decline have been lacking or inconclusive. The work presented in this thesis is motivated by the need for better cerebellar structure segmentation and effective structure-function correlation and prediction methods in cerebellar disease.

The thesis makes four major contributions. First, we proposed an automated method for segmenting cerebellar lobules from MR images. The proposed method achieved better performance than two state-of-the-art segmentation methods when validated on a cohort of 15 subjects including both healthy controls and patients with various degrees of cerebellar atrophy. Second, we presented two highly-informative shape representations to characterize cerebellar structures: a landmark shape representation of the collection of cerebellar lobules and a level set based whole cerebellar shape representation. Third, we developed an analysis pipeline to classify healthy controls and different ataxia types and to visualize disease specific cerebellar atrophy patterns based on the proposed shape representations and high-dimensional pattern classification methods. The classification performance is evaluated on a cohort consisting of healthy controls and different cerebellar ataxia types. The visualized cerebellar atrophy patterns are consistent with the regional volume decreases observed in previous studies in cerebellar ataxia. Compared to existing analysis methods, the proposed method provides intuitive and detailed visualization of the differences of overall size and shape of the cerebellum, as well as that of individual lobules. Fourth and the last, we developed and tested a similar analysis pipeline for functional score prediction and function specific cerebellar atrophy pattern visualization.

The thesis was prepared under the direction of Dr. Jerry L. Prince.

Acknowledgments

First and foremost, I would like to thank my adviser, Dr. Jerry L. Prince. Over the past six years, he encouraged me with his passion, guided me with his insights, and helped me through the struggles. He is the professor I have met that has the most patience and thinks most for the student. He taught me how to be a researcher by his own example and his influence on me is not only academic, but also on many other aspects of life and career. It is my great fortune and honor to pursue my degree under his supervision.

I would also like to thank Dr. Sarah H. Ying, who has great passion for ataxia research and genuine care for ataxia patients. She helped my research with her insights on the clinical side. And Dr. Bruno M. Jedynak for his expertise in statistics and machine learning.

I would like to thank my committee members: Dr. Jerry L. Prince, Dr. Trac. D. Tran, Dr. Mounya Elhilali for their time and effort. Especially Dr. Tran, who has been my course instructor, department qualification exam committee member, proposal committee member, and now defense committee member.

I would like to thank all the current and former members of the brain group—Dr. John Bogovic, Dr. Min Chen, Dr. Chuyang Ye, Mr. Amod Jog, Mr. Murat Bilgel, Dr. Snehashis Roy, Dr. Navid Shiee, Ms. Ezgi Ergun, Dr. Blake Lucas, Mr. Mazy Abulnaga for their collaboration, help and suggestions; Dr. Xiaodong Tao, Dr. Duygu Tosun and Dr. Maryam E. Rettmann, for their inspiring works and writings. I would like to thank all other members of the Image Analysis and Communication Lab—Mr. Fangxu Xing, Mr. Andrew Lang, Dr. Bhavna Antony, Dr. David A. Gomez, Dr. Xiaofeng Liu, Dr. Sahar Soleimanifard, Ms. Maria Ayad, Dr. Harsh Agarwal, Dr. Nathanael Kuo for their friendship that has made my graduate study so enjoyable. I would especially like to thank Mr. Aaron Carass, without whom the lab cannot function properly even for a single day, for all his help on everything I do in the lab; and Laura Granite for managing the logistics, for her kindness and patience.

I owe heartfelt thanks to my family back home, for all that they have done for me.

Over the years, they are always there to cheer for my achievements and cushion my falls, without complaining the very short days I could spend with them. My grandpa passed away without me by his side. I want to dedicate this thesis to my parents and my grandpa.

Contents

List of Figures

List of Tables

Chapter 1

Introduction

1.1 Motivation

The cerebellum plays an important role in motor control [1, 2] and is also involved in regulation of cognition and emotion [3, 4]. Cerebellar dysfunction can lead to a wide range of movement disorders including a lack of coordination, reduced manual dexterity, postural instability, and gait disturbances [5]. Despite the significant impact on the lives of patients, the current standard of diagnosis, prognosis, and treatment is inadequate [6,7]. Magnetic resonance (MR) imaging provides the potential to improve our understanding of cerebellar neurodegeneration by revealing structural changes in the cerebellum. Figure 1.1 shows example coronal sections of the cerebellum from a healthy control and subjects with spinocerebellar ataxia type 2 (SCA2), spinocerebellar ataxia type 6 (SCA6), and ataxia-telangiectasia (AT). We can see that all of the three ataxia types show cerebellar atrophy relative to the healthy control. However, SCA2 shows significant atrophy of the corpus medullare (central white matter of the cerebellum and the deep cerebellar nuclei) while SCA6 shows more atrophy in the posterior-inferior regions of the cerebellum. It is of great interest to study the cerebellar structural pattern associated with specific disease type and functional decline, and to quantify the correlation between cerebellar structural change with functional decline. On the scientific side, it helps researchers further understand the localized function map of the cerebellum. On the clinical side, it sets the stage for developing

disease-modifying therapies, monitoring individual patient progress, and designing efficient therapeutic trials.

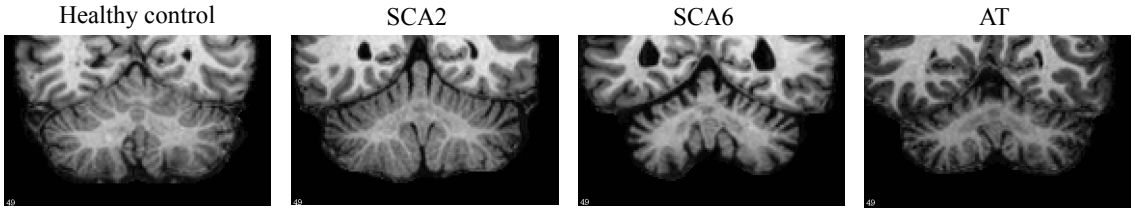

Figure 1.1: Example coronal sections of the cerebellum from HC and three ataxia types.

MR image based brain morphometric analysis has been successfully established as a tool for the differential diagnosis and for disease progression prediction of Alzheimer's disease [8–10], Huntington's disease [11–13], and several other neurodegenerative diseases, with most of the studies done on cerebrum structures. Compared to the cerebrum, literature on the morphometric analysis in the cerebellum is much more limited due to the relatively smaller population affected.

In this work, we focus on morphometric analysis of the cerebellum in cerebellar ataxia, with special focus on: 1) developing an automated and accurate method for segmenting fine anatomical divisions of the cerebellum; 2) exploring highly informative representation of the cerebellar structures; 3) predicting ataxia types and functional declines based on the highly informative representations, and 4) identifying disease and function specific cerebellar atrophy patterns.

1.2 Anatomy and function of the cerebellum

The cerebellum is located at the back of the brain, below the posterior part of the cerebrum and behind the top part of the brain stem (see Figure 1.2(a)). The cerebellum is divided into two hemispheres connected by a narrow midline zone (see Figure 1.2(b)). The cerebellum consists of a tightly folded layer of gray matter cortex and a central mass of white matter, called the corpus medullare. Fissures divide the cortex into small branches called lobules, numbered from I to X [14]. The most

prominent fissures define the boundaries of the lobes of the cerebellum. Lobules I–V form the anterior lobe, VI–VII form the middle lobe, and VIII–X form the caudal lobe. Figure 1.3 shows MR image of the cerebellum and manually labeled regions with their names overlaid on MR images. Figure 1.4 shows a surface rendering of the cerebellar lobules, lobes, and primary fissures.

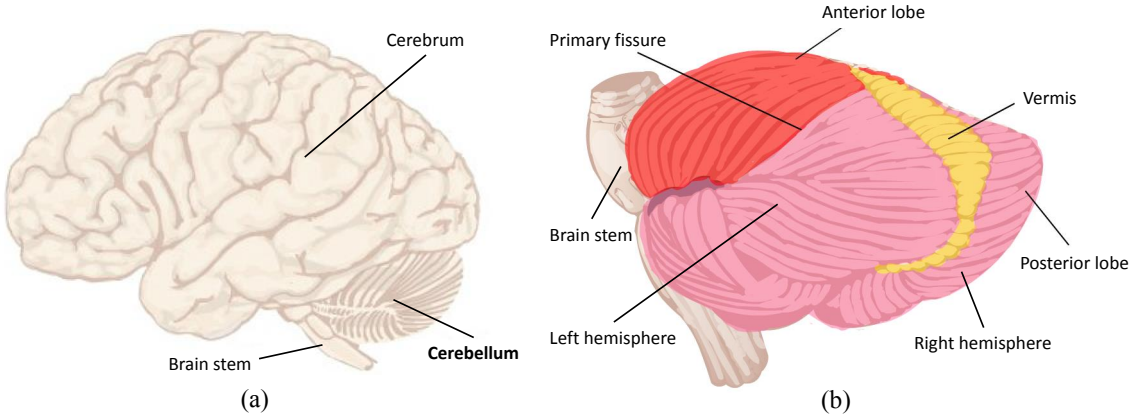

Figure 1.2: The cerebellum. (a) Location of the cerebellum; (b) Gross anatomy of the cerebellum. Image courtesy of James Knierim Neuroscience Online Section 3 Chapter 5: Cerebellum (http://neuroscience.uth.tmc.edu/s3/chapter05.html).

The cerebellum is most understood in terms of its contributions to motor control, including maintenance of balance and posture, coordination of voluntary movements, and motor learning. It is also involved in certain cognitive functions, such as language and emotion regularization. The cerebellar motor and cognitive functions are topographically organized, as revealed by functional magnetic resonance imaging (fMRI) studies [15–20]. These studies suggest that the anterior lobe and intermediate parts of posterior lobe are related to motor and somatosensory functions, whereas the lateral posterior cerebellum is related to cognitive functions. Whether similar regional structural atrophy pattern correlates with specific function loss in cerebellar diseases remains unknown.

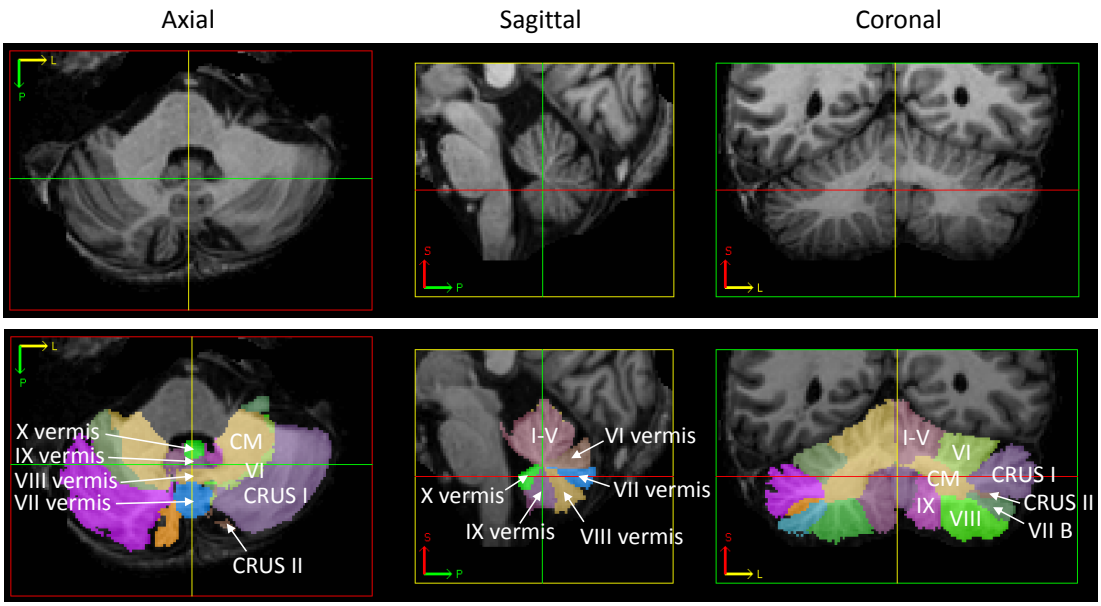

Figure 1.3: Annotated examples of the cerebellar lobules in three different views. The top and bottom rows are MR images overlaid with expert delineated lobules from a healthy control and an ataxia patient, respectively.

1.3 Cerebellar ataxia

Ataxia typically refers to the lack of coordinated movements. It describes symptoms without reference to specific diseases. Cerebellar ataxia is a form of ataxia originating in the cerebellum [6, 7]. Cerebellar ataxia can occur as a result of many diseases and has symptoms of an inability to coordinate balance, gait, and eye movements. The cause of cerebellar ataxia can be: 1) inherited, which means they are caused by a defect in a certain gene that is present from the start of a person's life; 2) acquired,

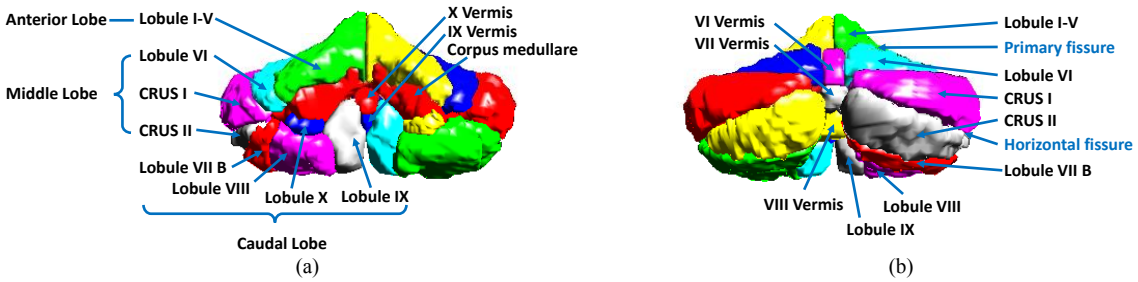

Figure 1.4: Surface rendering of cerebellar lobules and lobes. (a) Anterior view; (b) Posterior view.

e.g., from injury, diseases and toxic; 3) idiopathic, e.g., cerebellar form of multiple system atrophy.

The diagnostic approaches to cerebellar ataxia include checking medical history, family history of neurological problems, neurological examinations, blood tests to rule out other diseases and toxins, MR scan of the brain, and other tests [21]. Genetic blood tests are available for some types of hereditary ataxia to determine if someone has inherited an ataxia gene that affected other family members. For clinical assessment of the severity of ataxia, the International Cooperative Ataxia Rating Scale (ICARS) [22] and the Scale for the Assessment of Ataxia (SARA) [23] have been validated.

Although scientific and clinical studies on cerebellar ataxia have made significant progress, the research has not yet led to new effective therapies. Etiological treatment approaches are available only for some rare forms of ataxia with known biochemical defects. For most other types of hereditary and non-hereditary ataxia, only supportive treatment is possible.

The major disease types being studied in this work are spinocerebellar ataxia (SCA). SCA is a progressive, degenerative, genetic disease with multiple types, each of which could be considered a disease in its own right. An estimated 150,000 people in the United States are diagnosed with SCA. There is no known effective treatment or cure. Since SCA has multiple genetic versions, each with a characteristic pattern of anatomical degeneration that yields distinctive motor and cognitive problems, it provides a rich source to study the relationships between cerebellar structure and function.

1.4 Brain morphometric analysis review

Region of interest (ROI) volumetric analysis has been traditionally used to investigate the structural changes of the brain and is still now one of the most intuitive and reliable methods for structural analysis [8, 24–36]. In ROI volumetric analysis, a number of well-defined ROIs are delineated, and the volumes of these ROIs are statistically analyzed. Manual ROI delineation remains the gold standard, but it is very

time-consuming and requires specialized anatomical expertise and training to ensure accuracy and to prevent rater-dependent bias. These limitations might be overcome by automated methods to identify ROIs [37–39]. Another limitation of ROI-based analysis is that the ROI must be defined in advance, while in practice it is often the case that the regions affected by the disease are not known. Moreover, the disease might affect only part of a well-characterized anatomical region.

Voxel-based morphometry (VBM) gained popularity in the last two decades [9, 40–50]. VBM methods are based on a spatial transformation that map the subject images into a standard space, followed by a voxel-wise statistical analysis of the spatial distribution of different tissue types [40, 45], of the properties of the spatial transformation itself [51, 52], or of combined measurements of the residual image and the spatial transformation [43]. VBM can identify regions in which two groups differ (e.g., patients and healthy controls) or regions in which other variables (e.g., age, gender, disease severity) correlate with image based measurements. Compared with ROI volumetric analysis, VBM avoids pre-defining and delineating of ROIs and provide more localized morphometric information. However, VBM depends on the artificial deformation field between two subjects obtained by the registration algorithm, different registration algorithms give different results. Also, the amount of smoothing used to compensate for the registration error and increase statistical power of the analysis also affects the result. Both ROI volumetry and VBM employ mass univariate analysis. They have limited ability in identifying complex population differences because they do not take into account the multivariate relationships in the data [53]. Regions showing significant group difference are not necessarily good discriminatory factors at the individual level in prediction tasks.

With the development of machine learning algorithms capable of dealing with high-dimensional data, pattern classification methods have been recently proposed for morphological analysis [10, 54–62]. These methods typically take as input features the voxel-wise measurement as that used in VBM. They aim to capture multivariate relationships in the data and can achieve high classification accuracy on individual subjects. A challenge for these methods is that the training samples in medical

research are often insufficient compared to the high dimensionality of the data, dimension reduction like principal component analysis (PCA) [63–65], and nonlinear manifold learning [66–70] is carried out before any analysis. Then machine learning algorithms like linear discriminant analysis (LDA) [71], logistic regression [72, 73], support vector machine (SVM) [74], decision trees [75, 76], and ensemble learning methods [77, 78] are used to perform classification (e.g., predict disease type) or regression tasks (predict functional loss).

Statistical shape analysis also plays an important role in brain morphological analysis [79–95], where geometric outline of the anatomical structure is encoded in a vector and statistical learning methods are designed to study the population distribution in high-dimensional shape space. A very widely used representation is that of homologous landmarks located on the boundary (a closed contour in 2D case and closed surface in 3D case) of the object. Since shape representations try to capture all the geometrical information that remains after removing location, scale, and rotational effects [96], they provide more morphological information than local volume changes as in ROI and VBM analysis. For example, VBM cannot reflect the bending of an elongated shape. Since shape representation form a linear space, it can synthesize and visualize plausible instances in shape space. One challenge in applying shape analysis to the brain is to establish corresponding geometry across subjects in a population, which is difficult due to the complex geometry of anatomical structures and the large inter-subject variability. Current shape analysis methods are often applied to structures with simple geometry, e.g., brain sub-cortical structures.

Compared to the cerebrum, literature on the morphometric analysis in the cerebellum is much more limited due to the relatively smaller population affected. ROI volumetric analysis have been applied [31, 33, 97–104], but they were only performed with low numbers of affected individuals or evaluated on gross anatomical divisions (due to the lack of accurate volumetric analysis techniques for finer ROIs). VBM analysis have been applied [105–109], but methods using MR based morphometric biomarkers to predict clinical dysfunction or disease progression have been lacking or inconclusive.

1.5 Thesis contributions

The major contributions of this thesis are summarized as follows:

1. We propose an automated method for segmenting cerebellar lobules from MR images (see Chapter 2). There are few works on segmenting fine sub-structures of the cerebellum, especially ones validated on both healthy and diseased subjects. The method described in this thesis combines multi-atlas label fusion result and tissue/boundary classification in a graph cut segmentation framework. The multi-atlas component ensures the correct localization of different lobules, and tissue/boundary classification promotes accurate delineation of lobule boundaries. The proposed method is assessed on a cohort of 15 subjects, including both healthy controls and patients with various degrees of cerebellar atrophy, for which expert manual labels are also available. The method was further validated on a larger cohort containing both normal controls and patients experiencing cerebellar ataxia. Quantitative analysis of the lobule volumes show distinct patterns of volume changes associated with different SCA subtypes consistent with known patterns of atrophy in these genetic subtypes.

2. We propose two shape representations to characterize cerebellar structures (see Chapter 3). First, we propose a landmark shape representation of the collection of cerebellar lobules. This highly informative feature representation of the cerebellar structure is constructed by extracting dense homologous landmarks on the boundary surfaces of cerebellar sub-structures. We addressed the difficulty in establishing dense corresponding points on multiple 3D objects across subjects by a two-step non-rigid point set registration. Second, we propose a level set based shape representation. This representation is easy to generate (only a cerebellar tissue segmentation is needed, followed by a signed distance transform) and unique (no artificial non-rigid alignment involved as in VBM and landmark shape representation). We demonstrated the representational power of the proposed shape representations by studying the shape variations of different populations. We also compared the proposed shape representations with

existing morphometric measures like ROI volumes and RAVENS maps in disease classification and functional score regression to evaluate their discriminant power (see Chapters 4 and 5).

3. We present a shape analysis pipeline to classify healthy controls and different ataxia types and to visualize the characteristic cerebellar atrophy patterns for different ataxia types. Linear dimension reduction is applied to reduce the high-dimensional shape representation to a low-dimensional feature vector. A classifier is built in the dimension-reduced space to predict disease types. Characteristic atrophy pattern for an ataxia type is visualized by sampling along the discriminant direction between healthy controls and the ataxia type. Experimental results show that the proposed method can successfully classify healthy controls and different ataxia types. The visualized cerebellar atrophy patterns were consistent with the regional volume decreases observed in previous studies in cerebellar ataxia. Compared to existing analysis method, the proposed method provides an intuitive and detailed understanding about changes of overall size and shape of the cerebellum as well as that of individual lobules.

4. We present a shape analysis pipeline to predict functional scores and to visualize the function specific atrophy patterns. Similar to discriminant analysis, linear dimension reduction is applied to generate a low-dimensional feature vector. A regressor is built in the dimension-reduced space to predict functional scores. Functional specific atrophy patterns are visualized by sampling along the regression line. The visualized function specific atrophy patterns partially agree with a previous study on the topological organization of cerebellar functions.

We note that parts of this thesis have been previously published or submitted as conference and journal papers [110–112].

1.6 Thesis organization

The remainder of the thesis is organized as follows:

In Chapter 2, we review the literature on cerebellar structure segmentation and describe the proposed automated cerebellar lobule segmentation method. We tested the method on 15 subjects with expert labels and compared the performance with two state-of-the-art segmentation methods. We further validated the method on a larger cohort containing both normal controls and patients experiencing cerebellar ataxia.

In Chapter 3, we first review the background on shape modeling and then present two shape representations to characterize cerebellar structures: a landmark shape representation of the collection of cerebellar lobules and a level set based whole cerebellar shape representation. We study the cerebellar shape variations of different populations using the two shape representations.

In Chapter 4, we present the shape analysis pipeline to classify healthy controls and different ataxia types, and to visualize the characteristic cerebellar atrophy pattern. We tested the classifer on a data set with healthy controls, four spinocerebellar ataxia subtypes and ataxia-telangiectasia, and compared the performance of different cerebellar structural representations. We also compared the visualized cerebellar atrophy patterns with regional volume decreases observed in previous studies in cerebellar ataxia.

In Chapter 5, we present a shape analysis pipeline to predict functional scores and to visualize the function specific atrophy patterns. We tested the classifer on a data set with healthy controls, four spinocerebellar ataxia subtypes and ataxia-telangiectasia, and compared the performance of different cerebellar structural representations. We also compared the visualized function specific atrophy patterns with previous studies on the topological organization of cerebellar functions.

In Chapter 6, we summarize the work in this thesis and point out some future research directions.

Chapter 2

Cerebellar Lobule Segmentation

In this chapter, we present a new method for segmenting and labeling the cerebellar lobules from MR images. Pronounced regional cerebellar atrophy is known to occur in the spinocerebellar ataxias (SCAs) [97,101,104], while more subtle regional cerebellar atrophy has been observed in several other neurological diseases such as Parkinson's disease [113,114], Huntington's disease [115,116], Alzheimer's disease [117], and multiple sclerosis [118]. Accurate delineation of the cerebellum as a whole as well as further parcellation into lobes and lobules can be used to better understand cerebellar structural change and to diagnose and monitor disease. The purpose of the proposed method in this thesis is two-fold. First, it will be used for ROI volumetric analysis in differentiating different SCA types in Section 2.4.3; Second, it will be used for constructing a highly informative structural representation of the cerebellum in Chapter 3.

The remainder of this chapter is organized as follows: in Section 2.1, we review the literature on cerebellar structure segmentation and bring forward the idea behind the proposed algorithm; in Section 2.3, we describe the proposed automated cerebellar lobule segmentation method; in Section 2.4.2, we describe our testing of the method on 15 subjects with expert labels and we show a comparison of the performance with two state-of-the-art segmentation methods; in Section 2.4.3, we show results of applying the method on a larger cohort containing both normal controls and patients experiencing cerebellar ataxia.

2.1 Related works

Although the cerebellum has a fairly regular structure [14]—known, in particular, to be less variable than the cerebrum [119]—it nevertheless remains challenging for both manual raters and automatic algorithms to consistently and reliably label the parts of the cerebellum from magnetic resonance (MR) images. For example, experts (requiring thousands of hours of training), take 50–60 hours to label the whole cerebellum, its lobes, and its lobules [120]. Although time and cost can both be reduced by using multiple inexpert raters [120], the time and effort still remains considerable, and consistency of the results across different sets of raters may be poor.

Various automated methods such as FreeSurfer [121], TOADS [122], and others [123] provide a cerebellum segmentation result as part of their whole-brain segmentation method. These methods typically provide a whole cerebellum segmentation and also segment its gray matter (GM) and white matter (WM). Several specialized methods for segmenting just the cerebellum itself have also been developed; one method uses atlas registration and local image descriptors [124] and another uses an active contour model with a shape prior [125].

For a parcellation of the cerebellum into lobes and lobules, atlas based methods are typically used. In these methods one or more atlas brains are registered to the subject to be segmented and the atlas labels are transferred to the subject brain. Diedrichsen et al. (2006) [126] developed a spatially unbiased atlas template of the human cerebellum (SUIT) and later revised it with a probabilistic atlas [127]. Multi-atlas methods reduce the bias towards a specific atlas, and have been shown to be effective when combined with various label fusion strategies [128–130]. However, the accuracy of multi-atlas methods are limited by the quality of the registration result, which is in turn affected by the difference in cerebellar geometry of the atlas and subject. Cerebellar parcellation of subjects with extreme atrophy can therefore be expected to be poor when using these approaches, which is undesirable for quantitative analysis of group structural differences or studying structural-functional correlations. Various label fusion strategies have been proposed to solve these problems in different seg-

mentation tasks [131–134] including segmenting cerebellar sub-structures [135]. There has been few studies containing both healthy controls and patients with cerebellar atrophy. Bogovic et al. proposed ACCLAIM (Automatic Classification of Cerebellar Lobules Algorithm using Implicit Multi-boundary evolution) [136], which used a multi-object geometry deformable model driven by random forest boundary classification. The method demonstrated superior performance in comparison to the SUIT atlas-based labeling method and a multi-atlas label fusion approach [128], and was shown to perform well on both healthy controls and cerebellar ataxia patients.

The new method described here combines multi-atlas label fusion result and tissue/boundary classification in a graph cut segmentation framework. In particular, the multi-atlas and tissue classification results together determine the region terms in the graph cut energy function while the boundary classifier determines a boundary term in the energy function. The multi-atlas component ensures the correct localization of different lobules, and tissue/boundary classification promotes accurate delineation of lobule boundaries.

2.2 Atlases and image preprocessing

The method use a set of subjects as atlases (or training subjects). This set of subjects was manually delineated by an expert with over 5000 hours of training using the protocol described in Bogovic et al. (2013) [120]. The MR images of both the atlas subjects and the subject to be segmented are preprocessed using FreeSurfer version 5.3.0 [121]. As part of this procedure, each MR scan is transformed into MNI (Montreal Neurological Institute) space [137, 138] and a skull-stripped and intensity normalized image I_s is generated along with an initial tissue classification of the cerebellum into gray matter (GM) and white matter (WM). I_s is cropped to contain only the cerebellum, and the cropped image I was used in all subsequent processing. For the atlas subjects with manually delineated labels, the labels are transformed from the native image space into the same space as the preprocessed images so that the images and their corresponding manual labels are aligned.

2.3 Graph cut segmentation framework

Let $\mathbf{x} \in \Omega$ be a voxel location in a set of discrete voxel locations Ω in the image domain. An image segmentation is a label assignment $A(\mathbf{x})$ that maps each voxel location $\mathbf{x}$ to an integer label $k \in \{0, 1, 2, \ldots, K\}$. In our formulation, 0 represents background and each non-zero integer represents a finest-grain anatomical structure (see Section 1.2). The number of structures to be segmented is 26 (i.e., $K = 26$).

Graph cut methods [139,140] are widely used in various image segmentation tasks for their robustness and accuracy. It casts the energy-based image segmentation problem in a graph structure and finds the optimal solution by efficient min-cut algorithms. A typical graph cut energy function $E(A)$ includes a region term (unary potential) and a boundary term (pairwise potential), both of which are evaluated a given the label assignment $A(\mathbf{x})$. In our approach, the graph cut energy function is formulated as

$$E(A) = \lambda_l \overbrace{\sum_{\mathbf{x}\in\Omega} R_l(\mathbf{x}, A(\mathbf{x}))}^{\text{Lobule region term}} + \lambda_c \overbrace{\sum_{\mathbf{x}\in\Omega} R_c(\mathbf{x}, A(\mathbf{x}))}^{\text{Cerebellum region term}} + \overbrace{\sum_{\substack{(\mathbf{x},\mathbf{y})\in\Gamma \\ A(\mathbf{x})\neq A(\mathbf{y})}} B(\mathbf{x}, \mathbf{y})}^{\text{Boundary term}}, \tag{2.1}$$

where the constants λ_l and λ_c weight the two region terms relative to the boundary term. Γ is the set of all unordered 26-connected neighborhood voxel pairs. The lobule region term $R_l(\mathbf{x}, A(\mathbf{x}))$ specifies the cost of assigning a lobule label $A(\mathbf{x})$ to a voxel $\mathbf{x}$. It is computed based on the multi-atlas labeling result, and controls the overall shape of the final segmentation. The cerebellum region term $R_c(\mathbf{x}, A(\mathbf{x}))$ specifies the cost of assigning cerebellar ($A(\mathbf{x}) \neq 0$) or non-cerebellar label ($A(\mathbf{x}) = 0$), i.e., background, to a voxel $\mathbf{x}$. It is computed based on a cerebellar tissue classification result and aims to refine the lobule-background boundary. The boundary term $B(\mathbf{x}, \mathbf{y})$ specifies the cost of assigning a pair of neighboring voxels $(\mathbf{x}, \mathbf{y})$ with different lobule labels. It is computed using a boundary voxel classification result and it refines both the lobule-lobule and the lobule-background boundaries. The definition of these energy terms, which we will describe in detail in the following sections, is the key to a good

segmentation.

For this multiple label assignment problem, we use the α-expansion optimization strategy [139, 140] which successively segments all α and non-α voxels (where α represents a particular label) using the max-flow/min-cut algorithm and then iterates over each label (assigned as the α label) until the label assignments converge.

Figure 2.1 shows the diagram of the method. First the MR image is preprocessed as described in Section 2.2. Then, multi-atlas registration and label fusion is carried out to obtain both an initial segmentation of the cerebellum and the lobule region term. Tissue classification is performed to obtain the cerebellum region term and boundary classification is performed to obtain the boundary term. Finally, the graph cut energy function is minimized to produce the final segmentation result. In the following subsections, we describe in detail the specification and computation of each energy term in our graph cut formulation.

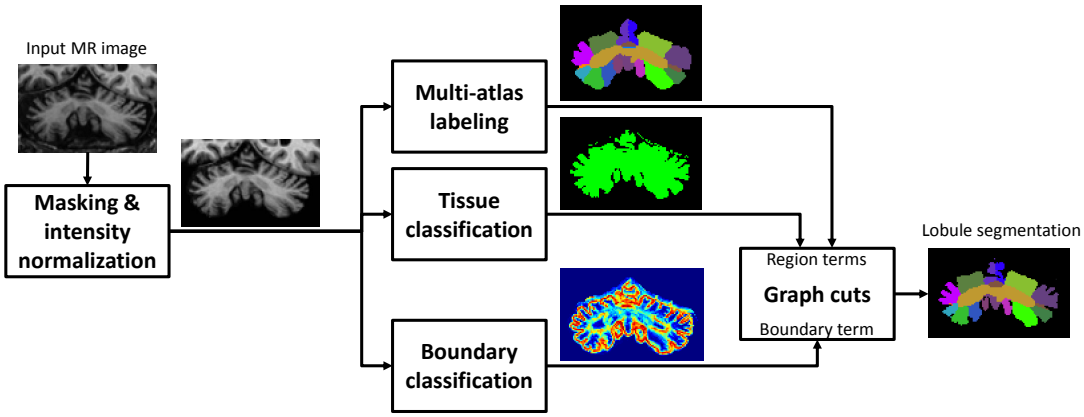

Figure 2.1: Diagram of the proposed algorithm.

2.3.1 Lobule region term

In this section, we define an energy term $R_l(\mathbf{x}, A(\mathbf{x}))$, which ideally yields a smaller cost when voxel $\mathbf{x}$ is assigned the correct label $A(\mathbf{x})$. We derive the necessary information to define this energy term from a multi-atlas labeling result that is carried out as another preprocessing step. Multi-atlas labeling methods register a set of labeled

images to the test subject, transfer their labels, and then decide on a single label at each voxel given the set of transferred labels. Various approaches have been proposed for label fusion—e.g., majority voting [141], similarity weighted voting [130, 142, 143], and statistical fusion [128, 144, 145]. Statistical methods like STAPLE [128] and its variants [144, 145] integrate a model of rater behavior, and are among the very best performers in the label fusion task. In this work, we use the non-local STAPLE (NL-STAPLE) algorithm proposed by Asman et al. (2013) [133]. NL-STAPLE models the registered atlases as collections of volumetric patches containing both intensity and label information. It uses the non-local criteria [143, 146] to improve results that are otherwise flawed by imperfect registration results.

Each atlas is made up of a preprocessed image I together with a registered expert delineation. To carry out multi-atlas labeling, each of the atlas images is deformably registered to the subject image using the symmetric image normalization method (SyN) [147] implemented in the Advanced Normalization Tools (ANTS) [148]. We use mean square intensity difference as the similarity term in registration. The optimization in registration is performed over two resolutions with a maximum of 10 iterations at the coarse level and 10 at the full resolution. The atlas label is transformed to the subject space using the corresponding deformation field. The transformed labels from all atlases are then fused using NL-STAPLE to produce $A_m(\mathbf{x})$, a multi-atlas subject label.

This multi-atlas labeling result represents a state-of-the-art cerebellar segmentation result by itself, but here we use it as a preprocessing step to help specify the lobule region term in our graph cut energy. In particular, given the multi-atlas label result $A_m(\mathbf{x})$ we define the lobule region term as

$$R_l(\mathbf{x}, A(\mathbf{x})) = \min_{\mathbf{y} \in \Phi_{A(\mathbf{x})}} \|\mathbf{x} - \mathbf{y}\|, \tag{2.2}$$

where $\Phi_l = \{\mathbf{y} \in \Omega \,|\, A_m(\mathbf{y}) = l\}$ is the region labeled l in the multi-atlas labeling result. Evaluated at each voxel $\mathbf{x}$, the term $R_l(\mathbf{x}, A(\mathbf{x}))$ yields the distance to region $\Phi_{A(\mathbf{x})}$, the region with the same label as that of $\mathbf{x}$ in the multi-atlas labeling result. If

the label at $\mathbf{x}$ actually agrees with the multi-atlas label at $\mathbf{x}$, then the cost $R_l(\mathbf{x}, A(\mathbf{x}))$ is zero. The cost grows larger as $\mathbf{x}$ grows farther away from $\Phi_{A(\mathbf{x})}$. Consequently, this lobule region term encourages the final segmentation result to agree with the multi-atlas labeling result.

2.3.2 Cerebellum region term

Neither FreeSurfer nor multi-atlas labeling provides accurate boundary between the cerebellar and non-cerebellar region. FreeSurfer consistently underestimates the cerebellum region, i.e., it labels cerebellar lobule voxels as background. Multi-atlas labeling, on the other hand, tends to over-estimate the cerebellum region, i.e., it labels background voxels as cerebellar lobule voxel, especially when the cerebellum has experienced atrophy, such as that which occurs in spinocerebellar ataxia. This occurs even when atrophied cerebella are included among the atlases used to provide the multi-atlas segmentation result. A better result can be achieved by directly carrying out a cerebellum segmentation step. Several approaches for whole cerebellum segmentation have been proposed [123, 125]. To differentiate cerebellum from non-cerebellum, these methods typically use intensity and texture information together with prior information about the position and shape of the cerebellum. In our work, both image and spatial information are used to train a voxelwise cerebellar tissue classifier. This result is then used to define the cerebellum region term in our graph cut energy function.

Two types of features are used to distinguish cerebellar voxels from non-cerebellar voxels in a preprocessed image I. The first type of features are image features including the intensity, the magnitude of the image gradient, and the trace and determinant of the Hessian matrix of the intensity. The second type of features are spatial features including the spatial coordinates relative to the centroid of the estimated corpus medullare (CM) and the signed distance of the voxel to the boundary of the estimated CM. The estimated CM is obtained by applying a morphological opening operation (using a circular structuring element of diameter 5 pixels) to the cerebellar WM mask obtained from the FreeSurfer segmentation result. This opening operation removes

WM branches inside the lobules, yielding a better estimate of the CM. A feature vector $\mathbf{u}(\mathbf{x})$ comprising the values of these eight features is constructed for each voxel $\mathbf{x}$.

We use random forests [149] to perform the classification of cerebellar and non-cerebellar voxels given the feature vector $\mathbf{u}(\mathbf{x})$. Random forests have been shown to achieve robust and accurate classification while avoiding over-fitting [149]. To form the training samples, voxels were sampled from the two classes, cerebellar and non-cerebellar tissue, among the images of the training subjects (which are the same set of labeled subjects used in the multi-atlas segmentation step described in Section 2.3.1). To generate the training samples, 1000 voxels were randomly sampled from each class of each subject. For the random forest configuration, an ensemble of 500 decision trees were constructed, and each decision node within a decision tree used a random subset of two of the eight input features.

Let $A_c(\mathbf{x})$ be the class output by the random forest classifier at voxel $\mathbf{x}$ where $A_c(\mathbf{x}) = 1$ represents a cerebellar voxel and $A_c(\mathbf{x}) = 0$ represents a non-cerebellar (background) voxel. We use this to define the cerebellum region term used in our graph cut energy as follows

$$R_c(\mathbf{x}, A(\mathbf{x})) = \begin{cases} \min_{\mathbf{y}\in\Psi_0} \|\mathbf{x}-\mathbf{y}\|, & \text{if } \; A(\mathbf{x}) = 0 \\ \min_{\mathbf{y}\in\Psi_1} \|\mathbf{x}-\mathbf{y}\|, & \text{if } \; A(\mathbf{x}) \neq 0 \end{cases}, \tag{2.3}$$

where $\Psi_0 = \{\mathbf{y} \in \Omega \,|\, A_c(\mathbf{y}) = 0\}$ is the region classified as non-cerebellum by the random forest classifier and $\Psi_1 = \{\mathbf{y} \in \Omega \,|\, A_c(\mathbf{y}) = 1\}$ is the region classified as cerebellum. The cerebellum region term $R_c(\mathbf{x}, A(\mathbf{x}))$ acts in a fashion very similar to the lobule region term $R_l(\mathbf{x}, A(\mathbf{x}))$ in that it penalizes labels that disagree with the preliminarily estimated labels (in this case by the random forest classifier) by the distance from the region with an agreeing label. For example, if the label $A(\mathbf{x})$ is a cerebellar lobule label (i.e., $A(\mathbf{x}) \neq 0$) and the random forest classifies $\mathbf{x}$ as cerebellar voxel (i.e., $A_c(\mathbf{x}) = 1$) then the cost for $\mathbf{x}$ is zero. However, if $A(\mathbf{x})$ is a cerebellar lobule label but the random forest classifies $\mathbf{x}$ as a non-cerebellar voxel (i.e., $A_c(\mathbf{x}) = 0$), the cost is non-zero and increases with its distance to Ψ_1, the region classified as

cerebellum by the random forest classifier. In this way, when this cost is included in the graph cut energy, as in Equation (2.1), the final labeling is encouraged to agree with the random forest classification of cerebellar and non-cerebellar tissue.

2.3.3 Boundary term

A boundary term is used to further refine the lobule boundaries. Lobule boundaries are typically characterized by high image gradients (at boundaries between lobule and non-cerebellar tissue) or high second order directional derivatives (at boundaries between different lobules). In order to encourage our graph cut segmentation algorithm to make cuts that favor such boundaries between labels, we trained another random forest classifier to identify boundary voxels, including both lobule-background and lobule-lobule boundaries.

The same input feature vector $\mathbf{u}(\mathbf{x})$ as in Section 2.3.2 is used, and the same set of atlas images as the multi-atlas segmentation algorithm was used in training. A multiclass classifier was trained to output the class label $k \in \{1, 2, 3\}$. $k = 1$ indicates a boundary voxel, defined as any voxel having any neighboring voxel (within a 26-voxel neighborhood) with a different label. So a boundary voxel can lie between any pair of lobules or between a lobule and the background. $k = 2$ indicates a lobule voxel, which is a cerebellar (non-background) voxel that is not a boundary voxel, and $k = 3$ indicates a non-cerebellar (background) voxel that is not a boundary voxel. A random forest classifier with the same configuration as in Section 2.3.2 was trained. The training samples were formed by sampling 1000 voxels from each class on each training subject. As before, 500 decision trees were used and each decision node considered a random subset of two of the eight input features.

Rather than combining all decision trees in the random forest to yield a hard classification (of $k = 1$, 2, or 3), we used the outputs of the decision trees to generate a probability of class assignment. Let $h_i(\mathbf{u}(\mathbf{x}))$ be the class prediction made by the i-th decision tree given the feature vector $\mathbf{u}(\mathbf{x})$. Then the probability that the voxel

with feature $\mathbf{u}(\mathbf{x})$ belongs to class k can be computed as

$$p(k|\mathbf{u}(\mathbf{x})) = \frac{1}{500}\sum_{i=1}^{500}\delta[h_i(\mathbf{u}(\mathbf{x})) - k], \quad k \in \{1,2,3\}\,, \tag{2.4}$$

where $\delta[k]$ is the delta function. Figure 2.2 shows a training image and its 3-class labeling (derived from a manual labeling result) and a test image with the probability of its boundary class output from the trained random forest.

We then define the boundary term as

$$B(\mathbf{x},\mathbf{y}) = 1 - \max\left\{p(1|\mathbf{u}(\mathbf{x})), p(1|\mathbf{u}(\mathbf{y}))\right\}\,, \tag{2.5}$$

which yields a small value when either one of the two neighboring voxels has high boundary class probability and a large value when neither voxel is likely to be a boundary voxel. When this boundary term is used in Equation (2.1), the optimal cut is encouraged to be positioned along highly probable boundary voxels.

2.3.4 Energy Minimization

After the energy terms described in Sections 2.3.1, 2.3.2, and 2.3.3 are computed, the graph cut energy function in Equation (2.1) is minimized using the α-expansion algorithm [139]. We used the multi-label energy optimization library available online at `http://vision.csd.uwo.ca/code/`. We chose $\lambda_l = \lambda_c = 1.0$ in Equation (2.1) empirically according to experimental observations. The algorithm produces highly similar results when λ_l and λ_c are selected in the range $[0.5, 5]$.

2.4 Results

2.4.1 Data

T1-weighted magnetization prepared rapid gradient echo (MPRAGE) images of 92 subjects were acquired on a 3.0T MR scanner (Intera, Phillips Medical Systems,

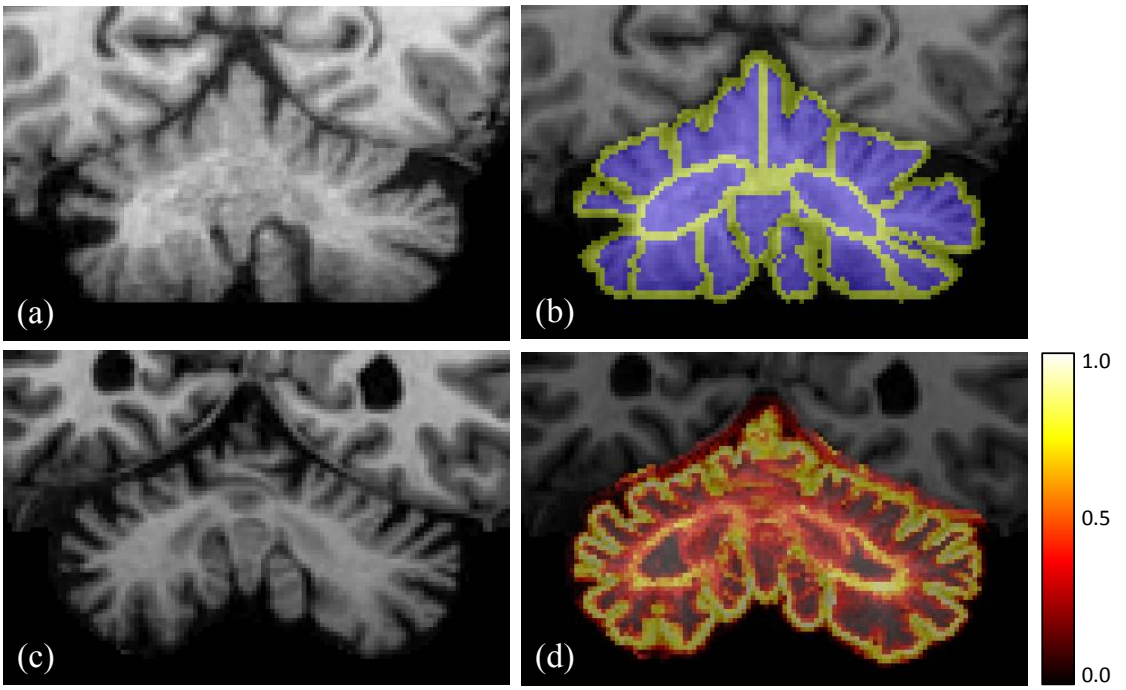

Figure 2.2: Example training and prediction result of the boundary classifier. (a) Preprocessed MR image of a subject used for training. (b) Voxel class overlaid with the image in (a), where yellow indicates boundary voxels, blue indicates lobule voxels and otherwise non-cerebellar voxels. (c) Preprocessed MR image of a test subject. (d) Boundary probability output from the random forest classifier overlaid with the image in (c).

Netherlands). The parameters of the MPRAGE are: 132 slices, axial orientation, 1.1mm slice thickness, 8° flip angle, TE = 3.9ms, TR = 8.43ms, FOV 21.2 × 21.2cm, matrix 256 × 256 (resolution: 0.828125 × 0.828125 ×1.1mm). 15 of the 92 subjects (containing both HC and patients) were manually delineated by an expert with over 5000 hours of training, using the protocol described in Bogovic et al. (2013) [120]. Table 2.1 summarizes the demographic information of each diagnosis group, in the expert delineated subject set and in the set with no expert delineation.

Table 2.1: Demographic information on both the set of 15 subjects with expert delineation and the set of 77 subjects without expert delineation. Key: N is the number of subjects; m/f is the male/female ratio; Age is the mean age; SD is the standard deviation of the age; healthy controls (HC); people who have symptoms of cerebellar dysfunction but no genetic diagnosis (CB); spinocerebellar ataxia type 2 (SCA2), type 3 (SCA3), and type 6 (SCA6).

	Expert delineated				**No expert delineation**			
	N	(m/f)	Age	(SD)	N	(m/f)	Age	(SD)
HC	6	(2/4)	54.3	(14.7)	44	(19/25)	56.5	(12.9)
CB	3	(1/2)	54.3	(8.0)	-	(-/-)	-	(-)
SCA2	-	(-/-)	-	(-)	4	(3/1)	48.8	(8.8)
SCA3	-	(-/-)	-	(-)	7	(2/5)	51.7	(9.3)
SCA6	6	(2/4)	55.3	(12.6)	22	(6/16)	58.8	(8.4)

2.4.2 Accuracy evaluation

In this experiment, 15 subjects with expert delineated labels were used to perform a leave-one-out validation study. Each subject was used as a test subject while the remaining 14 subjects were used in the multi-atlas labeling phase and also as training data for both the cerebellum tissue and boundary classifiers. In this way, results were computed for each of the 15 subjects and statistical performance measures were computed across these 15 subjects. See Table 2.1 for a summary of the diagnosis and demographic information on the 15 subjects. Three segmentation approaches were compared: ACCLAIM [136], NL-STAPLE (as described in Section 2.3.1), and the proposed method. To quantitatively evaluate the segmentation results, we first examined the overlap between the true and automatically obtained labels for each lobule using the Dice similarity coefficient (DSC). The DSC of a segmented region R against its manual delineation T is computed as

$$\mathrm{DSC} = \frac{2\,|R \cap T|}{|R| + |T|},$$

where $|\cdot|$ represents the volume of a region.

Figure 2.3 shows the statistics of the DSC between the manual and automatic labels. For the proposed method, most of the lobules have mean DSC above 0.70, and many are above 0.80 (CM, lobule I-IV, lobule VI, sub-structures of lobule VII, VIII vermis, and lobule IX). The worst mean DSC values are still above 0.60, and these occurred in lobules with relative small volumes such as lobules V and X. These structures also have a larger variation in DSC. Comparing the three segmentation algorithms, NL-STAPLE and the proposed method outperformed ACCLAIM in most of the lobules, with higher mean DSC for all the lobules and smaller DSC variance for almost all the lobules. The proposed method outperformed NL-STAPLE in most of the lobules, especially the lobules in the middle and caudal portions of the cerebellum (lobules XII, IX, and X). In order to evaluate the overall performance of segmentation on a subject, we computed the average volume weighted DSC (ADSC) over all lobules for each subject. The ADSC is computed as

$$\text{ADSC} = \frac{\sum_{i=1}^{N} |T_i| \, \text{DSC}_i}{\sum_{i=1}^{N} |T_i|}$$

where DSC_i is the DSC of the i-th lobule, and $|T_i|$ is the volume of the i-th lobule computed from the manual delineation. N is the total number of lobules.

Table 2.2 lists the ADSC of each subject in the leave-one-out experiment, grouped into three groups: 1) HCs, which have no cerebellar atrophy; 2) SCA6 patients, with atrophy varying from mild to severe; 3) CBs, which are patients with symptoms of cerebellar dysfunction but no genetic diagnosis or other diagnosis. In this particular 15 subject cohort, all the CBs happened to have severe cerebellar atrophy. The Wilcoxon two-sided signed rank test was carried out to compare the ADSCs of the 15 subjects produced by the proposed method and the other two, at a 5% confidence interval. The test results indicated that the proposed method improved the segmentation results over the other two methods significantly in terms of ADSC, with a p-value of 1.2×10^{-4} when compared with ACCLAIM and 3.3×10^{-3} when compared with NL-STAPLE. The mean and standard deviation (std) of ADSC for each group were also computed,

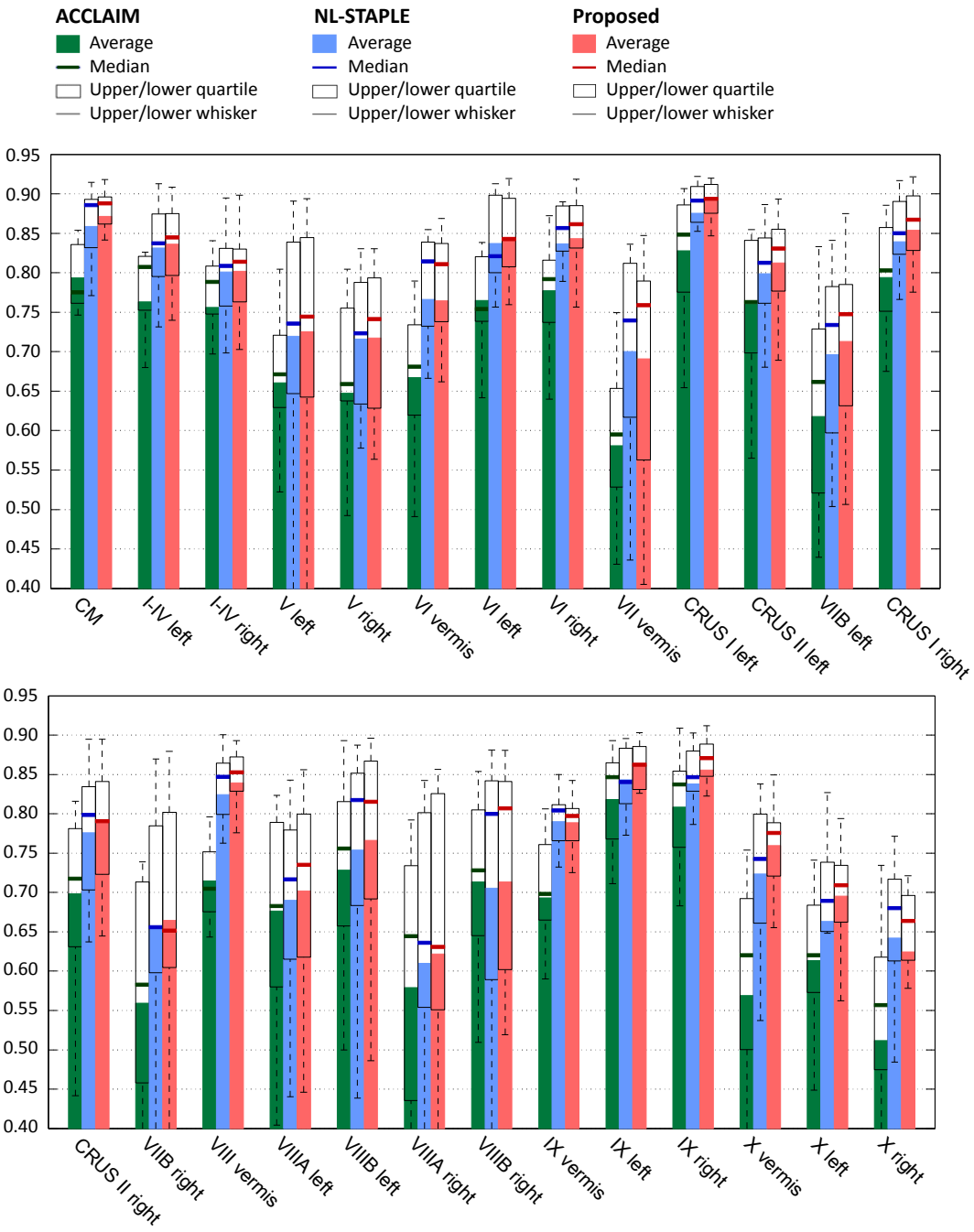

Figure 2.3: Box plots of Dice similarity coefficient comparing ACCLAIM, NL-STAPLE, and the proposed method.

as listed in Table 2.2. The proposed method has the highest mean ADSC among the three algorithms in each group. The ADSCs of the proposed method and NL-STAPLE are similar in the HC group. The ADSCs of the proposed method are higher than NL-STAPLE for all the subjects in both SCA6 and CB groups. The improvements are most prominent in the CB group where subjects have large cerebellar atrophy. Figure 2.4 shows example segmentation results generated by the three algorithms. We can see that NL-STAPLE and the proposed method outperformed ACCLAIM for both lobule location and boundary accuracy. The proposed method shows improvements over NL-STAPLE at the lobule boundaries, being able to capture the deep sulci and fissures.

Although the proposed method outperformed the other two methods in identifying cerebellar atrophy, the segmentation results were still biased towards the majority of the training data, which in our case comprises subjects with zero to moderate atrophy. The segmentation tended to over-estimate cerebellum tissue in subjects with large atrophy, resulting in a lower dice in the CB group.

Table 2.2: The average volume weighted dice similarity coefficient (ADSC) for each subject in the leave-one-out experiment, grouped by diagnosis. See Table 2.1 for a key of the diagnoses.

Method	**Healthy control**						
	1	2	3	4	5	6	mean ± std.
ACCLAIM	70.9	77.0	66.0	73.9	79.1	77.2	74.2 ± 4.9
NL-STAPLE	82.4	82.6	83.2	76.0	84.3	82.5	81.8 ± 2.9
Proposed	82.1	82.5	83.8	76.2	84.2	83.0	82.0 ± 2.9

Method	**SCA6**						
	1	2	3	4	5	6	mean ± std.
ACCLAIM	77.2	79.0	73.9	73.2	76.5	73.6	75.6 ± 2.3
NL-STAPLE	82.2	82.6	80.4	80.1	74.4	79.0	79.8 ± 3.0
Proposed	83.1	82.7	80.5	81.9	75.5	79.4	80.5 ± 2.8

Method	**CB**			
	1	2	3	mean ± std.
ACCLAIM	71.5	67.9	72.5	70.6 ± 2.4
NL-STAPLE	72.9	73.1	80.3	75.4 ± 4.2
Proposed	77.2	77.5	81.2	78.6 ± 2.2

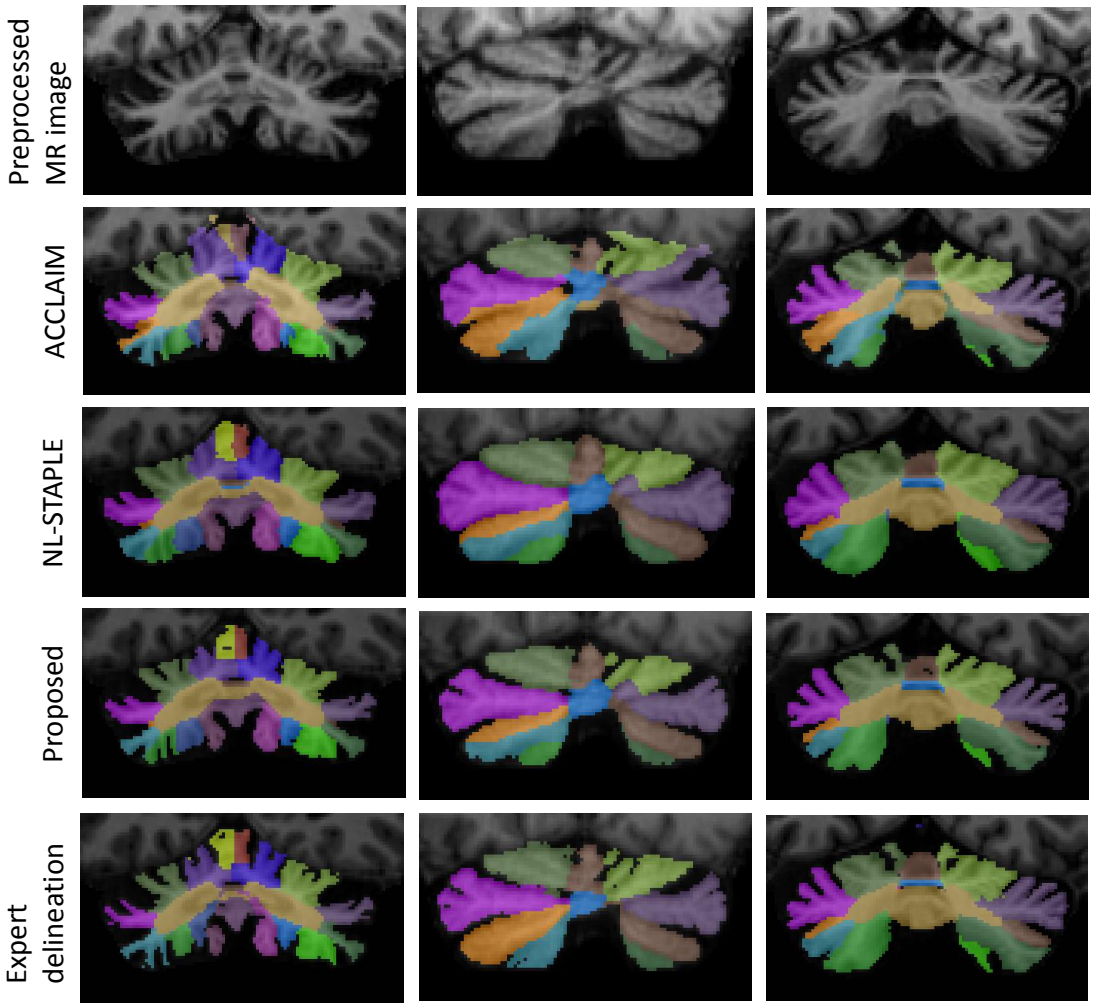

Figure 2.4: Example lobule segmentation results. Each column contains the preprocessed MR image (coronal slice), the segmentation results and the expert delineation of a subject. From the top to the bottom row are in turn the preprocessed MR images, the segmentation results obtained by ACCLAIM, NL-STAPLE, the proposed method, and the expert delineations.

2.4.3 Volumetric analysis in SCA

In this experiment, we applied the proposed segmentation method to 77 subjects (with no expert delineation) to study the region-specific cerebellar atrophy patterns in ataxia patients and to further validate the proposed method. The 15 expert labeled subjects were used for training. We studied three sub-types of SCA based on the volumetric measurements of the parcellated regions of interest (ROIs) from our method. The demographic information of the different groups is summarized in Table 2.1. In order to compare the degree of atrophy across different ROIs, we evaluated a relative ROI volume computed as follows. Let $v_{r,s}$ be the volume of ROI r in subject s. Let $\bar{v}_{r,\mathrm{HC}}$ be the average volume of ROI r over all healthy subjects. The relative ROI volume of ROI r for subject s is computed as

$$\tilde{v}_{r,s} = \frac{v_{r,s}}{\bar{v}_{r,\mathrm{HC}}}\,.$$

Figure 2.5 shows the statistics of the relative ROI volumes of gross anatomical divisions, while Figure 2.6 shows the statistics of relative ROI volumes of cerebellar lobules. A two-sided Wilcoxon rank sum test was carried out between the relative ROI volumes of each ataxia type and the HCs for each ROI, at a 5% confidence interval. The Wilcoxon rank sum test had a null hypothesis that the ROI volumes of the two groups have equal medians, against the alternative that they do not. The test results are marked at the bottom of the box-plots in Figures 2.5 and 2.6, where one star (p-value between 0.01 and 0.05) indicates the volume difference between the patient and healthy group is statistically significant, and two stars (p-value less than 0.01) indicates the difference has strong statistical significance.

As shown in Figures 2.5 and 2.6, SCA6 exhibits a global atrophy in comparison to the HCs, with significant atrophy across all lobules. The average relative ROI volumes against HCs were between 0.6 and 0.8 for CM, lobules in anterior and middle lobe, and between 0.7 and 0.9 for lobules in posterior lobes. SCA2 shows significant atrophy of the CM, middle lobe, and superior vermis with relative sparing of the posterior-inferior regions of the cerebellum. The above results are consistent with

the observations reported in [103, 104]. For SCA3, significant atrophy was found in the CM region and near significant atrophy was found in the anterior lobes. The fact that no significant volume decrease was found in other ROIs partially agrees with [97], which reported significant volume decrease in SCA3 against HCs in cerebellar vermis, and no significant volume change in cerebellar hemisphere.

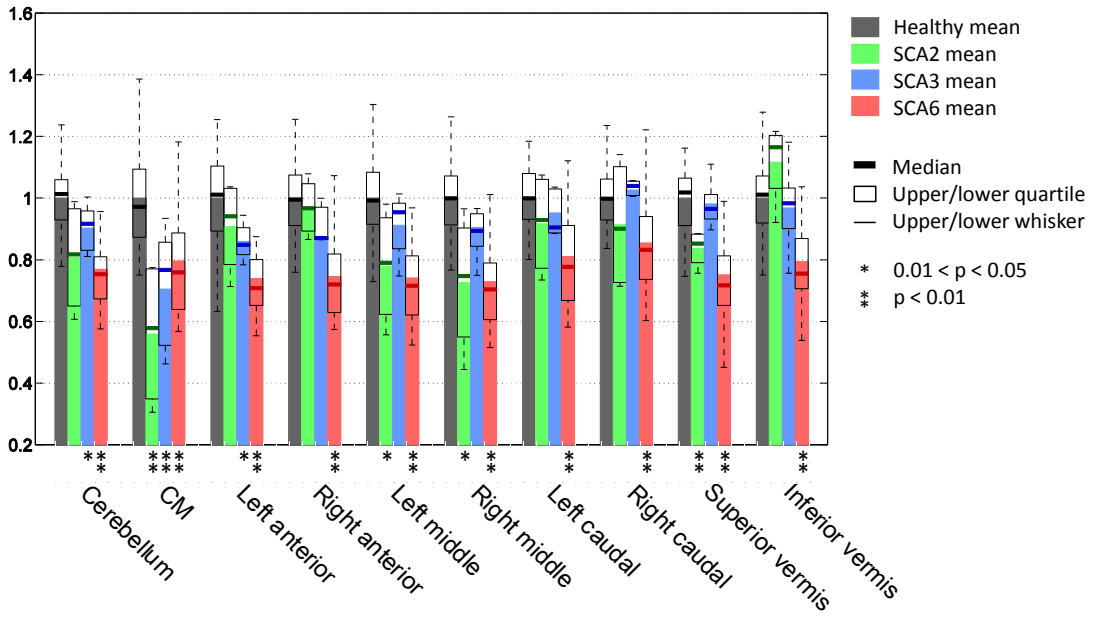

Figure 2.5: Box plots of relative lobe volumes for healthy controls and three SCA subtypes.

2.4.4 Discussion

The run time of the algorithm for one subject is ∼7 hours on a computer with 48GB Ram and 12 cores each with a 2.7Ghz Intel processor. It includes ∼6 hours of FreeSurfer processing, ∼40 mins for multi-atlas registration and label fusion, and ∼20 mins for computing the graph cut energy terms and optimization. One way to reduce the algorithm runtime is to replace the FreeSurfer processing part by other brain MR image analysis software that provides cerebellar tissue segmentation, e.g., TOADS [122], which take ∼3 hours to produce a whole brain segmentation. Since it can take 50–60 hours for an expert rater to label the cerebellar lobules, the proposed method has potential for MRI based volumetric studies involving large num-

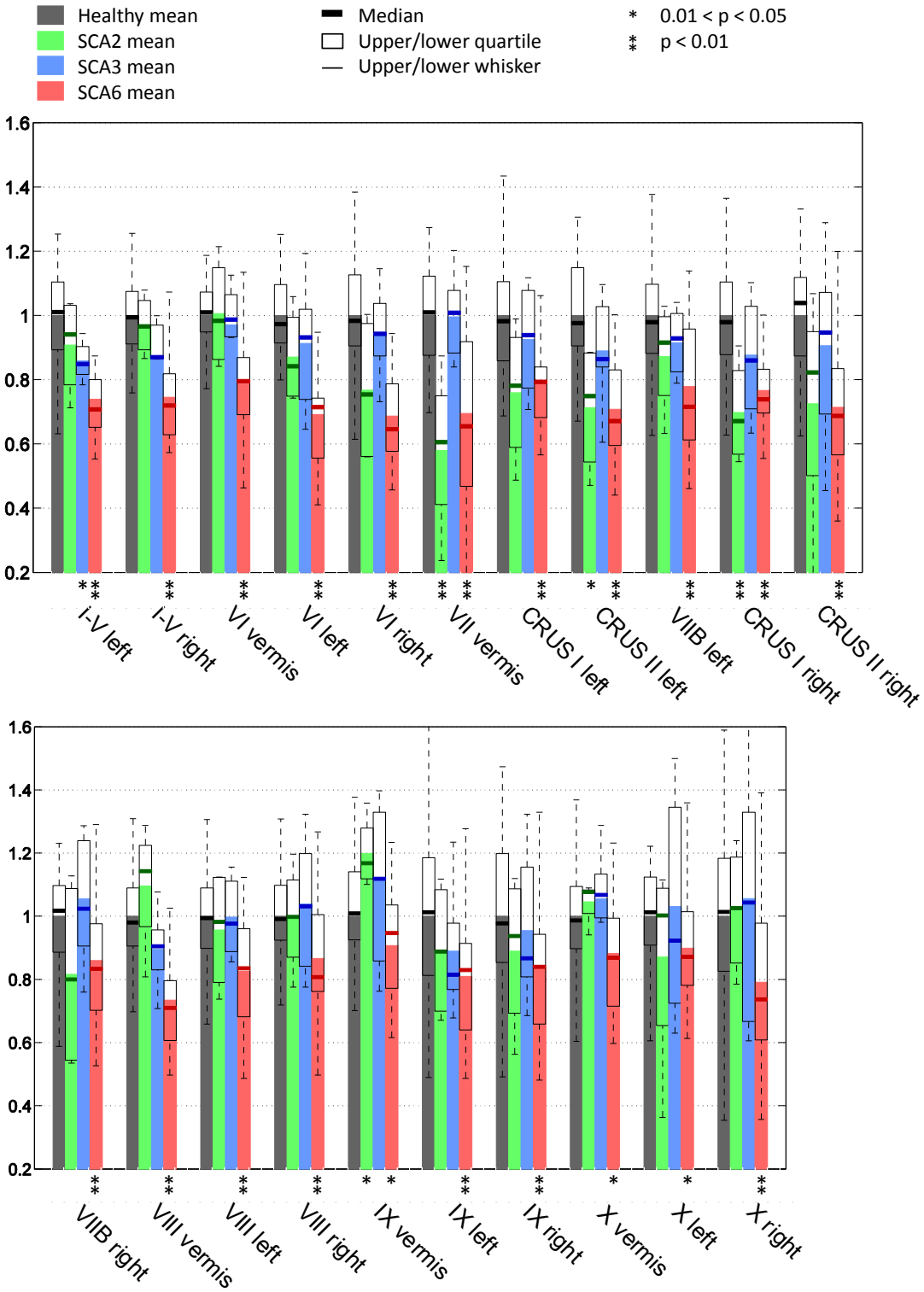

Figure 2.6: Box plots of relative lobule volumes for healthy controls and three SCA subtypes.

bers of subjects. Due to the data-driven nature of multi-atlas methods and learned tissue/boundary classifiers, the proposed method can be applied to any cerebellar parcellation protocol and any image modality, providing manually labeled training data with the same protocol and image modality.

2.5 Summary

In this chapter, we proposed a fully automated cerebellar lobule segmentation method that combines a multi-atlas result and tissue/boundary classification in a graph cut framework. The method was validated using a leave-one-out study on 15 expert delineated subjects including both healthy controls and patients with various degrees of cerebellar atrophy. The proposed method outperformed two state-of-the-art cerebellum segmentation methods, especially on subjects with moderate to large cerebellar atrophy. The proposed method was then applied to label the cerebellar lobules of a larger cohort consisting of healthy controls and patients with different SCA subtypes. Quantitative analysis of the ROI volumes showed significant regional volume decreases in all SCA sub-types and distinct patterns of atrophy for each subtypes. The observed atrophy patterns for different SCA sub-types are consistent with previous findings, in which cerebellar lobules were manually labeled by experts.

As mentioned at the beginning of the chapter, the purpose of the proposed segmentation method in this thesis is two-fold. In this chapter we have demonstrated the effectiveness of the proposed method for ROI volumetric analysis of the cerebellum on large population. In Chapter 3, we will use the lobule segmentation to construct a highly informative shape representation of the cerebellum.

Chapter 3

Cerebellar Shape Representation

In this chapter, we present two shape representations for cerebellar structures: a landmark shape representation of the collection of cerebellar lobules and a level set based whole cerebellum shape representation. The landmark representation is more informative as it contains shape information for each lobule, while the level set representation is simple to obtain (no cerebellar lobule parcellation and correspondence point finding needed) and thus free from errors due to this process. Both representations encode rich morphological information of the cerebellum and they lay the foundation for studying group difference, predicting disease/function, and identifying disease/function specific atrophy pattern.

In Section 3.1, we review the literature on shape analysis and the basics of the landmark and level set representations. In Sections 3.2 and 3.3 we use these shape representations to describe the shape of the cerebellum. In Section 3.4, we use the proposed cerebellar shape representations to study the cerebellar shape variation of different populations.

3.1 Statistical shape analysis

Shape analysis is an area of study arising from a wide variety of applications. For example, shape provides useful information for tasks like object recognition [150, 151] and segmentation [152,153]. The well accepted definition of *shape* by Kendall (1984) [154]

is that "shape is all the geometrical information that remains when location, scale, and rotational effects are removed". *Statistical shape analysis* is an analysis of the geometrical properties of some given set of shapes by statistical methods [96]. The statistical model learned from a population of shapes is called *statistical shape model* (SSM). The application of statistical shape analysis in biomedical image analysis lies in the following two aspects: 1) SSMs serve as shape priors in segmenting anatomical structures from images [153]; 2) SSMs can model group differences of anatomical structures and further used for predicting disease and functional decline [94, 155].

Statistical shape analysis have two main components: 1) Shape representation, which encodes the shape information into a set of homologous geometric primitives or basis functions across different subjects in a population; 2) Analysis method, which may involve modeling the distribution of shapes from a group of training subjects, defining a probability measure to identify abnormal shapes, or defining shape distance or metrics to quantify group differences. In the following section, we review different approaches in statistical shape analysis with a focus on these two components.

3.1.1 Literature review

An intuitive and widely used way to represent shape is to locate a finite number of landmarks on the object. A *landmark*, as defined in Kendall (1984) [154], is a point of correspondence on each object that matches between and within populations. Kendall (1984) [154], Kendall (1989) [156], Bookstein (1986) [157], Goodall (1991) [158], and Dryden and Mardia (1991) [159] established the theoretical foundation and methodology for analyzing shape using landmark representation. As for the analysis method, Goodall and Mardia (1993) [160], Dryden and Mardia (1991) [159], and Dryden and Mardia (1993) [161] used perturbation models. Cootes et al. (1992) [162,163] used principal components models. Although the principal component model is a special case of the perturbation model, it models the shape variation with more specificity, and thus has gained great popularity in various applications, e.g., object segmentation.

Medial models or skeletons are also commonly used to represent shapes [164].

They represent objects by their centerlines and corresponding radii, which result in a more compact description than landmarks. Pizer et al. (1999) [165,166] presented medial model named *M-Reps* consisting of a set of points on the centerlines and vectors pointing from the points toward the boundary. Styner built M-Reps on a spherical harmonic (SPHARM) approximated surface to incorporate object variability and to reduce the branching topology sensitivity of pure medial models [167–169]. Then statistical analysis can be carried out separately on the two medial shape properties—local position and thickness [89]—or directly on each point of the approximated surface [91]. Fletcher et al. [170] proposed principal geodesic analysis, a generalization of principal component analysis to the manifold setting, for analyzing the variation of a population of objects described by M-Reps.

A large number of other approaches to represent shapes by parameterizing the surfaces exist [153]: Fourier surfaces [171, 172], elastic models [173], extension of spherical harmonics [174, 175], wavelet transformation [176], spherical wavelets [177, 178], B-splines [179]. Most of them use principal component analysis (assume multivariate Gaussian distribution) to model the variation of a population.

The level set shape representation was introduced as a tool for numerical analysis of surfaces and shapes [180]. It is used widely for curve or surface evolution in image segmentation [181–183] and it has also proven to be useful for modeling shape statistics [184, 185]. It can represent arbitrary shapes and it inherently supports topology changes during deformation. Since it does not require establishing correspondence on an object surface (which often requires deformable registration), it is easy to compute and less prone to errors in computing the representation.

In the next two sections, we focus on two shape representations—the landmark representation and the level set representation. We describe in detail the standard steps for computing the two shape representations and building SSMs based on these representations.

3.1.2 Landmark based SSM

Landmark generation

A landmark shape representation describes a shape by locating a finite number of points on the outline. A landmark is a point of correspondence on each object that matches between and within populations (Dryden and Mardia (1998) [96]). Landmarks can be points that have anatomical meanings, or have a special geometrical property like high curvature, or are just points that are densely distributed on the object's boundary. Landmarks are also called homologous points, vertices, anchor points, fiducial markers, model points, markers, key points, etc. One way to assign landmarks across a set of training shapes is to manually designate corresponding points on each shape, which is time consuming and impracticable for 3D shapes. Automatic and semi-automatic methods for identifying corresponding points have been developed, mostly based on image or point set registration techniques [153]. Once the landmarks are assigned, a shape is represented by the ordered list of landmarks. A shape represented by M landmarks in D dimension is represented by an MD-dimensional column vector $\mathbf{x}$ formed by concatenating the spatial coordinates of the ordered landmarks (we assign $D = 3$ in the following context for simplicity)

$$\mathbf{x} = [x_1, y_1, z_1, x_2, y_2, z_2, \ldots, x_M, y_M, z_M]^T . \tag{3.1}$$

Shape alignment

According to the definition [154], shape is invariant under Euclidean similarity transformations. To obtain a true shape representation, location, scale, and rotational effects must be filtered out. This is carried out by establishing a *coordinate reference*—with respect to position, scale, and rotation, commonly known as *pose*—to which all shapes are aligned. This is solved by *Procrustes alignment* [80,158,163,186]. First we describe the alignment of two shapes. Let $\mathbf{x}_1$ and $\mathbf{x}_2$ be the shape representations of two shapes defined in Equation 3.1. Aligning $\mathbf{x}_1$ to $\mathbf{x}_2$ is realized by finding the Euclidean similar transformation T that minimizes the least-square error

between the spatial coordinates of the two shapes, i.e., $\|T(\mathbf{x}_1) - \mathbf{x}_2\|_2^2$, where $\|\cdot\|_2$ is the l_2 norm. The transformation T can be solved analytically [80, 96, 187]. To align a set of shapes, an iterative approach with the following procedures is carried out:

1. Choose an initial estimate of the mean shape (often the first shape in the set).
2. Align all the remaining shapes to the mean shape.
3. Recalculate the estimate of the mean from the aligned shapes.
4. If the estimated mean has changed, return to step 2.

Convergence is thus declared when the mean shape does not change significantly within an iteration. Bookstein [80] notes that two iterations of the above should be sufficient in most cases. To obtain an estimate of the mean shape, the most frequently used is the *Procrustes mean shape* or just the *Procrustes mean*,

$$\bar{\mathbf{x}} = \frac{1}{N} \sum_{i=1}^{N} \mathbf{x}_i, \tag{3.2}$$

where N is the number of shapes.

Statistical Analysis

Consider a set of N aligned shapes with M landmarks. Each shape instance can be represented by a $3M$-dimensional vector, or a point in a $3M$-dimensional space. The set of N shapes gives a cloud of N points in the $3M$-dimensional space. Principal Component Analysis (PCA) is an efficient way to model the distribution in high-dimensional space, assuming multivariate Gaussian distribution. Let $\mathbf{x}_i$ be the vector representation of the ith shape instance. Then the mean shape $\bar{\mathbf{x}}$ is computed as

$$\bar{\mathbf{x}} = \frac{1}{N} \sum_{i=1}^{N} x_i. \tag{3.3}$$

The principal axes of the point cloud are described by $\{\mathbf{e}_k\}, k = 1, \ldots, 3M$, the unit eigenvectors of the sample covariance matrix $\mathbf{S}$, ordered by the corresponding

eigenvalues $\{\lambda_k | \lambda_1 \geq \lambda_2 \geq \cdots \geq \lambda_{3M}\}$. The eigenvectors are called principal shape modes. A shape $\mathbf{x}$ in the training set can be approximated by the mean shape and a linear combination of the first t shape modes:

$$\mathbf{x} = \bar{\mathbf{x}} + \mathbf{E}\mathbf{b}, \tag{3.4}$$

where $\mathbf{P} = [\mathbf{e}_1, \mathbf{e}_1, \ldots, \mathbf{e}_t]$ and $\mathbf{b}$ is a column vector of weights. Equation 3.4 allows us to generate new examples of shapes by specifying the coeffcients $\mathbf{b}$ within suitable ranges, so that the synthetic shape will be similar to the training shapes. The suitable limits are typically

$$-3\sqrt{\lambda_k} \leq b_k \leq 3\sqrt{\lambda_k}. \tag{3.5}$$

Equations 3.4 and 3.5 together provide an *allowable shape domain* [163]. It can be used as constraints in segmentation tasks. It can also generate new shapes in a systematic way, which is appealing for visualization purposes.

3.1.3 Level set based SSM

Level set function

A level set function φ can be used to represent the shape or region $\Omega \subset \mathbb{R}^3$ as follows

$$\varphi(\mathbf{x}) \begin{cases} > 0, & \mathbf{x} \in \Omega \setminus \partial\Omega \\ = 0, & \mathbf{x} \in \partial\Omega \\ < 0, & \mathbf{x} \in \mathbb{R}^3 \setminus \Omega \end{cases}. \tag{3.6}$$

Often a special form of level set function, the signed distance function (SDF), which satisfies $|\nabla\varphi| = 1$, is used. Given a closed and bounded shape $\Omega \in \mathbb{R}^3$, there is a unique solution to the above constraints

$$\varphi(\mathbf{x}) = \begin{cases} -d(\mathbf{x}), & \mathbf{x} \in \Omega \setminus \partial\Omega \\ 0, & \mathbf{x} \in \partial\Omega \\ d(\mathbf{x}), & \mathbf{x} \in \mathbb{R}^3 \setminus \Omega \end{cases}, \tag{3.7}$$

where

$$d(\mathbf{x}) = \min_{\mathbf{x}_b \in \partial\Omega} (|\mathbf{x} - \mathbf{x}_b|) \tag{3.8}$$

is the distance from a point $\mathbf{x}$ to the boundary $\partial\Omega$. Any shape yields a unique SDF, and vice versa. SDF on a discrete grid can be efficiently computed with the fast marching method [180]. In order to reduce the impact of large distance values far from the object boundary, the SDF can be truncated by a threshold value $d_{\max}$

$$\varphi(\mathbf{x}) = \begin{cases} \max(-d(\mathbf{x}), -d_{\max}), & \mathbf{x} \in \Omega \setminus \partial\Omega \\ 0, & \mathbf{x} \in \partial\Omega \\ \min(d(\mathbf{x}), d_{\max}), & \mathbf{x} \in \mathbb{R}^3 \setminus \Omega \end{cases}, \tag{3.9}$$

resulting in a truncated SDF (TSDF). Suppose the TSDF is computed on an $L \times L \times L$ grid; then the shape can be represented by a vector $\mathbf{v} \in R^{L^3}$.

Shape alignment

Similar to landmark based SSM, Procrustes alignment can be applied to align a set of shapes. Instead of aligning the landmark points, the alignment of two shapes Ω_1 and Ω_2 is often realized by aligning their corresponding level set functions φ_1 and φ_2. First, a Euclidean similar transformation T is obtained by minimizing $\|\varphi_1(T(\mathbf{x})) - \varphi_2(\mathbf{x})\|_2^2$, where $\|\cdot\|_2$ is the l_2 norm. T is then applied to Ω_1, resulting in the aligned shape $T(\Omega_1) = \{\mathbf{x} \in \mathbb{R}^3 | T(\mathbf{x}) \in \Omega_1\}$. The set of all shapes are aligned by Procrustes alignment, as described in Section 3.1.2. After alignment, the level set functions are recomputed for each aligned shape.

Statistical Analysis

Consider a set of N 3D shapes, with each shape, after alignment, represented by a level set function on a $L \times L \times L$ grid, or a L^3-dimensional vector $\mathbf{v}$. As in landmark based SSM, PCA is used to model the shape variation.

3.2 Cerebellar lobule landmark representation

In this section, we present a landmark based shape representation for cerebellar structures. We treat the cerebellum with its lobule parcellation as a multi-object shape, and we describe the cerebellum by the collection of dense landmarks on the boundaries of all lobules. A challenge of using the landmark representation to model anatomical structures, especially 3D structures, is establishing dense corresponding landmarks across different subjects. Multi-object shapes (as in the collection of lobules comprising a cerebellum) add another level of complexity [188]. We address the correspondence building problem for multiple structures by applying a two-step non-rigid point set registration between the template point set and the subject point set, with the first step registering all lobules as a whole and the second step registering each lobule separately. The deformed template point set is then used as the landmarks of the subject. The steps for generating landmark representation is described in detail next.

The cerebellum was segmented from the MR image and parcellated into K cerebellar lobules, using the method described in Chapter 2. A dense triangulation of the boundary surface of each lobule was generated by the marching cubes algorithm [189]. Figure 3.1 shows the input MR image, the lobule segmentation, and the generated triangular meshes of lobules.

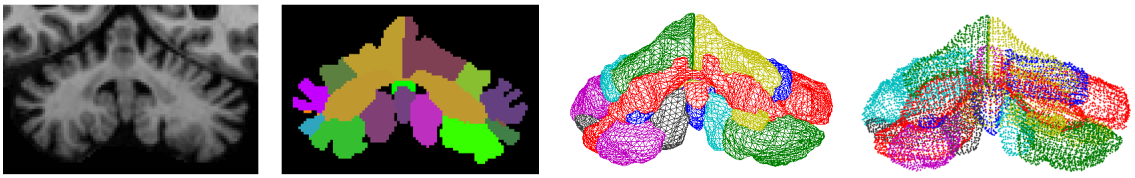

Figure 3.1: From MR image to lobule meshes: a) MR image of the cerebellum; b) Lobule segmentation; c) Triangular meshes of all lobules; d) Vertices of the lobule meshes.

Let $\{m_1, m_2, \ldots, m_K\}$ be the set of lobule meshes generated from a subject, where

K is the number of lobules. Let $p_{k,i}$ be the ith vertex of m_k. The set of points from m_k is represented by $P_k = \{p_{k,1}, p_{k,2}, \ldots, p_{k,M_k}\}$, where M_k is the number of vertices from m_k. The set of points from all lobules is then $P = \bigcup_{k=1}^{K} P_k$, which can be called the point set of a subject or subject point set. An arbitrary subject is selected as the template, and the template point set is denoted by P^0. The landmark representation of a subject is obtained through two steps of non-rigid registration:

1. The template point set P^0 is registered to the subject point set P through a non-rigid transformation, resulting in P^1. Coherent point drift (CPD) [190] is used to implement the non-rigid point set registration.

2. For each lobule k, P_k^1 (the set of points in P^1 that belongs to lobule k) is registered to P_k^r (the set of points in P^r that belongs to lobule k) through a non-rigid transformation, resulting in P_k^2. $P^2 = \bigcup_{k=1}^{K} P_k^2$ then denotes the template point set after two steps of non-rigid registration.

P^2 is assigned as the landmarks of the subject, since it has the shape of the subject point set P, and the corresponded point order to the template point set P^0. Figure 3.2 shows the initial template point set P^0, and the template point set after each step of non-rigid registration, i.e., P^1 and P^2, overlaid with subject point set P.

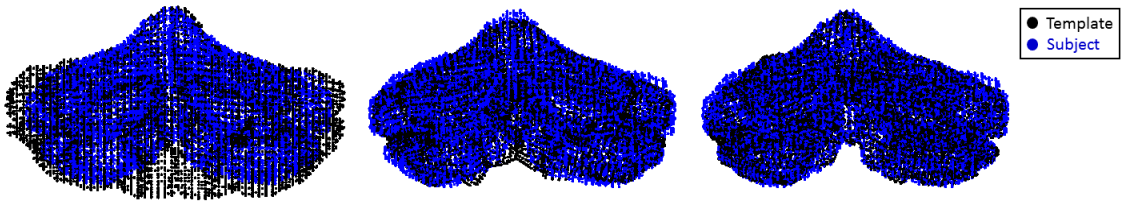

Figure 3.2: Two-step non-rigid point set registration: a) Template point set and subject point set before non-rigid registration; b) after whole cerebellum non-rigid registration; c) after individual lobule non-rigid registration.

Let $\{x_i, y_i, z_i\}$ be the spatial coordinates of the ith landmark; the landmark shape

representation of the subject is the vector

$$\mathbf{s} = [x_1, y_1, z_1, x_2, y_2, z_2, \ldots, x_M, y_M, z_M]^T, \tag{3.10}$$

where $M = \sum_{k=1}^{K} M_K$ is the number of landmarks from all lobules. In our case $M \approx 15,000$.

In this work, we modify the shape definition by including scale effects in the shape. In our definition, a shape is all the geometrical information that remains when translation and rotation are filtered out from an object. We include scale in shape because, cerebellar atrophy in ataxia patients will result in a global scale change of the cerebellum, especially those with severe cerebellar atrophy. This global scale change is not captured if scale is filtered out. In the Procrustes alignment, the transformation applied to align the landmarks is rigid transformation (only allow translation and rotation).

3.3 Whole cerebellum level set representation

In this section, we present an alternative cerebellar shape representation based on the level set function of the whole cerebellum shape. The advantage of this representation over the representation presented in Section 3.2 is that it is much easier to compute and less prone to segmentation and registration errors. The whole cerebellum can be obtained by many available brain image analysis software packages such as FreeSurfer [121], TOADS [122], BrainSuite [191], and Caret [192,193]. In this work, we use FreeSurfer version 5.3.0 [121] for the whole cerebellum segmentation. The steps for generating the level set representation is described in detail next.

As part of FreeSurfer processing, each MR scan is transformed into MNI space, and a whole brain parcellation is performed, including a segmentation of the whole cerebellum and its gray matter (GM) and white matter (WM). Let $\Omega_{GM} \subset \mathbb{R}^3$ and $\Omega_{WM} \subset \mathbb{R}^3$ denote the cerebellar GM and WM region, respectively. TSDF is computed from the whole cerebellar region $\Omega_C = \Omega_{GM} \cup \Omega_{WM}$. Figure 3.3 shows an

example of this process from MR images to TSDF level set representation. As in Section 3.2, Procrustes alignment is carried out with a rigid transformation (no scale adjustment) as the alignment transformation.

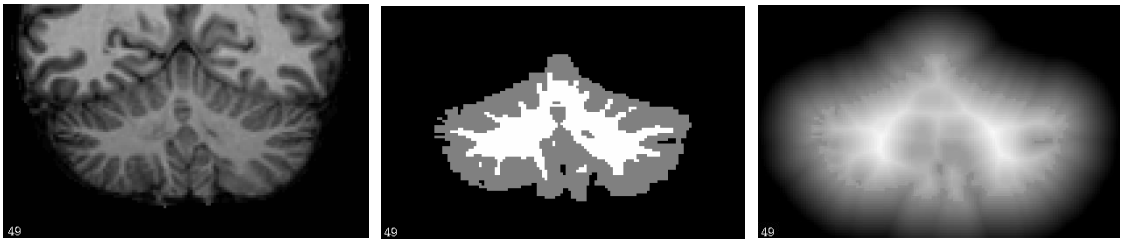

Figure 3.3: From MR image to level set shape representation. (a) MR image (coronal slice); (b) Cerebellar GM and WM region obtained from FreeSurfer processing; (c) Truncated signed distance function (TSDF) of the whole cerebellum.

3.4 Results

In this section, we demonstrate the effectiveness of the two cerebellar shape representations presented in Sections 3.2 and 3.3 by building SSMs using the two representations and studying the cerebellar shape variations for different groups of subjects. See Sections 3.1.2 and 3.1.3 for the details of building SSMs using the two types of shape representations. The set of subjects to be studied include 65 healthy controls and 58 patients with five types of cerebellar ataxia. Demographic information is summarized in Table 3.1.

Table 3.1: Demographic information of the 123 subjects being studied. Key: N number of subjects; m/f is the male/female ratio; Age is the mean age; SD is the standard deviation of the age; healthy controls (HC); spinocerebellar ataxia type 2 (SCA2), type 3 (SCA3), type 6 (SCA6) and type 8 (SCA8); ataxia-telangiectasia (AT).

	N	(m/f)	Age	(SD)
HC	65	(28/37)	50.7	(17.7)
SCA2	4	(3/1)	48.8	(8.8)
SCA3	7	(2/5)	51.7	(9.3)
SCA6	27	(7/20)	58.4	(9.3)
SCA8	2	(2/0)	43.5	(16.3)
AT	18	(12/6)	18.3	(6.2)

Figures 3.4 and 3.5 show the cerebellum of five representative healthy controls, rendered from the two shape representations. Figures 3.6 and 3.7 show the cerebellum of five representative SCA6 subjects, rendered from the two shape representations.

SSMs were built using the two shape representations and principal modes of variation are visualized for different groups of subjects. Figures 3.8–3.11 show the first and second principal modes of variation for the whole dataset (including healthy controls and patients of all ataxia types) computed using the two shape representations, respectively. Figures 3.12 and 3.13 show the first principal modes of variation for healthy control group computed using the two shape representations respectively. Figures 3.14 and 3.15 show the first principal modes of variation for SCA6 group using the two shape representations, respectively.

As shown in Figures 3.4–3.7, the cerebellar lobule shapes are much more smooth and regular than the whole cerebellum shapes. This is because the graph cuts based lobule segmentation locates a smoothed lobule boundary with high precision, while FreeSurfer cerebellar tissue segmentation tends to under-estimate the cerebellum region, resulting in branch like shapes. See Section 2.3 for more details.

For the whole dataset SSM, the first mode of variation computed using the two representations are similar, capturing overall size change of the cerebellum and volume change of individual lobules in the posterior lobes (Figures 3.8 and 3.9). Level set representation shows a significant change in the medial part of the anterior lobe (see the top of the cerebellum in Figure 3.9), which is not observed in landmark representation. The cerebellar lobule landmark representation reveals relative changes of different lobules. As shown in Figure 3.8, the lobules in the posterior lobes, especially CRUS I and II, undergo much larger shape changes than lobules I–V and corpus medullare. For the second mode of variation, landmark representation captures a combined change of lobule volumes and the aspect ratio (width versus height) of the whole cerebellum (Figures 3.10 and 3.11). The level set representation captures a more apparent aspect ratio change of the whole cerebellum (see Figure 3.11).

For the SSM of the healthy control group, the first mode of variation computed using the two representations are similar, capturing the elongation in the transverse

direction and a mild overall size change (Figures 3.12 and 3.13). An interesting observation from the landmark representation is that with the decreasing of cerebellum width, the medial part of the two hemispheres become closer (see bottom row in Figure 3.12).

For the SSM of SCA6 patient group, the mean shapes have smaller size than the mean shapes of the healthy, and also wider fissures in the posterior lobes (see middle columns in Figures 3.14 and 3.15). The first mode of variation computed using the two representations are similar, also capturing an overall size change of the cerebellum and volume change of individual lobules in the posterior lobes (Figures 3.14 and 3.15). This variation reflects the different degrees of cerebellar atrophy within the SCA6 group. SCA6 patients with a short disease duration can have very mild atrophy and their cerebella look very much like that of healthy subjects (see SCA subject 1 in Figure 3.6). Again the cerebellar lobule landmark representation reveals relative changes of different lobules. As shown in Figure 3.14, the lobules in the posterior lobes, especially CRUS I and II, undergo much larger shape changes than lobules I–V and corpus medullare.

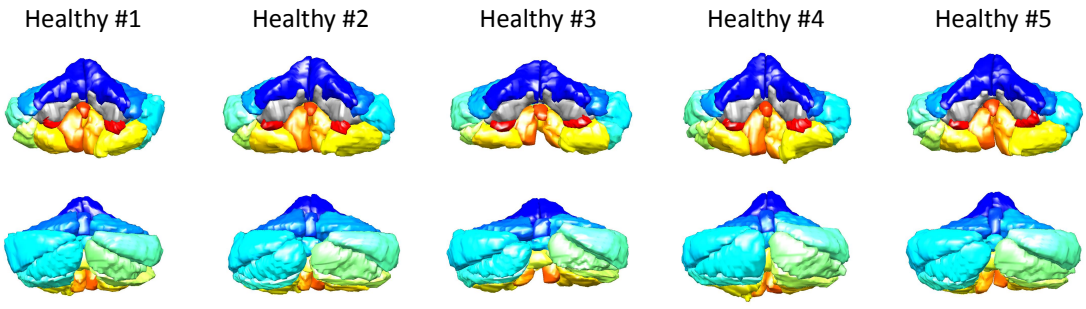

Figure 3.4: Cerebellar lobule shapes of five representative healthy controls. The top row is the anterior view and the bottom row the posterior view.

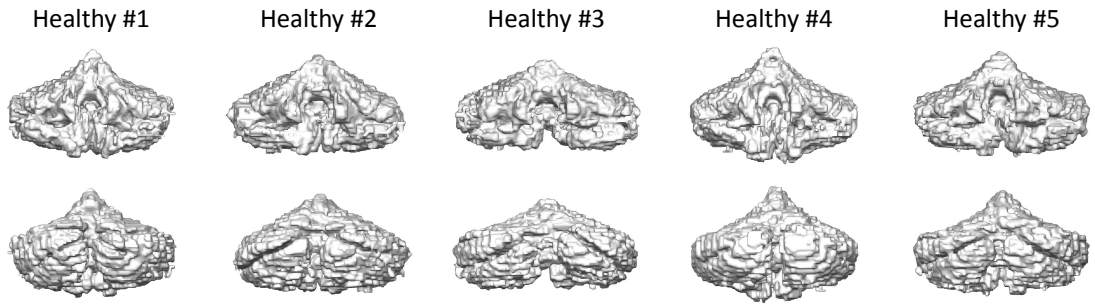

Figure 3.5: Whole cerebellum shapes of five representative healthy controls (the same five subjects as in Figure 3.4). The top row is the anterior view and the bottom row is the posterior view.

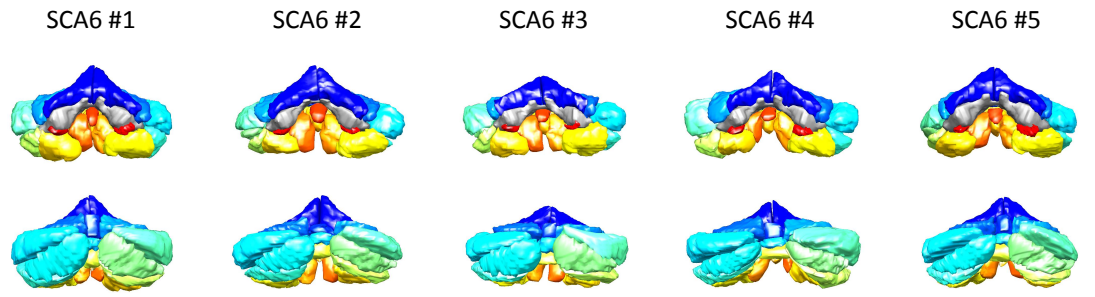

Figure 3.6: Cerebellar lobule shapes of five representative SCA6 subjects. The top row is the anterior view and the bottom row is the posterior view.

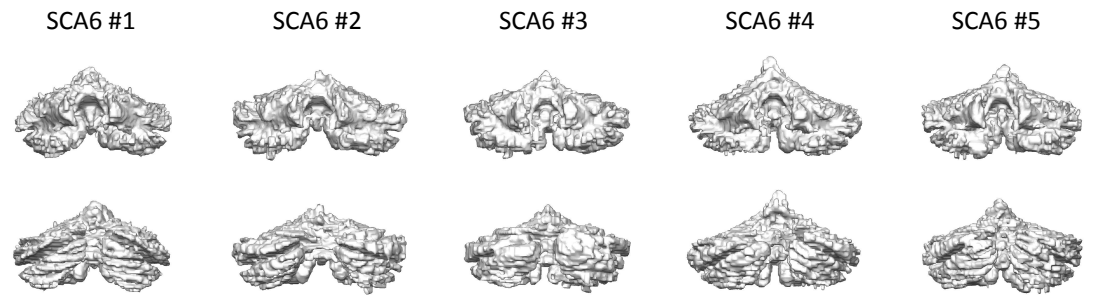

Figure 3.7: Whole cerebellum shapes of five representative SCA6 subjects (the same five subjects as in Figure 3.6). The top row is the anterior view and the bottom row the posterior view.

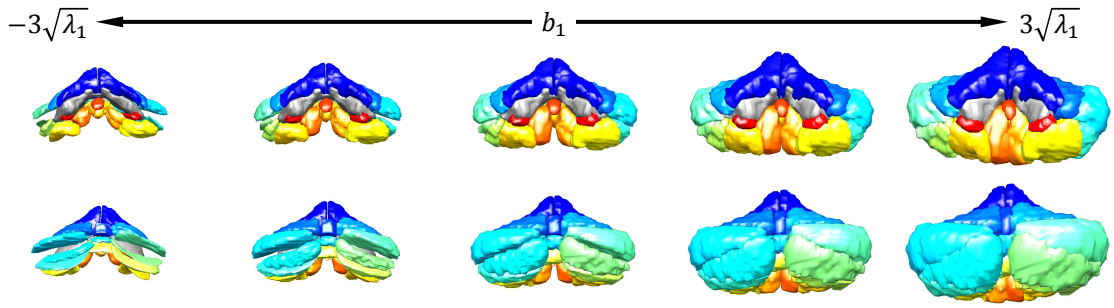

Figure 3.8: The first mode of variation of the whole population. The top row is the anterior view and the bottom row is the posterior view.

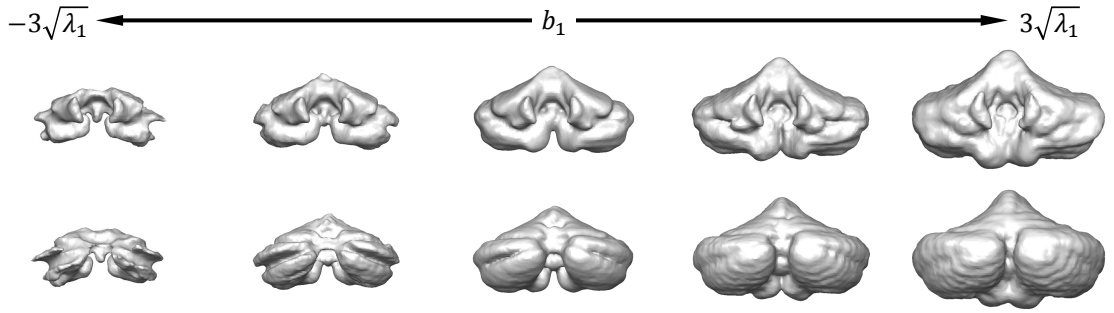

Figure 3.9: The first mode of variation of the whole population. The top row is the anterior view and the bottom row is the posterior view.

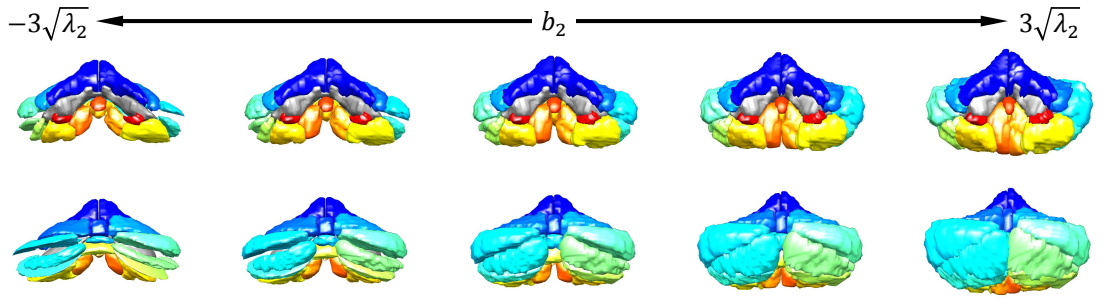

Figure 3.10: The second mode of variation of the whole population. The top row is the anterior view and the bottom row is the posterior view.

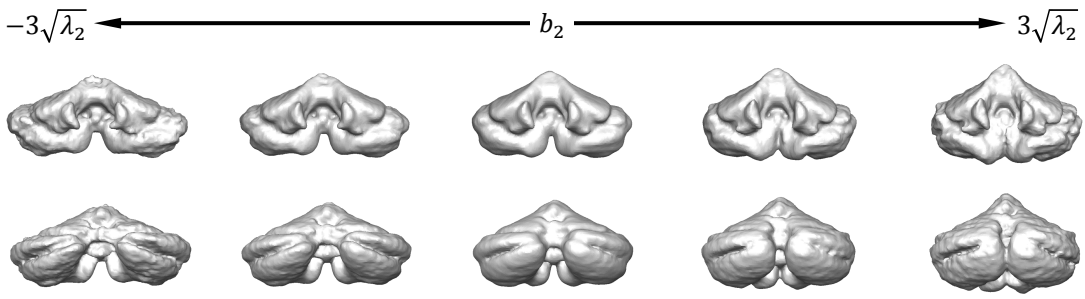

Figure 3.11: The second mode of variation of the whole population. The top row is the anterior view and the bottom row is the posterior view.

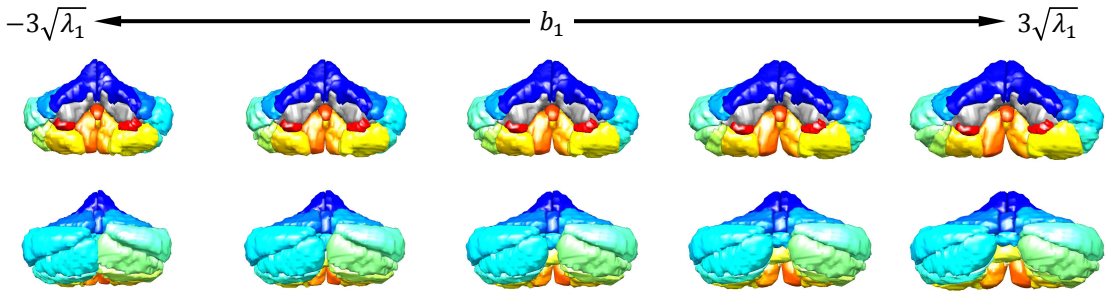

Figure 3.12: The first mode of variation of the healthy control group. The top row is the anterior view and the bottom row is the posterior view.

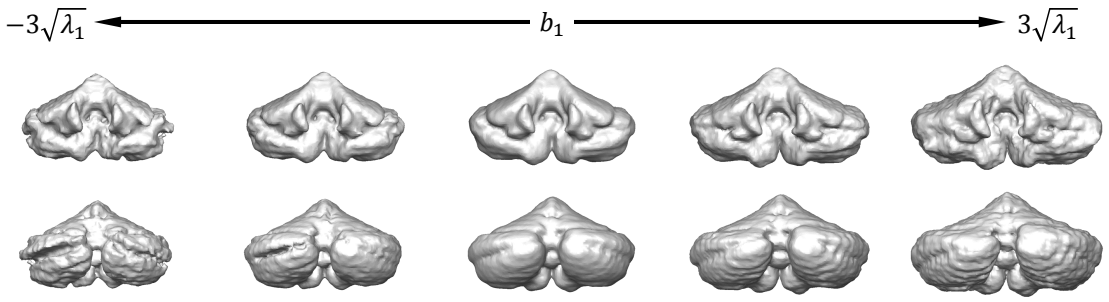

Figure 3.13: Cerebellar shape variation along the first principal direction of healthy control group. The top row is the anterior view and the bottom row is the posterior view.

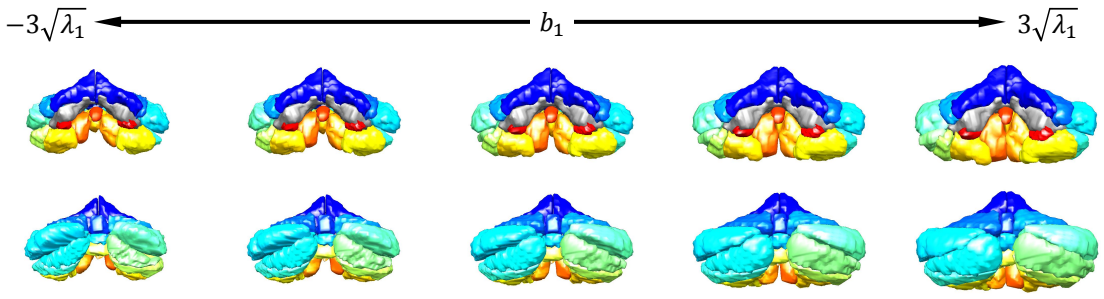

Figure 3.14: The first mode of variation of SCA6 group. The top row is the anterior view and the bottom row is the posterior view.

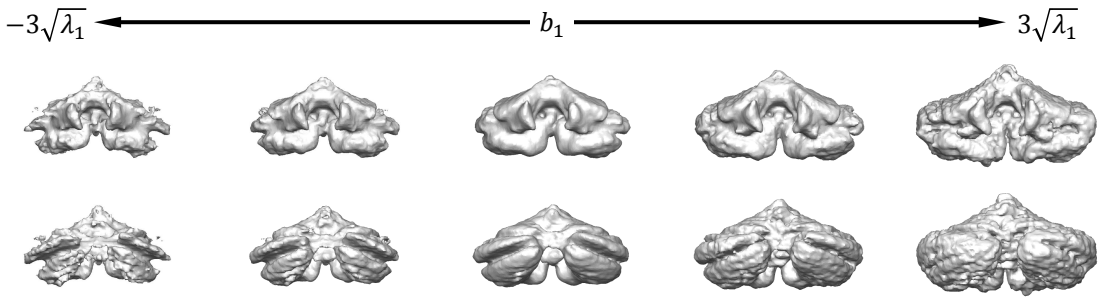

Figure 3.15: The first mode of variation of SCA6 group. The top row is the anterior view and the bottom row is the posterior view.

3.5 Summary

In this chapter, we presented two highly informative cerebellar shape representations: a landmark shape representation of the collection of cerebellar lobules and a level set based whole cerebellum shape representation. Based on the two shape representations, we studied the cerebellar shape variation of different populations. The two shape representations yield similar and realistic shape variations for each group, demonstrating the effectiveness of the shape representations. In Chapters 4 and 5, we use the proposed cerebellar shape representations for disease classification, functional score regression, and identifying disease or function specific atrophy patterns.

Chapter 4

Disease classification and atrophy pattern visualization

As mentioned in Section 1.1, it is of great interest to study the cerebellar atrophy pattern associated with specific disease types and to correlate the structural change with specific functional degeneration. In this chapter, we develop a classifier to classify healthy and different disease types and to identify characteristic cerebellar atrophy patterns associated with different cerebellar ataxia types based on the cerebellar shape representations presented in Chapter 3.

The remainder of this chapter is organized as follows. In Section 4.1, we review background on classification methods and dimension reduction techniques. In Section 4.2, we design a diagnosis classifier to classify healthy controls and different ataxia types. In Section 4.3, we present a method to visualize characteristic cerebellar atrophy pattern associated with different cerebellar ataxia types. In Section 4.4, we first test the diagnosis classifier using leave-one-out cross-validation with an extensive comparison of different combinations of cerebellar structural representations, classifiers, and dimension reduction techniques; then we study the characteristic cerebellar atrophy pattern of four ataxia types and to previous findings in the literature.

4.1 High-dimensional classification

Classification has many applications in various fields like computer vision, speech recognition, disease classification, drug development, etc. Various classification methods have been developed and widely used in the last several decades. Supervised classification learns from training data consisting of observations with known class a decision rule that can predict the class of a new observation. An observation can be a collection of variables represented as a *feature vector*. When the dimension of the input feature vector is high, as in our case, it poses difficulties to classification methods. Difficulties include unreliable parameter estimation for classification models and poor generalization ability. In this section, we first present some background on popular classification methods and the classifiers that we will use later in this chapter. We then discuss the impact of high-dimensional input on classification, and finally we discuss dimension reduction techniques to which can be used address the problem.

4.1.1 Classification

Linear classifiers

Linear classifiers, which base their classification on the linear combination of the input variables, are among the earliest classification methods developed. A linear classifier a classification decision based on the linear combination of the input variables. Popular linear classifiers include linear discriminant analysis (or Fisher's linear discriminant) [71], logistic regression [194, 195], naive Bayes classifier [196], and perceptrons [197]. Linear classifiers work well for many problems, reaching accuracy levels comparable to non-linear classifiers while taking less time to train and use [198]. However, when the boundaries between classes are nonlinear, linear classifiers might not work very well.

We use linear discriminant analysis (LDA) [71] as one of our classifiers to to classify diseases and to identify disease specific atrophy patterns. LDA models conditional density functions for different classes as Gaussian distributions with common covariances and assigns the class of a new observation to the one maximizes the posterior

probability.

Support vector machine (SVM)

SVM was first introduced in Boser et al. (1992) [199] and became popular because of its success in handwritten digit recognition [200, 201]. Consider a two-class classification problem. SVM constructs a hyperplane in a high-dimensional space that optimally separates the samples from two classes. When the two-class are *linearly separable*, i.e., there exists at least one hyperplane with all of the samples from class 1 on one side of the hyperplane and all the samples from class 2 on the other side, an optimal separation is defined as the hyperplane that produces the largest distance to the nearest training samples of any class, called a *margin*, since in general the larger margin means lower generalization error. The nearest training samples to the hyperplane are called *support vectors*.

Soft Margin and *kernel tricks* were introduced in SVM to deal with data that are not linearly separable. *Soft Margin* introduces non-negative "slack variables" that measures the degree of misclassification, and the resulting hyperplane optimizes a trade off between a large margin and a small error penalty of the misclassification [74]. The *kernel trick* [202] implicitly maps the input space to a higher dimensional space where the data is linearly separable, thus creating nonlinear classification [199]. SVM is very flexible since different kernel functions can be specified for the decision function. SVM is also effective with high-dimensional input. But if the input dimension is much greater than the number of samples, the method is still likely to give poor performance.

Decision trees

A decision tree classifies an observation by submitting it to a series of tests that determine the class. The tests are organized in a tree structure. The training samples are used for choosing the tests in the decision tree. A decision tree is often constructed from top to bottom, choosing the tests that best splits the set of samples first. The best split is often measured by information gain. Pruning procedures are often neces-

sary to avoid over-fitting problem of decision trees. The advantages of decision trees are that they are simple to understand and interpret, relatively easy to construct, and perform well on large datasets. One big disadvantage of decision trees is that they can be sensitive to small variations in the data, which can be mitigated by using decision trees within an ensemble.

Random forests, which we use as one of our classifiers, is an ensemble of decision trees [149]. It builds a set of decision trees at training time and outputs the class that is the mode of the classes output from the individual trees. Random forests combines the "bagging" idea, wherein each decision tree is constructed by using a random subset of the training data, with a random selection of features to build the test at each tree node. Random forests largely correct the over-fitting problem of single decision trees. It is one of the most accurate classification methods and it is quite robust to redundant variables. It can run efficiently on large datasets and it can provide a measure of the importance of each feature in forming the classifier, which can be useful in feature selection.

4.1.2 The curse of dimensionality

It can be proved that any set of two-class samples in general position with the number of samples equal or less than the dimensionality of its feature space is linearly separable [203]. The classifier learns the appearance of instances and exceptions that are specific to the training data and do not generalize well to the new data. This phenomenon is called over-fitting and is a direct result of the curse of dimensionality.

Various approaches have been proposed and successfully applied to avoid the over-fitting that comes with high-dimensional input. On the data side, dimension reduction and feature selection methods have been applied. On the algorithm side, model regularization (SVM), and bootstrap aggregating, or bagging (random forest) have been applied. And the two types of approaches are often combined in analyzing high-dimensional input data. Popular classification methods, like SVM and random forests, incorporate regularization or bagging to best avoid over-fitting, but dimension reduction is still necessary when dealing with high-dimensional input. Choosing

appropriate dimension reduction methods can improve the classification result.

4.1.3 Dimension reduction

Dimension reduction transforms the data in the high-dimensional space to a space with fewer dimensions. Dimension reduction methods can be categorized into unsupervised (not using class labels) and supervised (using class labels). One of the most widely used unsupervised dimension reduction methods is principal component analysis (PCA) [64, 204, 205]. It performs a linear mapping of the data to a lower-dimensional space in such a way that the variance of the data in the low-dimensional representation is maximized. Sparse coding [206–208], which finds the set of basis in which the signal has a sparse representation, is another effective linear dimension reduction technique. Nonlinear dimension-reduction techniques include manifold learning techniques such as kernel PCA [209, 210], Isomap [211], locally linear embedding (LLE) [68], Hessian LLE [212], Laplacian eigenmaps [213], local tangent space alignment (LTSA) [70] and neural network methods like autoencoders [214,215]. These techniques construct a low-dimensional data representation using a cost function that retains local properties of the data.

For supervised dimension reduction, Fisher linear discriminant (FDA) or linear discriminant analysis (LDA) is widely used [71]. LDA tries to find a good linear projection to the subspace so that samples from the same class are projected close to each other and the projected means of different classes are as father apart as possible. Nonlinear supervised dimension reduction methods include kernel methods [216,217], neural network methods with class label as hidden layers.

Supervised methods can extract features that are more discriminating with respect to the output class labels, thus has the potential to improve classification performance. However, like classification algorithms, supervised methods suffer from over-fitting with increasing input dimension and limited training samples. Therefore unsupervised and supervised methods are often combined either as a two-step process (often supervised learning after unsupervised) or into one model that is built to serve both purposes [218–220]. *Partial least squares* (PLS) is such example. PLS is a

supervised linear dimension reduction method [221] that tries to explain variance in both the input data and output class labels. PLS is closely related to PCA. PCA finds combinations of the predictors with large variance, while PLS finds combinations of the predictors that have a large covariance with the response values. PLS therefore combines information about the variances of both the predictors and the responses while also considering the correlations among them.

4.2 Cerebellar ataxia classification

In this section, we build a multi-class classifier with cerebellar shape representation as input and diagnosis (healthy or a specific cerebellar ataxia type) as output. The classifier uses dimension reduction as a preprocessing step followed by a standard classifier. For dimension reduction, we explore two linear dimension reduction methods PCA and PLS. There are three reasons for using linear methods. First, linear mappings are easy to compute. Second, linear mappings have very few parameters(often only the number of target dimensions), and are therefore less prone to over-fitting than nonlinear mappings. This is important since we are analyzing high-dimensional shape representations with few training samples. Third, linear mappings can be inverted easily. Although the analysis is carried out in the dimension reduced space, we can reconstruct and visualize the discriminant pattern in original high-dimensional shape space.

For the classifier, we explore three classifiers—linear discriminant analysis (LDA), support vector machine (SVM), and random forests. We use the shrunken centroids regularized discriminant analysis (SCRDA) [222], a modified version of LDA. We describe in detail principals of LDA and the modification, since it will be used in both disease classification and disease specific pattern visualization in Section 4.3.

Let $\mathbf{x}$ denote the feature vector of a sample in the dimension-reduced space associated with a class label $y \in \{0, 1, \ldots, C\}$. LDA assumes that the conditional probability density functions $p(\mathbf{x}|y = c), c = 0, 1, \ldots, C$, are normally distributed with common covariance $\mathbf{\Sigma}$ and different mean vectors $\boldsymbol{\mu}_c, c = 0, 1, \ldots, C$. The class

prediction problem is solved by maximizing the posterior probability, $p(y|\mathbf{x})$, that the observation belongs to a particular class. In the case of two classes, the decision criterion becomes a threshold on the dot product

$$\boldsymbol{\omega} \cdot \mathbf{x} > h, \tag{4.1}$$

for some threshold constant h, where

$$\boldsymbol{\omega} = \boldsymbol{\Sigma}^{-1} (\boldsymbol{\mu}_1 - \boldsymbol{\mu}_2). \tag{4.2}$$

$\boldsymbol{\omega}$, called *discriminant direction*, is the direction that the data from two classes are most separated when projected on a line in this direction.

Instead of using the sample covariance matrix estimation $\hat{\boldsymbol{\Sigma}}$ in the discriminant function, Guo et al.(2007) [222] use a shrunken version of the sample covariance matrix

$$\tilde{\boldsymbol{\Sigma}} = \alpha \hat{\boldsymbol{\Sigma}} + (1 - \alpha) \mathbf{I}_p, \tag{4.3}$$

where $\mathbf{I}_p$ is the $p \times p$ identity matrix and $0 \leq \alpha \leq 1$. By introducing a slightly biased covariance matrix, it stabilizes the sample covariance estimates. It also stabilizes the variance and reduces the bias of the discriminant function, leading to an improved prediction accuracy [222].

4.3 Disease specific atrophy pattern visualization

Visualization of the anatomical shapes and shape differences between different diagnosis groups are key elements in the exploration of data and in formulating and testing of hypotheses. In this section, we aim to visualize the characteristic cerebellar atrophy patterns as they change from healthy to a particular ataxia type. We consider the discriminant direction $\boldsymbol{\omega}$ between the two classes—healthy control and the ataxia type of interest—as computed in Section 4.2, since it represents a feature direction that can best differentiate the two classes. The atrophy pattern is visualized

as a series of synthetic shapes sampled along a line in the discriminant direction $\boldsymbol{\omega}$.

Given the discriminant direction $\boldsymbol{\omega}$ in the dimension-reduced space, the corresponding direction in high-dimensional shape space can be computed as

$$\mathbf{w} = \mathbf{V}\boldsymbol{\omega}, \tag{4.4}$$

where $\mathbf{V} = [\mathbf{v}_1, \mathbf{v}_2, \ldots, \mathbf{v}_d]$ and $\mathbf{v}_i$ is the ith component produced by PCA or PLS dimension reduction. In order to be representative of the data, we select the line trajectory in the direction $\mathbf{w}$ that passes through the point $\boldsymbol{\mu}$, the mean of all subjects, and we call it the *discriminant line*. The parametric representation of the discriminant line $\mathbf{s}_l$ can then be written as

$$\mathbf{s}_l(t) = \boldsymbol{\mu} + t\mathbf{w}, \quad t \in \mathbb{R}. \tag{4.5}$$

To visualize the line trajectory, we sample five equidistant points $\mathbf{s}_l(t_0 + k\Delta t),\ k = 0, 1, \ldots, 4$ on the line, and reconstruct the cerebellar shapes from the points. Figure 4.1 shows an illustration of the discriminant line and sampled shapes in the first two dimensions of the dimension-reduced space. The points are sampled so that first and third ones are the projection of the HC mean, $\boldsymbol{\mu}_{HC}$, and mean of the ataxia type of interest, $\boldsymbol{\mu}_{Ataxia}$, respectively. The shape corresponding to the 5th point $\mathbf{s}_l(t_0+4\Delta t)$ will depicting a conjectured subject with an extreme case of a particular ataxia type, so that the structural change pattern for different ataxia types can be observed more evidently.

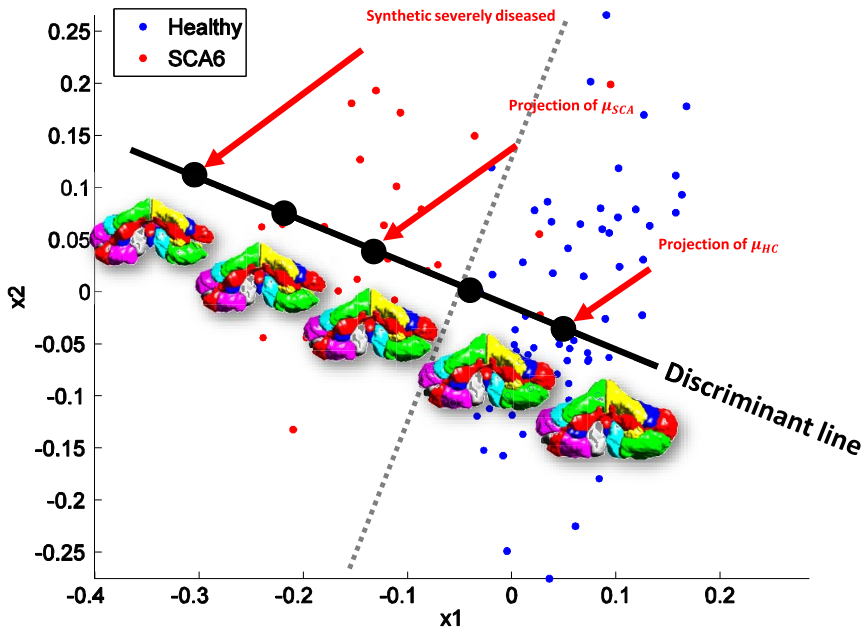

Figure 4.1: Illustration of the discriminant line and sampled shapes in the first two dimensions of the dimension-reduced space.

4.4 Results

4.4.1 Diagnosis group classification

In this experiment, we tested the proposed method on classifying healthy controls and five different ataxia types: SCA2, SCA3, SCA6, SCA8, and AT. See Table 4.1 for the number and demographic information for each diagnosis group. A leave-one-out experiment was used to evaluate the classification performance, where each of the 123 subjects was used as a test subject while the remaining 122 were used to learn the linear mapping for dimension reduction and yo train the classifier.

We compared the combinations of different cerebellar structure representations, dimension reduction methods, and classification methods. The cerebellar structure representations are:

- **ROI volumes**: volumes of 22 cerebellar lobule structures, with lobule segmentation obtained using the approach proposed in Chapter 3.

Table 4.1: Demographic information of the 123 subjects being studied. Key: N number of subjects; m/f is the male/female ratio; Age is the mean age; SD is the standard deviation of the age; healthy controls (HC); spinocerebellar ataxia type 2 (SCA2), type 3 (SCA3), type 6 (SCA6) and type 8 (SCA8); ataxia-telangiectasia (AT).

	N	(m/f)	Age	(SD)
HC	65	(28/37)	50.7	(17.7)
SCA2	4	(3/1)	48.8	(8.8)
SCA3	7	(2/5)	51.7	(9.3)
SCA6	27	(7/20)	58.4	(9.3)
SCA8	2	(2/0)	43.5	(16.3)
AT	18	(12/6)	18.3	(6.2)

- **RAVENS maps**: RAVENS maps for cerebellar GM and WM. The cerebellar GM/WM are obtained using FreeSurfer and the RAVENS maps are computed using the DRAMMS software [223].

- **Landmark**: the cerebellar lobule landmark representation, as described in Section 3.1.2.

- **Level set**: the level set representation of the whole cerebellum, as described in Section 3.1.3, combined with the level set of the cerebellar WM.

The dimension reduction methods are PCA and PLS. The classifiers are SCRDA, SVM, and random forests (RF).

Table 4.2 shows the leave-one-out classification success rate for each combination. Leave-one-out classification success rate is computed as the number of correct diagnosis predictions divided by N, the number of subjects used in the leave-one-out experiment. Among all combinations, the combination of level set representation, PCA and SCRDA obtains the highest success rate, 0.87. Regarding the cerebellar structural representations, the RAVENS maps and the level set shape representation gave the best classification performance. The RAVENS maps produces success rate above 0.8 with any combination of dimension reduction and classification method; the level set representation achieves high performance when using SCRDA as the classifier. Overall, high-dimensional representations, e.g., the RAVENS maps and the level set representation perform better than low-dimensional representation, i.e., ROI

volumes, because of the rich structural information they encode. However, the lobule landmark representation, which encodes the richest structural information, does not perform well. This may due to the error and variance introduced in the many processing steps (segmentation and correspondence finding) to compute the representation. Regarding different dimension reduction methods, PCA is slightly better than PLS. Regarding different classification methods, SCRDA performs the best.

Table 4.2: Leave-one-out classification successful rate.

	PCA			PLS		
	LDA	SVM	RF	SCRDA	SVM	RF
ROI Volumes	0.797 ± 0.036	0.528 ± 0.045	0.724 ± 0.044	0.805 ± 0.036	0.528 ± 0.045	0.748 ± 0.039
RAVENS maps	0.829 ± 0.034	0.837 ± 0.033	0.821 ± 0.035	0.821 ± 0.035	0.821 ± 0.035	0.805 ± 0.036
Landmark	0.797 ± 0.036	0.772 ± 0.038	0.780 ± 0.037	0.813 ± 0.035	0.724 ± 0.040	0.764 ± 0.038
Level set	0.870 ± 0.030	0.830 ± 0.034	0.772 ± 0.038	0.854 ± 0.032	0.780 ± 0.037	0.748 ± 0.039

Table 4.3 is an example confusion matrix between the true diagnosis and predicted diagnosis produced by the classifier with the combination of lobule landmark representation, PLS and SCRDA. We can see that the classifier predicts the majority diagnosis groups (healthy, SCA6 and AT) well. The classifier did not predict SCA2, SCA3, and SCA8 well, however. This may be due to the limited training samples that are available for these classes. A major source of error is the mistake of classifying ataxia types as healthy controls. This may because the cerebellum of patients with a short disease duration has mild atrophy, and it is therefore difficult to distinguish their cerebella from healthy subjects.

Table 4.3: Example confusion matrix.

True \Predicted	Healthy	SCA2	SCA3	SCA6	SCA8	AT
Healthy	63	0	0	2	0	0
SCA2	1	1	1	1	0	0
SCA3	4	0	3	0	0	0
SCA6	4	0	0	23	0	0
SCA8	0	0	0	0	0	2
AT	1	0	0	4	1	12

4.4.2 Disease specific atrophy pattern visualization

In this section, we show the characteristic cerebellar atrophy patterns associated with each cerebellar ataxia type. To do this we visualize the synthetic cerebellar lobule shapes sampled along the discriminant line pointing from healthy control to the ataxia type, as described in Section 4.3. Figures 4.2–4.5 show the atrophy patterns for SCA2, SCA3, SCA6, and AT computed from the two shape representations. We can see that noticeable cerebellar atrophy is observed for all ataxia types, but different ataxia types have different patterns of shape changes. In the following paragraphs we discuss the observed cerebellar atrophy pattern for the four ataxia types computed from the two shape representations.

SCA2/landmark: SCA2 has the biggest atrophy in the corpus medullare among the four ataxia types (see the shrinking corpus medullare in Figure 4.2), indicating large white matter atrophy. There is substantial atrophy in the anterior and middle lobes (see Lobules I–V in Figure 4.2 and Lobule CRUS I and II in Figure 4.4) while the caudal lobes do not change as much (see Lobules VIII, IX, and X in Figure 4.2). These observations agree with the observations in Jung et al. (2012) [103] that the volume of corpus medullare, the anterior lobe, middle lobe of SCA2 patients were reduced compared to controls while the caudal lobes are relatively preserved. The visualization also suggests that although there is atrophy in many parts of the cerebellum the overall size of the cerebellum does not change too much.

SCA2/levelset: In agreement with the observations made using the landmark representation, SCA2 has the most white matter atrophy among the four ataxia types (Figures 4.3 and 4.5). The primary and horizontal fissure become wider (Figure 4.5), indicating atrophies in anterior and middle lobes. Again the overall size of the cerebellum does not change too much.

SCA3/landmark: SCA3 has the mildest overall cerebellar atrophy among the four ataxia types, with no substantial change of the size. Evidence of lobule atrophy in SCA3 is still apparent, however. There is noticeable atrophy in Lobule CRUS I (Figure 4.4) and Lobule IX (Figure 4.2); but the degree of atrophy is much less than

that in the other three types. SCA3 has larger corpus medullare atrophy than that in SCA6 and AT, but not as large as that in SCA2. These observations agree with the observations in Burk et al. (1996) [97] and Lukas et al. (2006) [105].

SCA3/levelset: In agreement with the observations made using the landmark representation, SCA3 has the mildest whole cerebellum volume change among the four ataxia types, with no substantial size change of the whole cerebellum. The horizontal fissure becomes wider (Figure 4.5), indicating there is still atrophy in the posterior lobes, but the atrophy is much less than the other three types.

SCA6/landmark: SCA6 has substantial atrophy in almost all parts of the cerebellum and a decrease in the overall size of the cerebellum (Figures 4.2 and 4.4). SCA6 has less atrophy in corpus medullare than that of SCA2 and SCA3 (Figure 4.2). These observations agree with the observations in Jung et al. (2012) [104] that in comparison to SCA2, SCA6 has larger atrophy in posterior-inferior regions of the cerebellum but less atrophy in the corpus medullare. These results also agree with the voxel-based morphometry study on SCA3 and SCA6 in Lukas et al. (2006) [105] in which significant grey matter loss was found in SCA6 in hemispheric lobules bilaterally as well as in the vermis, and white matter analysis revealed significant changes in SCA3 whereas no significant white matter reduction was found in SCA6 patients.

SCA6/levelset: As also observed in the results from the landmark representation, there is substantial decrease in the overall size of the cerebellum (Figures 4.3 and 4.5). Again, SCA6 has less amount of cerebellar white matter atrophy than that of SCA2 and SCA3 (Figures 4.3 and 4.5).

AT/landmark: AT has the most apparent whole cerebellum atrophy (Figures 4.2 and 4.4). The size of the cerebellum decreases rapidly when moving from healthy to AT. All lobules shrink, especially the middle lobes (Figure 4.4). These observations agree with the observations in Tavani et al. (2003) [100] that all parts of the cerebellar hemispheres and vermis undergo moderate to severe atrophy in AT patients with ages between 9 and 40, and the lateral part of cerebellar hemispheres has the most severe atrophy.

AT/levelset: As also observed in the results from the landmark representation,

AT has the most significant whole cerebellum atrophy (Figures 4.3 and 4.5). The size of the cerebellum decreases rapidly when moving from healthy to AT along the discriminant direction. All lobules shrink, especially the lateral parts of the cerebellar hemispheres and the superior vermis at the top of the cerebellum.

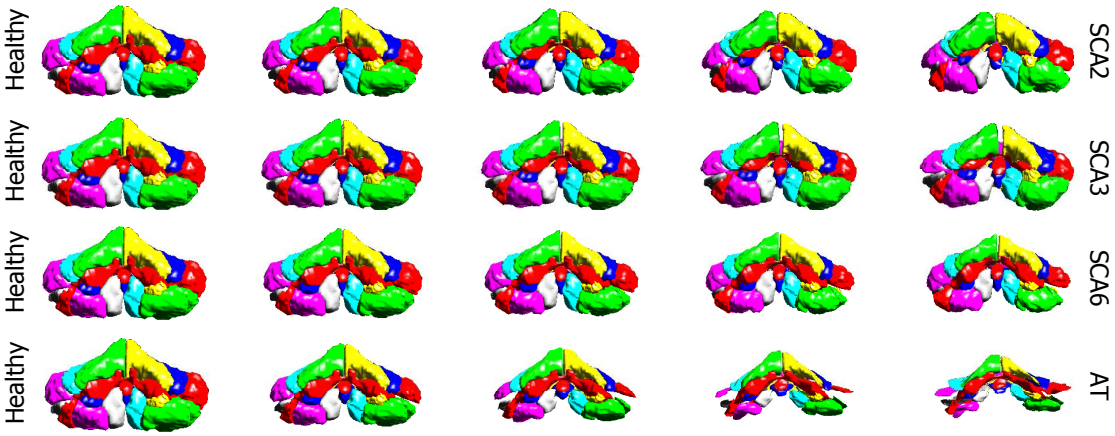

Figure 4.2: Cerebellar lobule shape changes from healthy controls to four different ataxia types viewing from the front of the cerebellum. Each column shows in order one of the five equidistant points sampled on the discriminant line, with the first column being the projection of the HC mean and the third column being the projection of the mean of a ataxia type.

4.5 Summary

In this chapter, we presented a cerebellar shape analysis pipeline to classify healthy and different disease types and to identify characteristic cerebellar atrophy pattern associated with different cerebellar ataxia types. A leave-one-out classification experiment demonstrated the effectiveness of the proposed classification method. Characteristic cerebellar atrophy pattern for different ataxia types were visualized by sampling along the discriminant direction between healthy controls and the ataxia types. The observed shape change patterns are consistent with known patterns of atrophy in these ataxia types. It provides intuitive and visual understanding about the changes of overall size and shape change of the cerebellum, as well as the details of individual sub-structures.

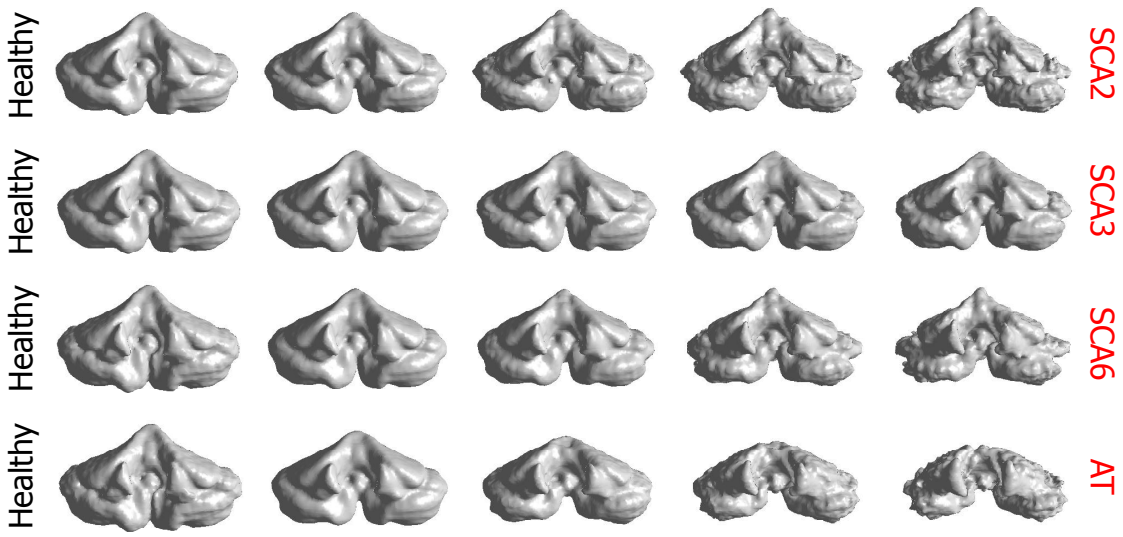

Figure 4.3: Cerebellar lobule shape changes from healthy controls to four different ataxia types viewing from the front of the cerebellum. Each column shows in order one of the five equidistant points sampled on the discriminant line, with the first column being the projection of the HC mean and the third column being the projection of the mean of a ataxia type.

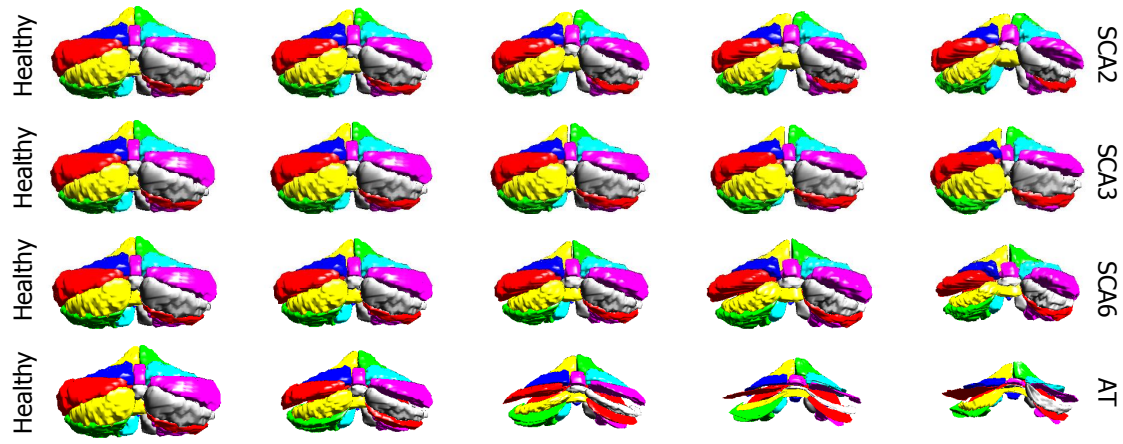

Figure 4.4: Cerebellar lobule shape changes from healthy controls to four different ataxia types viewing from the back of the cerebellum. Each column shows in order one of the five equidistant points sampled on the discriminant line, with the first column being the projection of the HC mean and the third column being the projection of the mean of a ataxia type.

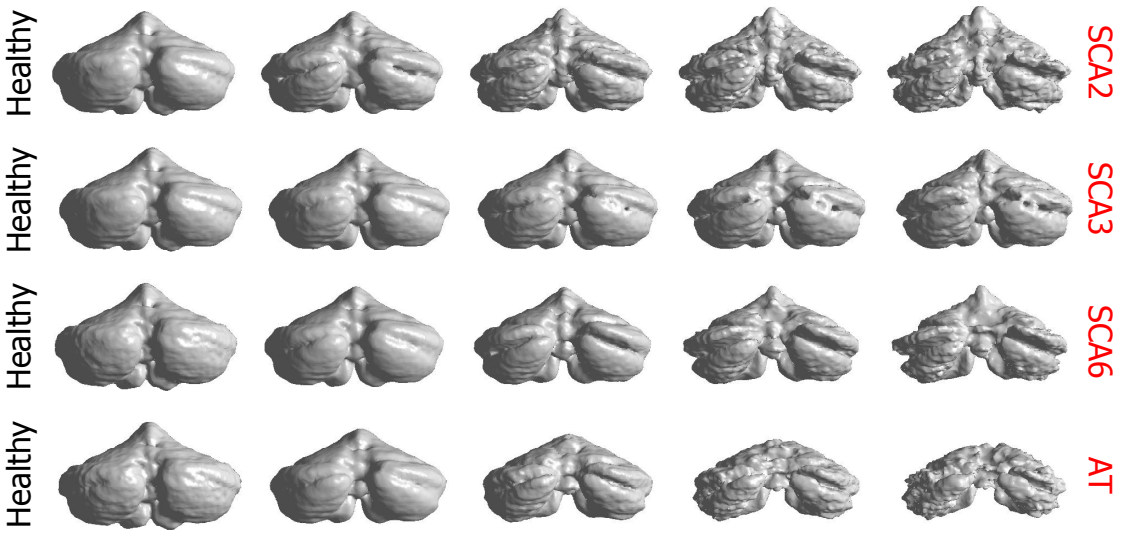

Figure 4.5: Cerebellar lobule shape changes from healthy controls to four different ataxia types viewing from the back of the cerebellum. Each column shows in order one of the five equidistant points sampled on the discriminant line, with the first column being the projection of the HC mean and the third column being the projection of the mean of a ataxia type.

Chapter 5

Functional score regression and atrophy pattern visualization

In the previous chapter, we developed classifiers for classifying ataxia types and studied the cerebellar atrophy patterns for different disease types. In this chapter, we develop regressors to predict functional scores and to identify function specific atrophy patterns.

The remainder of the chapter is organized as follows. In Section 5.1, we present background on regression methods. In Section 5.2 we build regressors to predict functional scores. The regressors are tested in Section 5.4.1 using leave-one-out cross validation with an extensive comparison of combinations using different cerebellar structural representations, different classifiers, and dimension reduction techniques. In Section 5.3, we present a method to visualize cerebellar atrophy pattern associated with different functional scores. In Section 5.4.2, we study the cerebellar atrophy pattern of representative scores related to motor and cognitive function.

5.1 Regression

Regression is the process of estimating the relationship between one or more dependent variables and one or more independent variables, or predictor variables. The relationship is often used to predict the dependent variables given new observations

of predictor variables. Regression is a supervised learning technique. Classification learns from training data a function that predicts categorical variable from input predictor variables, while regression learns a function that predicts continuous variables. Next we briefly introduce the two regression techniques that we use in our approach: ridge regression and random forest regression. Here we only discuss the case of one dependent variable.

Ridge regression is one of the linear regression methods. A linear regression model assumes that the dependent variable is a linear combination of the predictor variables and a constant. Among the many estimation methods for linear regression model, the least square estimator is the simplest and most widely used one. The least square estimator, called *ordinary least squares* (OLS), minimizes the sum of squared residuals, and leads to a closed form solution for the linear coefficients. OLS is an unbiased estimator but suffers from high variance. A bias-variance tradeoff can be made by adding a penalty term in the least square objective function. When the penalty term is the l_2 norm of the regression coefficients, the resulting approach is called ridge regression. Ridge regression reduces the variance of the estimate by introducing a limited amount of bias and generally yields better predictions than the OLS solution.

Random forests can be used for regression by replacing the decision tree with a regression tree and averaging the predictions from all of the regression trees [149]. A regression tree is similar to a decision tree except that the output variable takes ordered values and often a regression model is fitted to each node to give the prediction of the output variable. Like random forest classification, random forest regression is accurate and robust. It can model complex nonlinear relationships between the input feature vector and output variable and at the same time largely avoid over-fitting.

5.2 Functional score prediction

In this section, we build a regressor with a cerebellar shape representation as input and a functional score as output. As in classification, linear dimension reduction (PCA or PLS) is performed on the high-dimensional input feature vector. For the

regressor, we explore two methods: ridge regression and random forest regression. We describe in detail the principals of ridge regression since it will be used in both functional score prediction and function specific pattern visualization in Section 5.3.

Let $\mathbf{x}_i \in \mathcal{R}^{p\times 1}$ denote the feature vector of the ith training sample in the dimension-reduced space associated with a functional score $y_i \in \mathcal{R}$. In matrix form, $\mathbf{X} = [\mathbf{x}_1, \mathbf{x}_2, \ldots, \mathbf{x}_n]^T$ and $\mathbf{y} = [y_1, y_2, \ldots, y_n]^T$. Ridge regression finds the regression coefficients $\boldsymbol{\beta} \in \mathcal{R}^{p\times 1}$ that minimizes the objective function

$$f(\boldsymbol{\beta}) = \sum_{i=1}^{n} \left(y_i - \mathbf{x}_i^T \beta\right)^2 + \lambda \sum_{j=1}^{p} \beta_j^2 = \|\mathbf{y} - \mathbf{X}\boldsymbol{\beta}\|_2^2 + \lambda \|\boldsymbol{\beta}\|_2^2 , \tag{5.1}$$

where $\lambda \geq 0$ is the weight of the penalty term, often empirically determined.

When the intercept term is included in the regression, the intercept estimate ends up just being $\boldsymbol{\mu}_y$. Often $\mathbf{X}$ and $\mathbf{y}$ are centered before regression and then the intercept term can be ignored.

The geometric interpretation of regression coefficients is that vector $\boldsymbol{\beta} \in \mathcal{R}^{p\times 1}$ is a direction in p-dimensional space that when the input observations $\mathbf{x}$ are projected to this direction, i.e. $\boldsymbol{\beta}^T\mathbf{x}$, they have the biggest correlation with output variable y. We call $\boldsymbol{\beta}$ the *regression direction*.

The functional score of a new observation $\mathbf{x}$, centered, can then be predicted as $\hat{y}(\mathbf{x}) = \boldsymbol{\beta}^T\mathbf{x} + \boldsymbol{\mu}_y$.

5.3 Function specific atrophy pattern visualization

In this section, we aim to visualize the characteristic cerebellar atrophy patterns as a functional score changes from normal to increasing disability. We consider the regression direction $\boldsymbol{\beta}$ of the functional score, as computed in Section 5.2, since it represents the direction in feature space that correlates most with the functional score. As in Section 4.3, we visualize the atrophy pattern of a functional score as a series of synthetic shapes sampled along a line in the discriminant direction $\boldsymbol{\beta}$.

Given the regression direction $\boldsymbol{\beta}$ in the dimension-reduced space, the correspond-

ing direction in high-dimensional shape space can be computed as

$$\mathbf{b} = \mathbf{V}\boldsymbol{\beta}, \tag{5.2}$$

where $\mathbf{V} = [\mathbf{v}_1, \mathbf{v}_2, \ldots, \mathbf{v}_d]$ and $\mathbf{v}_i$ is the ith component produced by PLS dimension reduction. In order to be representative of the data, we select the line trajectory in the direction $\mathbf{b}$ that passes through the point $\boldsymbol{\mu}$, the mean of all subjects, and we call it the *regression line*. The parametric representation of the regression line $\mathbf{s}_l$ can then be written as

$$\mathbf{s}_l(t) = \boldsymbol{\mu} + t\mathbf{b}, \quad t \in \mathbb{R}. \tag{5.3}$$

To visualize the line trajectory, we sample five equidistant points $\mathbf{s}_l(t_0 + k\Delta t),\ k = 0, 1, \ldots, 4$ on the line, and reconstruct the cerebellar shapes from the points. The points are sampled so that the first and fifth points predict (by regression function $\hat{y}$) the lowest and highest functional score in the training data.

5.4 Results

5.4.1 Functional score prediction

In this experiment, we tested the proposed method on predicting functional staging score for ataxia (FSFA). FSFA is a subset of the unified ataxia disorders rating scale [224]. FSFA rates a subject from 0 to 6, where a higher FSFA value indicates more functional losses. 122 subjects with FSFA scores were used for the study. The 122 subjects include 30 healthy controls and 92 patients with different types of cerebellar ataxia. See Table 5.1 for the number and demographic information for the healthy controls and patients. A leave-one-out experiment was used to evaluate the regression performance, where each of the 122 subjects was used as a test subject while the remaining 121 were used to learn the linear mapping for dimension reduction and train the regressor.

We compared the combinations of different cerebellar structure representations,

Table 5.1: Demographic information of the 122 subjects used in the study. Key: N number of subjects; m/f is the male/female ratio; Age is the mean age; SD is the standard deviation of the age.

	N	(m/f)	Age	(SD)
Healthy	30	(14/16)	56.3	(14.2)
Patients	92	(45/47)	51.2	(16.3)

dimension reduction methods, and regression methods. The cerebellar structure representations are the same four representations used in Section 4.4.1: ROI volumes, GM+WM RAVENS maps, lobule landmark representation and CB+WM level set representation. The dimension reduction methods are PCA and PLS. The regression methods are ridge regression (RR) and random forest regressor (RF).

Table 5.2 shows the leave-one-out root mean square prediction error (RMSE) for each combination. Comparing different structural representations, the RAVENS map has the best performance. Unlike in classification, ROI volumes have compatible performance as high-dimensional representations. Again, the lobule landmark representation, which encodes the richest structural information, does not perform well. This may be due to the errors introduced in the many processing steps (segmentation and correspondence finding) to compute the representation. Regarding different dimension reduction methods, PCA is slightly better than PLS. Regarding different regression methods, random forest regression has better performance than ridge regression. Figure 5.1 shows the predicted FSFA verses the true FSFA from all the test subjects in the leave-one-out experiment (combination of landmark shape representation, PCA and ridge regression).

Table 5.2: FSFA root mean square prediction error (RMSE) of the leave-one-out experiments.

	PCA		PLS	
	RR	RF	RR	RF
ROI Volumes	1.22	1.27	1.34	1.24
RAVENS maps	1.21	1.15	1.23	1.14
Landmark	1.26	1.25	1.63	1.28
Level set	1.26	1.24	1.34	1.24

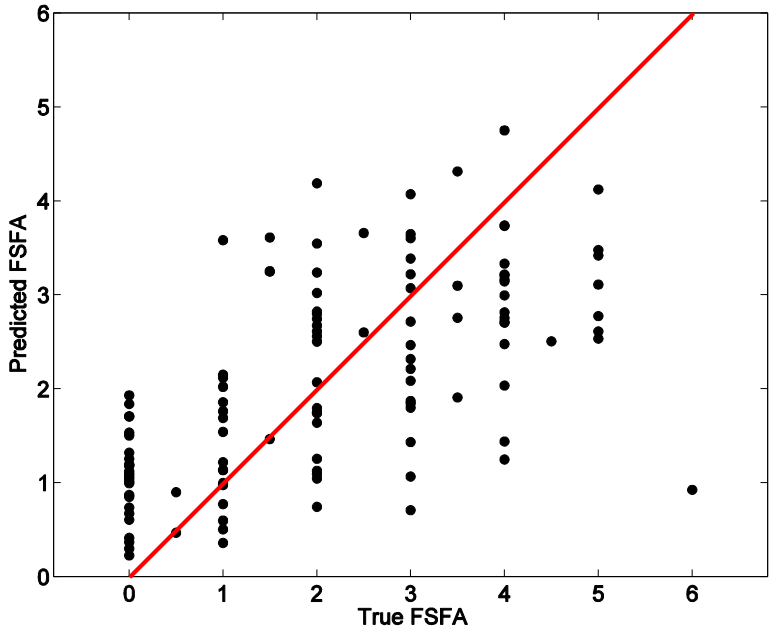

Figure 5.1: Predicted FSFA vs. true FSFA in the leave-one-out experiment for the combination of landmark shape representation, PCA dimension reduction and ridge regression.

5.4.2 Function specific atrophy pattern visualization

In this section, we use the cerebellar lobule landmark presentation and show the cerebellar atrophy patterns associated with a specific functional score. We visualize the synthetic cerebellum lobule shapes sampled along the regression line computed

from the regression analysis of the functional score, as described in Section 5.3. We chose 65 subjects with all functional scores evaluated. The 65 subjects include 18 healthy controls and 37 patients with different types of cerebellar ataxia. See Table 5.3 for the number and demographic information for the healthy controls and patients.

Table 5.3: Demographic information of the 65 subjects used in the study. Key: N number of subjects; m/f is the male/female ratio; Age is the mean age; SD is the standard deviation of the age.

	N	(m/f)	Age	(SD)
Healthy	18	(7/11)	53.9	(14.9)
Patients	37	(19/28)	53.6	(12.8)

Figures 5.2 and 5.3 show the atrophy pattern for FSFA and the Hooper test scores, respectively. As introduced in Section 5.4.1, FSFA is a rating score quantifying motor function. The Hooper test evaluates the individual's ability to organize visual stimuli [225], thus focusing more on the cognitive function. We can see that there is substantial global atrophy and overall size change of the cerebellum as the FSFA moves from normal to disease. For the Hooper test score, there is no apparent size change of the cerebellum as the score moves from normal to disease. There is almost no shape changes in lobules I–V and lobules VI. CRUS I and CRUS II have the most atrophy. This partially agrees with Imamizu et al. (2003) [15] that "anterior lobe and intermediate parts of posterior lobe are related to motor and somatosensory functions, whereas lateral posterior cerebellum is related to cognitive functions".

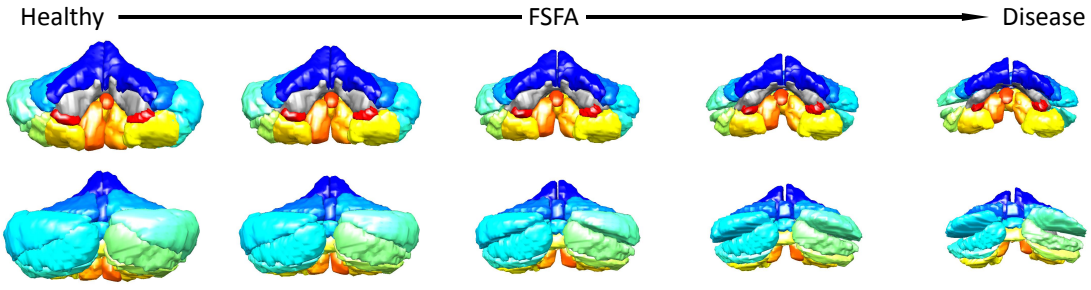

Figure 5.2: Cerebellar atrophy pattern associated with FSFA score.

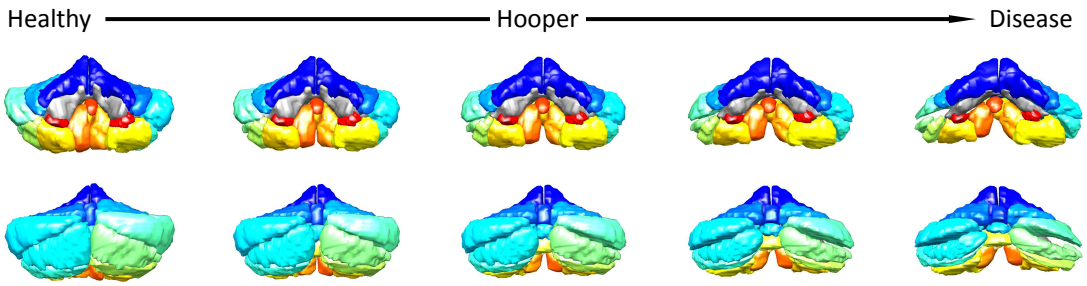

Figure 5.3: Cerebellar atrophy pattern associated with Hooper test score.

5.5 Summary

In this chapter, we presented cerebellar shape analysis method to predict functional scores and visualize the cerebellar atrophy pattern associated a functional score. A leave-one-out experiment demonstrated the effectiveness of the proposed regression method. We visualized cerebellar atrophy patterns associated with two functional scores: FSFA and the Hooper test score. The observed atrophy patterns partially agree with a previous study on the topological organization of functions in the cerebellum. It provides intuitive and visual understanding about the changes of overall size and shape change of the cerebellum, as well as the details of individual substructures.

Chapter 6

Conclusion and future work

This thesis focus on shape analysis of the cerebellum in cerebellar ataxia, with special focus on: 1) developing automated and accurate method for segmenting fine anatomical divisions of the cerebellum; 2) exploring highly informative representation of the cerebellar structures; 3) predicting ataxia types and functional decline based on the highly informative representations; and 4) identifying disease and function specific cerebellar atrophy patterns. In this chapter, we summarize the contributions and propose directions for future research.

6.1 Cerebellar Lobule Segmentation

In Chapter 2, we proposed an automated method for segmenting cerebellar lobules from MR images. The proposed method combines multi-atlas label fusion result and tissue/boundary classification in a graph cut segmentation framework. The multi-atlas component ensures the correct localization of different lobules, and tissue/boundary classification promotes accurate delineation of lobule boundaries.

6.1.1 Results

- The proposed method was assessed on a cohort of 15 subjects, including both healthy controls and patients with various degrees of cerebellar atrophy, for

which expert manual labels are also available. The Wilcoxon two-sided signed rank test on the 15 subjects indicated that the proposed method improved the segmentation results over the other two state-of-the-art segmentation methods significantly in terms of average area weighted Dice similarity coefficients, with a p-value of 1.2×10^{-4} when compared with ACCLAIM and 3.3×10^{-3} when compared with NL-STAPLE. The improvements are most substantial on subjects with moderate to large cerebellar atrophy.

- The method was further validated on a larger cohort containing both normal controls and patients experiencing cerebellar ataxia. Quantitative analysis of the lobule volumes show distinct patterns of volume changes associated with different SCA subtypes; the result is consistent with previous findings in which cerebellar lobules were manually labeled by experts.

6.1.2 Future directions

- There is a bias towards smooth boundaries in the graph cuts segmentation framework; this is undesirable for segmenting anatomical structures with complex boundaries. There have been works on eliminating this bias in graph cuts segmentation, which can be incorporated in the algorithm to improve the segmentation accuracy.

- The result of the algorithm depends (moderately) on the atlases used in the multi-atlas labeling and tissue / boundary training process, which might bias the segmentation result towards the majority diagnosis of the atlases. Some data driven atlas selection methods could be incorporated to improve the accuracy.

6.2 Cerebellar shape representations

In Chapter 3, we proposed two shape representations to characterize cerebellar structures. First, we proposed a landmark shape representation of the collection of cerebellar lobules. It is constructed by extracting dense homologous landmarks on the

boundary surfaces of cerebellar sub-structures. We addressed the difficulty in establishing dense corresponding points on multiple 3D objects across subjects by a two-step non-rigid point set registration. The second representation we proposed is a level set based whole cerebellar shape representation. This representation is relatively easy to compute and thus less prone to algorithm errors.

6.2.1 Results

- We demonstrated the representational power of the two shape representation by studying the cerebellar shape variations of specific groups of subjects. The principal shape modes computed by the two representations are consistent with each other. However, the cerebellar lobule landmark representation provides much more details on individual structures within the cerebellum.

- In Chapters 4 and 5, we compared the proposed shape representations with existing cerebellar structure representations like ROI volumes and RAVENS maps in disease classification and functional score prediction. Overall, the level set shape representation performed better or comparable to other representations while the landmark representation performed worse in most cases. This may due to the error and variance introduced in the many processing steps (segmentation and correspondence finding) to compute the representation.

- In Chapters 4 and 5, we visualized the disease/function specific cerebellar atrophy patterns using the two representations. Again they provided consistent results, and the cerebellar lobule landmark representation was able to provide more details on individual structures.

6.2.2 Future directions

The bad performance of lobule landmark representation in disease / function prediction results indicates that the landmark generation process, mainly the two-step non-rigid point set registration, introduces errors or unintended shape variations.

The correspondence finding process could be improved, for example, by imposing constraints and regularization on the non-rigid point set registration.

6.3 Disease classification and atrophy pattern visualization

In Chapter 4, we presented a shape analysis pipeline to classify healthy control and different ataxia types, and to visualize the characteristic cerebellar atrophy patterns for different ataxia types. Linear dimension reduction is first applied to reduce the data dimension. The classifier is built in a dimension-reduced space to predict disease types. The characteristic atrophy pattern for each ataxia type was visualized by sampling along the discriminant direction between healthy controls and the ataxia type.

6.3.1 Results

- Experimental results show that the proposed method can successfully classify healthy controls and different ataxia types. Different combinations of cerebellar structure representations, dimension reduction, and classification methods were compared. Among all combinations, the combination of level set representation, PCA and SCRDA obtains the highest success rate, 0.87. Regarding the cerebellar structural representations, the RAVENS maps and the level set shape representation achieve the best classification performance. The RAVENS maps obtains success rate above 0.80 with any combination of dimension reduction and classification method; the level set representation obtains success rate above 0.85 when using SCRDA as the classifier. Regarding different dimension reduction methods, PCA is slightly better than PLS. Regarding different classification methods, a regularized modification of linear discriminant analysis gave the best performance.

- We visualized cerebellar atrophy patterns associated with two functional scores:

FSFA and the Hooper test score. The visualized cerebellar atrophy patterns were consistent with the regional volume decreases observed in previous studies in cerebellar ataxia. Compared to existing analysis method, the proposed shape analysis pipeline provides an intuitive and detailed visualization of differences of the overall size and shape of the cerebellum, as well as that of individual lobules.

6.3.2 Future directions

- Although the current linear dimension reduction and discriminant analysis produce satisfying results, other dimension reduction and discriminant analysis methods like sparse representation, manifold learning and deep neural networks could be explored, but with careful handling of the high-dimensionality of the data.

6.4 Functional score regression and atrophy pattern visualization

In Chapter 5, we presented a shape analysis pipeline to predict functional scores, and to visualize the function specific atrophy patterns. As in discriminant analysis, linear dimension reduction was applied to generate the low-dimensional feature vector that are both representative of the input data and correlates with output functional scores. The regressor is built in the dimension-reduced space to predict functional scores. Functional specific atrophy pattern is visualized by sampling along the regression line.

- We demonstrated the effectiveness of the regression on predicting one of the functional scores—functional staging score for ataxia (FSFA). We compared the combinations of different cerebellar structure representations, different dimension reduction, and regression methods. Regarding the cerebellar structural

representations, the RAVENS maps gave the best prediction performance. Regarding different dimension reduction methods, PCA is slightly better than PLS. Regarding different regression methods, random forest regression has better performance than ridge regression.

- The visualized function specific cerebellar atrophy patterns partially agrees with a previous study on the topological organization of cerebellar functions. Compared to existing analysis method, the proposed method provides an intuitive and detailed visualization of changes of overall size and shape of the cerebellum, as well as that of individual lobules, associated with the degeneration of a specific function.

6.4.1 Future directions

- As pointed out in Section 6.3, nonlinear dimension reduction and regression methods like manifold learning and deep neural networks could be explored, but with careful handling of the high-dimensionality of the data.

- Since ataxia patients often have functional loss in different aspects, the different functional scores are correlated. Future work include decorrelating the effects of different functional scores, and identifying more specific atrophy patterns for a functional score.

- Function specific pattern might vary with other variables like disease type, age, gender. With enough samples, these variables should be included in the regression analysis.

6.5 Overall perspective

The main goal of the work presented in this thesis was to contribute to the morphometric analysis of the cerebellum, where currently relatively limited works have been done compared to the study of the cerebrum. This work contributes in many ways

from the ROI segmentation and shape representations to shape based prediction and visualization methods. It is hoped that this research has provided new tools and insights in the morphometric analysis of the cerebellum, and will help to promote future developments in the general fields of brain image analysis.

Bibliography

[1] M. Ito, "Neural design of the cerebellar motor control system," *Brain Research*, vol. 40, no. 1, pp. 81–84, 1972.

[2] M. Itō, *The cerebellum and neural control*. Raven Press, 1984.

[3] H. C. Leiner, A. L. Leiner, and R. S. Dow, "Does the cerebellum contribute to mental skills?," *Behavioral Neuroscience*, vol. 100, no. 4, p. 443, 1986.

[4] J. D. Schmahmann, "An emerging concept: the cerebellar contribution to higher function," *Archives of Neurology*, vol. 48, no. 11, pp. 1178–1187, 1991.

[5] M. Manto, "The cerebellum, cerebellar disorders, and cerebellar researchâĂŤtwo centuries of discoveries," *The Cerebellum*, vol. 7, no. 4, pp. 505–516, 2008.

[6] D. Marmolino and M. Manto, "Past, present and future therapeutics for cerebellar ataxias," *Current Neuropharmacology*, vol. 8, no. 1, p. 41, 2010.

[7] T. Klockgether and H. Paulson, "Milestones in ataxia," *Movement Disorders*, vol. 26, no. 6, pp. 1134–1141, 2011.

[8] M. P. Laakso, G. B. Frisoni, M. Könönen, M. Mikkonen, A. Beltramello, C. Geroldi, A. Bianchetti, M. Trabucchi, H. Soininen, and H. J. Aronen, "Hippocampus and entorhinal cortex in frontotemporal dementia and Alzheimer's disease: a morphometric MRI study," *Biological Psychiatry*, vol. 47, no. 12, pp. 1056–1063, 2000.

[9] G. Karas, E. Burton, S. Rombouts, R. Van Schijndel, J. OâĂŹBrien, P. Scheltens, I. McKeith, D. Williams, C. Ballard, and F. Barkhof, "A comprehensive study of gray matter loss in patients with alzheimer's disease using optimized voxel-based morphometry," *NeuroImage*, vol. 18, no. 4, pp. 895–907, 2003.

[10] S. Klöppel, C. M. Stonnington, C. Chu, B. Draganski, R. I. Scahill, J. D. Rohrer, N. C. Fox, C. R. Jack, J. Ashburner, and R. S. Frackowiak, "Automatic classification of MR scans in Alzheimer's disease," *Brain*, vol. 131, no. 3, pp. 681–689, 2008.

[11] J. Kassubek, F. D. Juengling, T. Kioschies, K. Henkel, J. Karitzky, B. Kramer, D. Ecker, J. Andrich, C. Saft, P. Kraus, A. J. Aschoff, A. C. Ludolph, and G. B. Landwehrmeyer, "Topography of cerebral atrophy in early Huntington's disease:

a voxel based morphometric MRI study," *Journal of Neurology, Neurosurgery & Psychiatry*, vol. 75, no. 2, pp. 213–220, 2004.

[12] G. Douaud, V. Gaura, M.-J. Ribeiro, F. Lethimonnier, R. Maroy, C. Verny, P. Krystkowiak, P. Damier, A.-C. Bachoud-Levi, and P. Hantraye, "Distribution of grey matter atrophy in Huntington's disease patients: a combined ROI-based and voxel-based morphometric study," *NeuroImage*, vol. 32, no. 4, pp. 1562–1575, 2006.

[13] E. H. Aylward, "Change in MRI striatal volumes as a biomarker in preclinical Huntington's disease," *Brain Research Bulletin*, vol. 72, no. 2, pp. 152–158, 2007.

[14] J. D. Schmahmann, J. Doyon, D. McDonald, C. Holmes, K. Lavoie, A. S. Hurwitz, N. Kabani, A. Toga, A. Evans, and M. Petrides, "Three-dimensional MRI atlas of the human cerebellum in proportional stereotaxic space," *NeuroImage*, vol. 10, no. 3, pp. 233–260, 1999.

[15] H. Imamizu, T. Kuroda, S. Miyauchi, T. Yoshioka, and M. Kawato, "Modular organization of internal models of tools in the human cerebellum," *Proceedings of the National Academy of Sciences*, vol. 100, no. 9, pp. 5461–5466, 2003.

[16] J. X. O'Reilly, C. F. Beckmann, V. Tomassini, N. Ramnani, and H. Johansen-Berg, "Distinct and overlapping functional zones in the cerebellum defined by resting state functional connectivity," *Cerebral Cortex*, vol. 20, no. 4, pp. 953–965, 2010.

[17] C. J. Stoodley and J. D. Schmahmann, "Functional topography in the human cerebellum: a meta-analysis of neuroimaging studies," *NeuroImage*, vol. 44, no. 2, pp. 489–501, 2009.

[18] C. J. Stoodley and J. D. Schmahmann, "Evidence for topographic organization in the cerebellum of motor control versus cognitive and affective processing," *Cortex*, vol. 46, no. 7, pp. 831–844, 2010.

[19] C. J. Stoodley, E. M. Valera, and J. D. Schmahmann, "Functional topography of the cerebellum for motor and cognitive tasks: an fMRI study," *NeuroImage*, vol. 59, no. 2, pp. 1560–1570, 2012.

[20] R. L. Buckner, F. M. Krienen, A. Castellanos, J. C. Diaz, and B. T. Yeo, "The organization of the human cerebellum estimated by intrinsic functional connectivity," *Journal of Neurophysiology*, vol. 106, no. 5, pp. 2322–2345, 2011.

[21] J. H. S. of Medicine Ataxia Center, "Diagnosing ataxia." Available at `http://www.hopkinsmedicine.org/neurology_neurosurgery/centers_clinics/movement_disorders/ataxia/conditions/ataxia_diagnosis.html`.

[22] T. Schmitz-Hübsch, S. Tezenas du Montcel, L. Baliko, S. Boesch, S. Bonato, R. Fancellu, P. Giunti, C. Globas, J.-S. Kang, B. Kremer, *et al.*, "Reliability and validity of the international cooperative ataxia rating scale: a study in 156 spinocerebellar ataxia patients," *Movement Disorders*, vol. 21, no. 5, pp. 699–704, 2006.

[23] T. Schmitz-Hübsch, S. T. Du Montcel, L. Baliko, J. Berciano, S. Boesch, C. Depondt, P. Giunti, C. Globas, J. Infante, J.-S. Kang, *et al.*, "Scale for the assessment and rating of ataxia – development of a new clinical scale," *Neurology*, vol. 66, no. 11, pp. 1717–1720, 2006.

[24] D. D. Blatter, E. D. Bigler, S. D. Gale, S. C. Johnson, C. V. Anderson, B. M. Burnett, N. Parker, S. Kurth, and S. D. Horn, "Quantitative volumetric analysis of brain MR: normative database spanning 5 decades of life.," *American Journal of Neuroradiology*, vol. 16, no. 2, pp. 241–251, 1995.

[25] A. Convit, M. De Leon, C. Tarshish, S. De Santi, W. Tsui, H. Rusinek, and A. George, "Specific hippocampal volume reductions in individuals at risk for Alzheimer's disease," *Neurobiology of Aging*, vol. 18, no. 2, pp. 131–138, 1997.

[26] R. Insausti, K. Juottonen, H. Soininen, A. M. Insausti, K. Partanen, P. Vainio, M. P. Laakso, and A. Pitkänen, "MR volumetric analysis of the human entorhinal, perirhinal, and temporopolar cortices.," *American Journal of Neuroradiology*, vol. 19, no. 4, pp. 659–671, 1998.

[27] A. Convit, J. De Asis, M. De Leon, C. Tarshish, S. De Santi, and H. Rusinek, "Atrophy of the medial occipitotemporal, inferior, and middle temporal gyri in non-demented elderly predict decline to Alzheimer's disease," *Neurobiology of Aging*, vol. 21, no. 1, pp. 19–26, 2000.

[28] C. R. Jack, R. C. Petersen, Y. C. Xu, S. C. Waring, P. C. O'Brien, E. G. Tangalos, G. E. Smith, R. J. Ivnik, and E. Kokmen, "Medial temporal atrophy on MRI in normal aging and very mild Alzheimer's disease," *Neurology*, vol. 49, no. 3, pp. 786–794, 1997.

[29] C. Jack, R. C. Petersen, Y. Xu, P. C. O'Brien, G. E. Smith, R. J. Ivnik, E. G. Tangalos, and E. Kokmen, "Rate of medial temporal lobe atrophy in typical aging and Alzheimer's disease," *Neurology*, vol. 51, no. 4, pp. 993–999, 1998.

[30] K. Juottonen, M. Laakso, R. Insausti, M. Lehtovirta, A. Pitkänen, K. Partanen, and H. Soininen, "Volumes of the entorhinal and perirhinal cortices in Alzheimer's disease," *Neurobiology of Aging*, vol. 19, no. 1, pp. 15–22, 1998.

[31] M. P. DelBello, S. M. Strakowski, M. E. Zimmerman, J. M. Hawkins, and K. W. Sax, "MRI analysis of the cerebellum in bipolar disorder: a pilot study," *Neuropsychopharmacology*, vol. 21, no. 1, pp. 63–68, 1999.

[32] Y. Xu, C. Jack, P. OâĂŹbrien, E. Kokmen, G. Smith, R. Ivnik, B. Boeve, R. Tangalos, and R. Petersen, "Usefulness of MRI measures of entorhinal cortex versus hippocampus in AD," *Neurology*, vol. 54, no. 9, pp. 1760–1767, 2000.

[33] T. Ichimiya, Y. Okubo, T. Suhara, and Y. Sudo, "Reduced volume of the cerebellar vermis in neuroleptic-naive schizophrenia," *Biological Psychiatry*, vol. 49, no. 1, pp. 20–27, 2001.

[34] D. H. Mathalon, E. V. Sullivan, K. O. Lim, and A. Pfefferbaum, "Progressive brain volume changes and the clinical course of schizophrenia in men: a longitudinal magnetic resonance imaging study," *Archives of General Psychiatry*, vol. 58, no. 2, pp. 148–157, 2001.

[35] G. Chetelat and J.-C. Baron, "Early diagnosis of Alzheimer's disease: contribution of structural neuroimaging," *NeuroImage*, vol. 18, no. 2, pp. 525–541, 2003.

[36] N. Raz, U. Lindenberger, K. M. Rodrigue, K. M. Kennedy, D. Head, A. Williamson, C. Dahle, D. Gerstorf, and J. D. Acker, "Regional brain changes in aging healthy adults: general trends, individual differences and modifiers," *Cerebral Cortex*, vol. 15, no. 11, pp. 1676–1689, 2005.

[37] L. Clarke, R. Velthuizen, M. Camacho, J. Heine, M. Vaidyanathan, L. Hall, R. Thatcher, and M. Silbiger, "MRI segmentation: methods and applications," *Magnetic Resonance Imaging*, vol. 13, no. 3, pp. 343–368, 1995.

[38] D. L. Pham, C. Xu, and J. L. Prince, "Current methods in medical image segmentation," *Annual Review of Biomedical Engineering*, vol. 2, no. 1, pp. 315–337, 2000.

[39] M. A. Balafar, A. R. Ramli, M. I. Saripan, and S. Mashohor, "Review of brain MRI image segmentation methods," *Artificial Intelligence Review*, vol. 33, no. 3, pp. 261–274, 2010.

[40] J. Ashburner and K. J. Friston, "Voxel-based morphometry–the methods," *NeuroImage*, vol. 11, no. 6, pp. 805–821, 2000.

[41] J. Ashburner and K. J. Friston, "Why voxel-based morphometry should be used," *NeuroImage*, vol. 14, no. 6, pp. 1238–1243, 2001.

[42] C. J. Mummery, K. Patterson, C. J. Price, J. Ashburner, R. S. J. Frackowiak, and J. R. Hodges, "A voxel-based morphometry study of semantic dementia: relationship between temporal lobe atrophy and semantic memory," *Annals of Neurology*, vol. 47, no. 1, pp. 36–45, 2000.

[43] C. Davatzikos, A. Genc, D. Xu, and S. M. Resnick, "Voxel-based morphometry using the RAVENS maps: methods and validation using simulated longitudinal atrophy," *NeuroImage*, vol. 14, no. 6, pp. 1361–1369, 2001.

[44] C. D. Good, I. Johnsrude, J. Ashburner, R. N. Henson, K. J. Friston, and R. S. Frackowiak, "Cerebral asymmetry and the effects of sex and handedness on brain structure: a voxel-based morphometric analysis of 465 normal adult human brains," *NeuroImage*, vol. 14, no. 3, pp. 685–700, 2001.

[45] C. D. Good, R. I. Scahill, N. C. Fox, J. Ashburner, K. J. Friston, D. Chan, W. R. Crum, M. N. Rossor, and R. S. Frackowiak, "Automatic differentiation of anatomical patterns in the human brain: validation with studies of degenerative dementias," *NeuroImage*, vol. 17, no. 1, pp. 29–46, 2002.

[46] G. F. Busatto, G. E. Garrido, O. P. Almeida, C. C. Castro, C. H. Camargo, C. G. Cid, C. A. Buchpiguel, S. Furuie, and C. M. Bottino, "A voxel-based morphometry study of temporal lobe gray matter reductions in alzheimer's disease," *Neurobiology of Aging*, vol. 24, no. 2, pp. 221–231, 2003.

[47] G. Karas, P. Scheltens, S. Rombouts, P. Visser, R. Van Schijndel, N. Fox, and F. Barkhof, "Global and local gray matter loss in mild cognitive impairment and Alzheimer's disease," *NeuroImage*, vol. 23, no. 2, pp. 708–716, 2004.

[48] G. M. McAlonan, V. Cheung, C. Cheung, J. Suckling, G. Y. Lam, K. Tai, L. Yip, D. G. Murphy, and S. E. Chua, "Mapping the brain in autism. A voxel-based MRI study of volumetric differences and intercorrelations in autism," *Brain*, vol. 128, no. 2, pp. 268–276, 2005.

[49] A. Mechelli, C. J. Price, K. J. Friston, and J. Ashburner, "Voxel-based morphometry of the human brain: methods and applications," *Current Medical Imaging Reviews*, vol. 1, no. 2, pp. 105–113, 2005.

[50] R. Honea, T. J. Crow, D. Passingham, and C. E. Mackay, "Regional deficits in brain volume in schizophrenia: a meta-analysis of voxel-based morphometry studies," *American Journal of Psychiatry*, 2014.

[51] C. Davatzikos, M. Vaillant, S. M. Resnick, J. L. Prince, S. Letovsky, and R. N. Bryan, "A computerized approach for morphological analysis of the corpus callosum," *Journal of Computer Assisted Tomography*, vol. 20, no. 1, pp. 88–97, 1996.

[52] M. Miller, A. Banerjee, G. Christensen, S. Joshi, N. Khaneja, U. Grenander, and L. Matejic, "Statistical methods in computational anatomy," *Statistical Methods in Medical Research*, vol. 6, no. 3, pp. 267–299, 1997.

[53] C. Davatzikos, "Why voxel-based morphometric analysis should be used with great caution when characterizing group differences," *NeuroImage*, vol. 23, no. 1, pp. 17–20, 2004.

[54] Z. Lao, D. Shen, Z. Xue, B. Karacali, S. M. Resnick, and C. Davatzikos, "Morphological classification of brains via high-dimensional shape transformations and machine learning methods," *NeuroImage*, vol. 21, no. 1, pp. 46–57, 2004.

[55] Y. Fan, D. Shen, R. C. Gur, R. E. Gur, and C. Davatzikos, "COMPARE: classification of morphological patterns using adaptive regional elements," *IEEE Transactions on Medical Imaging*, vol. 26, no. 1, pp. 93–105, 2007.

[56] Y. Fan, N. Batmanghelich, C. M. Clark, C. Davatzikos, and A. D. N. Initiative, "Spatial patterns of brain atrophy in MCI patients, identified via high-dimensional pattern classification, predict subsequent cognitive decline," *NeuroImage*, vol. 39, no. 4, pp. 1731–1743, 2008.

[57] Y. Fan, S. M. Resnick, X. Wu, and C. Davatzikos, "Structural and functional biomarkers of prodromal Alzheimer's disease: a high-dimensional pattern classification study," *NeuroImage*, vol. 41, no. 2, pp. 277–285, 2008.

[58] C. Davatzikos, Y. Fan, X. Wu, D. Shen, and S. M. Resnick, "Detection of prodromal Alzheimer's disease via pattern classification of magnetic resonance imaging," *Neurobiology of Aging*, vol. 29, no. 4, pp. 514–523, 2008.

[59] C. Davatzikos, S. M. Resnick, X. Wu, P. Parmpi, and C. M. Clark, "Individual patient diagnosis of AD and FTD via high-dimensional pattern classification of MRI," *NeuroImage*, vol. 41, no. 4, pp. 1220–1227, 2008.

[60] P. Vemuri, J. L. Gunter, M. L. Senjem, J. L. Whitwell, K. Kantarci, D. S. Knopman, B. F. Boeve, R. C. Petersen, and C. R. Jack, "Alzheimer's disease diagnosis in individual subjects using structural MR images: validation studies," *NeuroImage*, vol. 39, no. 3, pp. 1186–1197, 2008.

[61] C. Misra, Y. Fan, and C. Davatzikos, "Baseline and longitudinal patterns of brain atrophy in MCI patients, and their use in prediction of short-term conversion to AD: results from ADNI," *NeuroImage*, vol. 44, no. 4, pp. 1415–1422, 2009.

[62] N. K. Batmanghelich, B. Taskar, and C. Davatzikos, "Generative-discriminative basis learning for medical imaging," *IEEE Transactions on Medical Imaging*, vol. 31, no. 1, pp. 51–69, 2012.

[63] S. Wold, K. Esbensen, and P. Geladi, "Principal Component Analysis," *Chemometrics and Intelligent Laboratory Systems*, vol. 2, no. 1, pp. 37–52, 1987.

[64] I. Jolliffe, *Principal component analysis*. Wiley Online Library, 2002.

[65] H. Abdi and L. J. Williams, "Principal component analysis," *Wiley Interdisciplinary Reviews: Computational Statistics*, vol. 2, no. 4, pp. 433–459, 2010.

[66] J. W. Sammon, "A nonlinear mapping for data structure analysis," *IEEE Transactions on Computers*, no. 5, pp. 401–409, 1969.

[67] M. A. Kramer, "Nonlinear principal component analysis using autoassociative neural networks," *AIChE Journal*, vol. 37, no. 2, pp. 233–243, 1991.

[68] S. T. Roweis and L. K. Saul, "Nonlinear dimensionality reduction by locally linear embedding," *Science*, vol. 290, no. 5500, pp. 2323–2326, 2000.

[69] L. K. Saul and S. T. Roweis, "Think globally, fit locally: unsupervised learning of low dimensional manifolds," *The Journal of Machine Learning Research*, vol. 4, pp. 119–155, 2003.

[70] Z.-y. Zhang and H.-y. Zha, "Principal manifolds and nonlinear dimensionality reduction via tangent space alignment," *Journal of Shanghai University (English Edition)*, vol. 8, no. 4, pp. 406–424, 2004.

[71] R. A. Fisher, "The use of multiple measurements in taxonomic problems," *Annals of Eugenics*, vol. 7, no. 2, pp. 179–188, 1936.

[72] D. W. Hosmer Jr and S. Lemeshow, *Applied Logistic Regression*. John Wiley & Sons, 2004.

[73] D. A. Freedman, *Statistical Models: Theory and Practice*. Cambridge, UK: Cambridge University Press, 2009.

[74] C. Cortes and V. Vapnik, "Support-vector networks," *Machine Learning*, vol. 20, no. 3, pp. 273–297, 1995.

[75] J. R. Quinlan, "Induction of decision trees," *Machine Learning*, vol. 1, no. 1, pp. 81–106, 1986.

[76] J. R. Quinlan, "Simplifying decision trees," *International Journal of Man-machine Studies*, vol. 27, no. 3, pp. 221–234, 1987.

[77] D. Opitz and R. Maclin, "Popular ensemble methods: An empirical study," *Journal of Artificial Intelligence Research*, pp. 169–198, 1999.

[78] R. Polikar, "Ensemble based systems in decision making," *Circuits and Systems Magazine, IEEE*, vol. 6, no. 3, pp. 21–45, 2006.

[79] F. L. Bookstein, "Shape and the information in medical images: A decade of the morphometric synthesis," in *Mathematical Methods in Biomedical Image Analysis, 1996., Proceedings of the Workshop on*, pp. 2–12, IEEE, 1996.

[80] F. L. Bookstein, "Landmark methods for forms without landmarks: morphometrics of group differences in outline shape," *Medical Image Analysis*, vol. 1, no. 3, pp. 225–243, 1997.

[81] F. L. Bookstein, *Morphometric tools for landmark data: geometry and biology*. Cambridge University Press, 1997.

[82] T. F. Cootes and C. J. Taylor, "A mixture model for representing shape variation," *Image and Vision Computing*, vol. 17, no. 8, pp. 567–573, 1999.

[83] X. Tao, X. Han, M. E. Rettmann, J. L. Prince, and C. Davatzikos, "Statistical study on cortical sulci of human brains," in *Information Processing in Medical Imaging*, pp. 475–487, Springer, 2001.

[84] X. Tao, J. L. Prince, and C. Davatzikos, "Using a statistical shape model to extract sulcal curves on the outer cortex of the human brain," *IEEE Transactions on Medical Imaging*, vol. 21, no. 5, pp. 513–524, 2002.

[85] D. Shen, E. H. Herskovits, and C. Davatzikos, "An adaptive-focus statistical shape model for segmentation and shape modeling of 3-D brain structures," *IEEE Transactions on Medical Imaging*, vol. 20, no. 4, pp. 257–270, 2001.

[86] G. Gerig, M. Styner, D. Jones, D. Weinberger, and J. Lieberman, "Shape analysis of brain ventricles using spharm," in *Mathematical Methods in Biomedical Image Analysis, 2001. MMBIA 2001. IEEE Workshop on*, pp. 171–178, IEEE, 2001.

[87] G. Gerig, M. Styner, M. E. Shenton, and J. A. Lieberman, "Shape versus size: Improved understanding of the morphology of brain structures," in *Medical Image Computing and Computer-Assisted Intervention–MICCAI 2001*, pp. 24–32, Springer, 2001.

[88] R. H. Davies, C. J. Twining, T. F. Cootes, J. C. Waterton, and C. J. Taylor, "3D statistical shape models using direct optimisation of description length," in *ECCV 2002*, pp. 3–20, Springer, 2002.

[89] M. Styner, G. Gerig, J. Lieberman, D. Jones, and D. Weinberger, "Statistical shape analysis of neuroanatomical structures based on medial models," *Medical Image Analysis*, vol. 7, no. 3, pp. 207–220, 2003.

[90] M. Styner, J. A. Lieberman, D. Pantazis, and G. Gerig, "Boundary and medial shape analysis of the hippocampus in schizophrenia," *Medical Image Analysis*, vol. 8, no. 3, pp. 197–203, 2004.

[91] M. Styner, I. Oguz, S. Xu, C. Brechbühler, D. Pantazis, J. J. Levitt, M. E. Shenton, and G. Gerig, "Framework for the statistical shape analysis of brain structures using SPHARM-PDM," *The Insight Journal*, no. 1071, p. 242, 2006.

[92] J. Ma, M. I. Miller, A. Trouvé, and L. Younes, "Bayesian template estimation in computational anatomy," *NeuroImage*, vol. 42, no. 1, pp. 252–261, 2008.

[93] A. Qiu, C. Fennema-Notestine, A. M. Dale, M. I. Miller, and A. D. N. Initiative, "Regional shape abnormalities in mild cognitive impairment and Alzheimer's disease," *NeuroImage*, vol. 45, no. 3, pp. 656–661, 2009.

[94] L. Younes, J. T. Ratnanather, T. Brown, E. Aylward, P. Nopoulos, H. Johnson, V. A. Magnotta, J. S. Paulsen, R. L. Margolis, R. L. Albin, M. L. Miller, C. A. Ross, and PREDICT-HD Investigators and Coordinators of the Huntington

Study Group, "Regionally selective atrophy of subcortical structures in prodromal HD as revealed by statistical shape analysis," *Human Brain Mapping*, vol. 35, no. 3, pp. 792–809, 2014.

[95] B. Patenaude, S. M. Smith, D. N. Kennedy, and M. Jenkinson, "A bayesian model of shape and appearance for subcortical brain segmentation," *NeuroImage*, vol. 56, no. 3, pp. 907–922, 2011.

[96] I. L. Dryden and K. V. Mardia, *Statistical Shape Analysis*, vol. 4. Wiley Chichester, 1998.

[97] K. Bürk, M. Abele, M. Fetter, J. Dichgans, M. Skalej, F. Laccone, O. Didierjean, A. Brice, and T. Klockgether, "Autosomal dominant cerebellar ataxia type I clinical features and MRI in families with SCA1, SCA2 and SCA3," *Brain*, vol. 119, no. 5, pp. 1497–1505, 1996.

[98] T. H. Wassink, N. C. Andreasen, P. Nopoulos, and M. Flaum, "Cerebellar morphology as a predictor of symptom and psychosocial outcome in schizophrenia," *Biological Psychiatry*, vol. 45, no. 1, pp. 41–48, 1999.

[99] E. V. Sullivan, A. Deshmukh, J. E. Desmond, K. O. Lim, and A. Pfefferbaum, "Cerebellar volume decline in normal aging, alcoholism, and Korsakoff's syndrome: relation to ataxia.," *Neuropsychology*, vol. 14, no. 3, p. 341, 2000.

[100] F. Tavani, R. Zimmerman, G. Berry, K. Sullivan, R. Gatti, and P. Bingham, "Ataxia-telangiectasia: the pattern of cerebellar atrophy on MRI," *Neuroradiology*, vol. 45, no. 5, pp. 315–319, 2003.

[101] S. Ying, S. Choi, S. Perlman, R. Baloh, D. Zee, and A. Toga, "Pontine and cerebellar atrophy correlate with clinical disability in SCA2," *Neurology*, vol. 66, no. 3, pp. 424–426, 2006.

[102] H. Tiemeier, R. K. Lenroot, D. K. Greenstein, L. Tran, R. Pierson, and J. N. Giedd, "Cerebellum development during childhood and adolescence: a longitudinal morphometric MRI study," *NeuroImage*, vol. 49, no. 1, pp. 63–70, 2010.

[103] B. C. Jung, S. I. Choi, A. X. Du, J. L. Cuzzocreo, H. S. Ying, B. A. Landman, S. L. Perlman, R. W. Baloh, D. S. Zee, A. W. Toga, J. L. Prince, and S. H. Ying, "MRI shows a region-specific pattern of atrophy in spinocerebellar ataxia type 2," *The Cerebellum*, vol. 11, no. 1, pp. 272–279, 2012.

[104] B. C. Jung, S. I. Choi, A. X. Du, J. L. Cuzzocreo, Z. Z. Geng, H. S. Ying, S. L. Perlman, A. W. Toga, J. L. Prince, and S. H. Ying, "Principal component analysis of cerebellar shape on MRI separates SCA types 2 and 6 into two archetypal modes of degeneration," *The Cerebellum*, vol. 11, no. 4, pp. 887–895, 2012.

[105] C. Lukas, L. Schöls, B. Bellenberg, U. Rüb, H. Przuntek, G. Schmid, O. Köster, and B. Suchan, "Dissociation of grey and white matter reduction in spinocerebellar ataxia type 3 and 6: a voxel-based morphometry study," *Neuroscience Letters*, vol. 408, no. 3, pp. 230–235, 2006.

[106] S. G. Mueller, K. D. Laxer, N. Cashdollar, S. Buckley, C. Paul, and M. W. Weiner, "Voxel-based Optimized Morphometry (VBM) of Gray and White Matter in Temporal Lobe Epilepsy (TLE) with and without Mesial Temporal Sclerosis," *Epilepsia*, vol. 47, no. 5, pp. 900–907, 2006.

[107] M. E. Sim, I. K. Lyoo, C. C. Streeter, J. Covell, O. Sarid-Segal, D. A. Ciraulo, M. J. Kim, M. J. Kaufman, D. A. Yurgelun-Todd, and P. F. Renshaw, "Cerebellar gray matter volume correlates with duration of cocaine use in cocaine-dependent subjects," *Neuropsychopharmacology*, vol. 32, no. 10, pp. 2229–2237, 2007.

[108] J. B. Schulz, J. Borkert, S. Wolf, T. Schmitz-Hübsch, M. Rakowicz, C. Mariotti, L. Schoels, D. Timmann, B. van de Warrenburg, A. Dürr, *et al.*, "Visualization, quantification and correlation of brain atrophy with clinical symptoms in spinocerebellar ataxia types 1, 3 and 6," *NeuroImage*, vol. 49, no. 1, pp. 158–168, 2010.

[109] J. Peng, J. Liu, B. Nie, Y. Li, B. Shan, G. Wang, and K. Li, "Cerebral and cerebellar gray matter reduction in first-episode patients with major depressive disorder: a voxel-based morphometry study," *European Journal of Radiology*, vol. 80, no. 2, pp. 395–399, 2011.

[110] Z. Yang, J. A. Bogovic, C. Ye, A. Carass, S. H. Ying, and J. L. Prince, "Automated cerebellar lobule segmentation using graph cuts," *MICCAI Challenge Workshop on Segmentation: Algorithms, Theory and Applications*, 2013.

[111] Z. Yang, C. Ye, J. A. Bogovic, A. Carass, B. M. Jedynake, S. H. Ying, and J. L. Prince, "Automated cerebellar lobule segmentation with application to cerebellar structural analysis in cerebellar disease," *NeuroImage*. accepted.

[112] Z. Yang, S. M. Abulnaga, A. Carass, K. Kansal, B. M. Jedynak, C. Onyike, S. H. Ying, and J. L. Prince, "Landmark based shape analysis for cerebellar ataxia classification and cerebellar atrophy pattern visualization," *SPIE Medical Imaging*, 2016. submitted.

[113] K. Bhattacharya, D. Saadia, B. Eisenkraft, M. Yahr, W. Olanow, B. Drayer, and H. Kaufmann, "Brain magnetic resonance imaging in multiple-system atrophy and Parkinson disease: a diagnostic algorithm," *Archives of Neurology*, vol. 59, no. 5, pp. 835–842, 2002.

[114] T. Wu and M. Hallett, "Reply: The cerebellum in parkinsonâĂŹs disease and parkinsonism in cerebellar disorders," *Brain*, vol. 136, no. 9, pp. e249–e249, 2013.

[115] R. Rodda, "Cerebellar atrophy in Huntington's disease," *Journal of the Neurological Sciences*, vol. 50, no. 1, pp. 147–157, 1981.

[116] U. Rüb, F. Hoche, E. R. Brunt, H. Heinsen, K. Seidel, D. Del Turco, H. L. Paulson, J. Bohl, C. Gall, J.-P. Vonsattel, H.-W. Korf, and W. F. den Dunnen, "Degeneration of the cerebellum in Huntington's disease (HD): possible relevance for the clinical picture and potential gateway to pathological mechanisms of the disease process," *Brain Pathology*, vol. 23, no. 2, pp. 165–177, 2013.

[117] M. Sjöbeck and E. Englund, "Alzheimer's disease and the cerebellum: a morphologic study on neuronal and glial changes," *Dementia and Geriatric Cognitive Disorders*, vol. 12, no. 3, pp. 211–218, 2001.

[118] A. Kutzelnigg, J. C. Faber-Rod, J. Bauer, C. F. Lucchinetti, P. S. Sorensen, H. Laursen, C. Stadelmann, W. Brück, H. Rauschka, M. Schmidbauer, and H. Lassmann, "Widespread demyelination in the cerebellar cortex in multiple sclerosis," *Brain Pathology*, vol. 17, no. 1, pp. 38–44, 2007.

[119] J. L. Lancaster, M. G. Woldorff, L. M. Parsons, M. Liotti, C. S. Freitas, L. Rainey, P. V. Kochunov, D. Nickerson, S. A. Mikiten, and P. T. Fox, "Automated Talairach atlas labels for functional brain mapping," *Human Brain Mapping*, vol. 10, no. 3, pp. 120–131, 2000.

[120] J. A. Bogovic, B. Jedynak, R. Rigg, A. Du, B. A. Landman, J. L. Prince, and S. H. Ying, "Approaching expert results using a hierarchical cerebellum parcellation protocol for multiple inexpert human raters," *NeuroImage*, vol. 64, no. 1, pp. 616–629, 2013.

[121] B. Fischl, D. H. Salat, E. Busa, M. Albert, M. Dieterich, C. Haselgrove, A. Van Der Kouwe, R. Killiany, D. Kennedy, S. Klaveness, A. Montillo, N. Makris, B. Rosen, and A. M. Dale, "Whole brain segmentation: automated labeling of neuroanatomical structures in the human brain," *Neuron*, vol. 33, no. 3, pp. 341–355, 2002.

[122] N. Shiee, P.-L. Bazin, A. Ozturk, D. S. Reich, P. A. Calabresi, and D. L. Pham, "A topology-preserving approach to the segmentation of brain images with multiple sclerosis lesions," *NeuroImage*, vol. 49, no. 2, pp. 1524–1535, 2010.

[123] C. Ciofolo and C. Barillot, "Atlas-based segmentation of 3D cerebral structures with competitive level sets and fuzzy control.," *Medical Image Analysis*, vol. 13, no. 3, p. 456, 2009.

[124] F. van der Lijn, M. de Bruijne, Y. Y. Hoogendam, S. Klein, R. Hameeteman, M. M. Breteler, and W. J. Niessen, "Cerebellum segmentation in MRI using atlas registration and local multi-scale image descriptors," in *Biomedical Imaging: From Nano to Macro, 2009. ISBI'09. IEEE International Symposium on*, pp. 221–224, IEEE, 2009.

[125] J. Hwang, J. Kim, Y. Han, and H. Park, "An automatic cerebellum extraction method in T1-weighted brain MR images using an active contour model with a shape prior," *Magnetic Resonance Imaging*, vol. 29, no. 7, pp. 1014–1022, 2011.

[126] J. Diedrichsen, "A spatially unbiased atlas template of the human cerebellum," *NeuroImage*, vol. 33, no. 1, pp. 127–138, 2006.

[127] J. Diedrichsen, J. H. Balsters, J. Flavell, E. Cussans, and N. Ramnani, "A probabilistic MR atlas of the human cerebellum," *NeuroImage*, vol. 46, no. 1, pp. 39–46, 2009.

[128] S. K. Warfield, K. H. Zou, and W. M. Wells, "Simultaneous truth and performance level estimation (STAPLE): an algorithm for the validation of image segmentation," *IEEE Transactions on Medical Imaging*, vol. 23, no. 7, pp. 903–921, 2004.

[129] R. A. Heckemann, J. V. Hajnal, P. Aljabar, D. Rueckert, and A. Hammers, "Automatic anatomical brain MRI segmentation combining label propagation and decision fusion," *NeuroImage*, vol. 33, no. 1, pp. 115–126, 2006.

[130] X. Artaechevarria, A. Munoz-Barrutia, and C. Ortiz-de Solórzano, "Combination strategies in multi-atlas image segmentation: Application to brain MR data," *IEEE Transactions on Medical Imaging*, vol. 28, no. 8, pp. 1266–1277, 2009.

[131] P. Aljabar, R. A. Heckemann, A. Hammers, J. V. Hajnal, and D. Rueckert, "Multi-atlas based segmentation of brain images: atlas selection and its effect on accuracy," *NeuroImage*, vol. 46, no. 3, pp. 726–738, 2009.

[132] A. J. Asman and B. Landman, "Formulating spatially varying performance in the statistical fusion framework," *IEEE Transactions on Medical Imaging*, vol. 31, no. 6, pp. 1326–1336, 2012.

[133] A. J. Asman and B. A. Landman, "Non-local statistical label fusion for multi-atlas segmentation," *Medical Image Analysis*, vol. 17, no. 2, pp. 194–208, 2013.

[134] X. Tang, K. Oishi, A. V. Faria, A. E. Hillis, M. S. Albert, S. Mori, and M. I. Miller, "Bayesian parameter estimation and segmentation in the multi-atlas random orbit model," *PloS ONE*, vol. 8, no. 6, p. e65591, 2013.

[135] K. Weier, V. Fonov, K. Lavoie, J. Doyon, and D. L. Collins, "Rapid automatic segmentation of the human cerebellum and its lobules (rascal)âĂŤimplementation and application of the patch-based label-fusion technique with a template library to segment the human cerebellum," *Human brain mapping*, vol. 35, no. 10, pp. 5026–5039, 2014.

[136] J. A. Bogovic, P.-L. Bazin, S. H. Ying, and J. L. Prince, "Automated segmentation of the cerebellar lobules using boundary specific classification and

evolution," in *Information Processing in Medical Imaging* (J. C. Gee, S. Joshi, K. M. Pohl, W. M. Wells, and L. Zöllei, eds.), vol. 7917 of *Lecture Notes in Computer Science*, pp. 62–73, Springer, 2013.

[137] A. C. Evans, S. Marrett, P. Neelin, L. Collins, K. Worsley, W. Dai, S. Milot, E. Meyer, and D. Bub, "Anatomical mapping of functional activation in stereotactic coordinate space," *NeuroImage*, vol. 1, no. 1, pp. 43–53, 1992.

[138] A. C. Evans, D. L. Collins, S. Mills, E. Brown, R. Kelly, and T. M. Peters, "3D statistical neuroanatomical models from 305 MRI volumes," in *Nuclear Science Symposium and Medical Imaging Conference, 1993., 1993 IEEE Conference Record.*, pp. 1813–1817, IEEE, 1993.

[139] Y. Boykov, O. Veksler, and R. Zabih, "Fast approximate energy minimization via graph cuts," *IEEE Transactions on Pattern Analysis and Machine Intelligence*, vol. 23, no. 11, pp. 1222–1239, 2001.

[140] Y. Boykov and G. Funka-Lea, "Graph cuts and efficient ND image segmentation," *International Journal of Computer Vision*, vol. 70, no. 2, pp. 109–131, 2006.

[141] T. Rohlfing, R. Brandt, C. R. Maurer Jr, and R. Menzel, "Bee brains, B-splines and computational democracy: Generating an average shape atlas," in *Mathematical Methods in Biomedical Image Analysis, 2001. MMBIA 2001. IEEE Workshop on*, pp. 187–194, IEEE, 2001.

[142] I. Isgum, M. Staring, A. Rutten, M. Prokop, M. A. Viergever, and B. van Ginneken, "Multi-atlas-based segmentation with local decision fusion—Application to cardiac and aortic segmentation in CT scans," *IEEE Transactions on Medical Imaging*, vol. 28, no. 7, pp. 1000–1010, 2009.

[143] P. Coupé, J. V. Manjón, V. Fonov, J. Pruessner, M. Robles, and D. L. Collins, "Patch-based segmentation using expert priors: Application to hippocampus and ventricle segmentation," *NeuroImage*, vol. 54, no. 2, pp. 940–954, 2011.

[144] A. J. Asman and B. A. Landman, "Robust statistical label fusion through consensus level, labeler accuracy, and truth estimation (COLLATE)," *IEEE Transactions on Medical Imaging*, vol. 30, no. 10, pp. 1779–1794, 2011.

[145] B. A. Landman, A. J. Asman, A. G. Scoggins, J. A. Bogovic, F. Xing, and J. L. Prince, "Robust statistical fusion of image labels," *IEEE Transactions on Medical Imaging*, vol. 31, no. 2, pp. 512–522, 2012.

[146] A. Buades, B. Coll, and J.-M. Morel, "A non-local algorithm for image denoising," in *Computer Vision and Pattern Recognition, 2005. CVPR 2005. IEEE Computer Society Conference on*, vol. 2, pp. 60–65, IEEE, 2005.

[147] B. B. Avants, C. L. Epstein, M. Grossman, and J. C. Gee, "Symmetric diffeomorphic image registration with cross-correlation: evaluating automated labeling of elderly and neurodegenerative brain," *Medical Image Analysis*, vol. 12, no. 1, pp. 26–41, 2008.

[148] B. B. Avants, N. J. Tustison, G. Song, P. A. Cook, A. Klein, and J. C. Gee, "A reproducible evaluation of ants similarity metric performance in brain image registration," *NeuroImage*, vol. 54, no. 3, pp. 2033–2044, 2011.

[149] L. Breiman, "Random forests," *Machine Learning*, vol. 45, no. 1, pp. 5–32, 2001.

[150] D. Marr and H. K. Nishihara, "Representation and recognition of the spatial organization of three-dimensional shapes," *Proceedings of the Royal Society of London B: Biological Sciences*, vol. 200, no. 1140, pp. 269–294, 1978.

[151] S. Belongie, J. Malik, and J. Puzicha, "Shape matching and object recognition using shape contexts," *IEEE Transactions on Pattern Analysis and Machine Intelligence*, vol. 24, no. 4, pp. 509–522, 2002.

[152] B. Leibe, A. Leonardis, and B. Schiele, "Combined object categorization and segmentation with an implicit shape model," in *Workshop on Statistical Learning in Computer Vision, ECCV*, vol. 2, p. 7, 2004.

[153] T. Heimann and H.-P. Meinzer, "Statistical shape models for 3D medical image segmentation: a review," *Medical Image Analysis*, vol. 13, no. 4, pp. 543–563, 2009.

[154] D. G. Kendall, "Shape manifolds, procrustean metrics, and complex projective spaces," *Bulletin of the London Mathematical Society*, vol. 16, no. 2, pp. 81–121, 1984.

[155] J. Csernansky, L. Wang, J. Swank, J. Miller, M. Gado, D. McKeel, M. Miller, and J. Morris, "Preclinical detection of Alzheimer's disease: hippocampal shape and volume predict dementia onset in the elderly," *NeuroImage*, vol. 25, no. 3, pp. 783–792, 2005.

[156] D. G. Kendall, "A survey of the statistical theory of shape," *Statistical Science*, pp. 87–99, 1989.

[157] F. L. Bookstein, "Size and shape spaces for landmark data in two dimensions," *Statistical Science*, pp. 181–222, 1986.

[158] C. Goodall, "Procrustes methods in the statistical analysis of shape," *Journal of the Royal Statistical Society. Series B (Methodological)*, pp. 285–339, 1991.

[159] I. Dryden and K. V. Mardia, "General shape distributions in a plane," *Advances in Applied Probability*, pp. 259–276, 1991.

[160] C. R. Goodall and K. V. Mardia, "Multivariate aspects of shape theory," *The Annals of Statistics*, pp. 848–866, 1993.

[161] I. Dryden and K. Mardia, "Multivariate shape analysis," *Sankhyā: The Indian Journal of Statistics, Series A*, pp. 460–480, 1993.

[162] T. F. Cootes and C. J. Taylor, "Active shape models—'smart snakes'," in *BMVC92*, pp. 266–275, Springer, 1992.

[163] T. F. Cootes, C. J. Taylor, D. H. Cooper, and J. Graham, "Active shape models-their training and application," *Computer Vision and Image Understanding*, vol. 61, no. 1, pp. 38–59, 1995.

[164] H. Blum, "Biological shape and visual science (Part I)," *Journal of Theoretical Biology*, vol. 38, no. 2, pp. 205–287, 1973.

[165] S. M. Pizer, D. S. Fritsch, P. Yushkevich, V. E. Johnson, and E. L. Chaney, "Segmentation, registration, and measurement of shape variation via image object shape," *IEEE Transactions on Medical Imaging*, vol. 18, no. 10, pp. 851–865, 1999.

[166] S. M. Pizer, P. T. Fletcher, S. Joshi, A. Thall, J. Z. Chen, Y. Fridman, D. S. Fritsch, A. G. Gash, J. M. Glotzer, M. R. Jiroutek, C. Lu, K. E. Muller, G. Tracton, P. Yushkevich, and E. L. Chaney, "Deformable M-Reps for 3D medical image segmentation," *International Journal of Computer Vision*, vol. 55, no. 2-3, pp. 85–106, 2003.

[167] M. Styner and G. Gerig, "Hybrid boundary-medial shape description for biologically variable shapes," in *Mathematical Methods in Biomedical Image Analysis, 2000. Proceedings. IEEE Workshop on*, pp. 235–242, IEEE, 2000.

[168] M. Styner and G. Gerig, "Medial models incorporating object variability for 3D shape analysis," in *Information Processing in Medical Imaging*, pp. 502–516, Springer, 2001.

[169] M. Styner, G. Gerig, S. Joshi, and S. Pizer, "Automatic and robust computation of 3D medial models incorporating object variability," *International Journal of Computer Vision*, vol. 55, no. 2-3, pp. 107–122, 2003.

[170] P. T. Fletcher, C. Lu, S. M. Pizer, and S. Joshi, "Principal geodesic analysis for the study of nonlinear statistics of shape," *IEEE Transactions on Medical Imaging*, vol. 23, no. 8, pp. 995–1005, 2004.

[171] L. H. Staib and J. S. Duncan, "Model-based deformable surface finding for medical images," *IEEE Transactions on Medical Imaging*, vol. 15, no. 5, pp. 720–731, 1996.

[172] G. Székely, A. Kelemen, C. Brechbühler, and G. Gerig, "Segmentation of 2-D and 3-D objects from MRI volume data using constrained elastic deformations of flexible Fourier contour and surface models," *Medical Image Analysis*, vol. 1, no. 1, pp. 19–34, 1996.

[173] A. Kelemen, G. Székely, and G. Gerig, "Elastic model-based segmentation of 3-D neuroradiological data sets," *IEEE Transactions on Medical Imaging*, vol. 18, no. 10, pp. 828–839, 1999.

[174] A. Matheny and D. B. Goldgof, "The use of three-and four-dimensional surface harmonics for rigid and nonrigid shape recovery and representation," *IEEE Transactions on Pattern Analysis and Machine Intelligence*, vol. 17, no. 10, pp. 967–981, 1995.

[175] C. Nikou, G. Bueno, F. Heitz, and J.-P. Armspach, "A joint physics-based statistical deformable model for multimodal brain image analysis," *IEEE Transactions on Medical Imaging*, vol. 20, no. 10, pp. 1026–1037, 2001.

[176] C. Davatzikos, X. Tao, and D. Shen, "Hierarchical active shape models, using the wavelet transform," *IEEE Transactions on Medical Imaging*, vol. 22, no. 3, pp. 414–423, 2003.

[177] D. Nain, S. Haker, A. Bobick, and A. Tannenbaum, "Multiscale 3-D shape representation and segmentation using spherical wavelets," *IEEE Transactions on Medical Imaging*, vol. 26, no. 4, pp. 598–618, 2007.

[178] P. Yu, P. E. Grant, Y. Qi, X. Han, F. Ségonne, R. Pienaar, E. Busa, J. Pacheco, N. Makris, R. L. Buckner, P. Golland, and F. Bruce, "Cortical surface shape analysis based on spherical wavelets," *IEEE Transactions on Medical Imaging*, vol. 26, no. 4, pp. 582–597, 2007.

[179] B. Tsagaan, A. Shimizu, H. Kobatake, and K. Miyakawa, "An automated segmentation method of kidney using statistical information," in *Medical Image Computing and Computer-Assisted InterventionâĂŤMICCAI 2002*, pp. 556–563, Springer, 2002.

[180] J. A. Sethian, *Level set methods and fast marching methods: evolving interfaces in computational geometry, fluid mechanics, computer vision, and materials science*, vol. 3. Cambridge university press, 1999.

[181] S. Osher and J. A. Sethian, "Fronts propagating with curvature-dependent speed: algorithms based on Hamilton-Jacobi formulations," *Journal of Computational Physics*, vol. 79, no. 1, pp. 12–49, 1988.

[182] R. Malladi, J. Sethian, and B. C. Vemuri, "Shape modeling with front propagation: A level set approach," *IEEE Transactions on Medical Imaging*, vol. 17, no. 2, pp. 158–175, 1995.

[183] T. F. Chan and L. Vese, "Active contours without edges," *IEEE Transactions on Image Processing*, vol. 10, no. 2, pp. 266–277, 2001.

[184] Y. Chen, H. D. Tagare, S. Thiruvenkadam, F. Huang, D. Wilson, K. S. Gopinath, R. W. Briggs, and E. A. Geiser, "Using prior shapes in geometric active contours in a variational framework," *International Journal of Computer Vision*, vol. 50, no. 3, pp. 315–328, 2002.

[185] D. Cremers, M. Rousson, and R. Deriche, "A review of statistical approaches to level set segmentation: integrating color, texture, motion and shape," *International Journal of Computer Vision*, vol. 72, no. 2, pp. 195–215, 2007.

[186] J. C. Gower, "Generalized procrustes analysis," *Psychometrika*, vol. 40, no. 1, pp. 33–51, 1975.

[187] B. K. Horn, "Closed-form solution of absolute orientation using unit quaternions," *Journal of the Optical Society of America A*, vol. 4, no. 4, pp. 629–642, 1987.

[188] A. F. Frangi, D. Rueckert, J. Schnabel, and W. J. Niessen, "Automatic construction of multiple-object three-dimensional statistical shape models: Application to cardiac modeling," *IEEE Transactions on Medical Imaging*, vol. 21, no. 9, pp. 1151–1166, 2002.

[189] W. E. Lorensen and H. E. Cline, "Marching cubes: A high resolution 3D surface construction algorithm," *ACM Siggraph Computer Graphics*, vol. 21, no. 4, pp. 163–169, 1987.

[190] A. Myronenko and X. Song, "Point set registration: Coherent point drift," *IEEE Transactions on Pattern Analysis and Machine Intelligence*, vol. 32, no. 12, pp. 2262–2275, 2010.

[191] D. W. Shattuck and R. M. Leahy, "BrainSuite: an automated cortical surface identification tool," *Medical Image Analysis*, vol. 6, no. 2, pp. 129–142, 2002.

[192] D. C. Van Essen, H. A. Drury, J. Dickson, J. Harwell, D. Hanlon, and C. H. Anderson, "An integrated software suite for surface-based analyses of cerebral cortex," *Journal of the American Medical Informatics Association*, vol. 8, no. 5, pp. 443–459, 2001.

[193] D. C. Van Essen, "Windows on the brain: the emerging role of atlases and databases in neuroscience," *Current Opinion in Neurobiology*, vol. 12, no. 5, pp. 574–579, 2002.

[194] D. R. Cox, "The regression analysis of binary sequences," *Journal of the Royal Statistical Society. Series B (Methodological)*, pp. 215–242, 1958.

[195] S. H. Walker and D. B. Duncan, "Estimation of the probability of an event as a function of several independent variables," *Biometrika*, vol. 54, no. 1-2, pp. 167–179, 1967.

[196] S. Russell and P. Norvig, "Artificial intelligence: a modern approach," 1995.

[197] Y. Freund and R. E. Schapire, "Large margin classification using the perceptron algorithm," *Machine Learning*, vol. 37, no. 3, pp. 277–296, 1999.

[198] G.-X. Yuan, C.-H. Ho, and C.-J. Lin, "Recent advances of large-scale linear classification," *Proceedings of the IEEE*, vol. 100, no. 9, pp. 2584–2603, 2012.

[199] B. E. Boser, I. M. Guyon, and V. N. Vapnik, "A training algorithm for optimal margin classifiers," in *Proceedings of the Fifth Annual Workshop on Computational Learning Theory*, pp. 144–152, ACM, 1992.

[200] L. Bottou, C. Cortes, J. S. Denker, H. Drucker, I. Guyon, L. D. Jackel, Y. LeCun, U. A. Muller, E. Sackinger, P. Simard, *et al.*, "Comparison of classifier methods: a case study in handwritten digit recognition," in *International Conference on Pattern Recognition*, pp. 77–77, IEEE Computer Society Press, 1994.

[201] V. Vapnik, *The nature of statistical learning theory*. Berlin, DE: Springer Science & Business Media, 2013.

[202] A. Aizerman, E. M. Braverman, and L. Rozoner, "Theoretical foundations of the potential function method in pattern recognition learning," *Automation and Remote Control*, vol. 25, pp. 821–837, 1964.

[203] T. M. Cover, "Geometrical and statistical properties of systems of linear inequalities with applications in pattern recognition," *IEEE Transactions on Electronic Computers*, no. 3, pp. 326–334, 1965.

[204] K. Pearson, "On lines and planes of closest fit to system of points in space. philiosophical magazine, 2, 559-572," 1901.

[205] H. Hotelling, "Analysis of a complex of statistical variables into principal components.," *Journal of Educational Psychology*, vol. 24, no. 6, p. 417, 1933.

[206] B. A. Olshausen and D. J. Field, "Sparse coding with an overcomplete basis set: A strategy employed by v1?," *Vision research*, vol. 37, no. 23, pp. 3311–3325, 1997.

[207] D. L. Donoho, "Compressed sensing," *Information Theory, IEEE Transactions on*, vol. 52, no. 4, pp. 1289–1306, 2006.

[208] J. Wright, A. Y. Yang, A. Ganesh, S. S. Sastry, and Y. Ma, "Robust face recognition via sparse representation," *Pattern Analysis and Machine Intelligence, IEEE Transactions on*, vol. 31, no. 2, pp. 210–227, 2009.

[209] B. Schölkopf, A. Smola, and K.-R. Müller, "Nonlinear component analysis as a kernel eigenvalue problem," *Neural Computation*, vol. 10, no. 5, pp. 1299–1319, 1998.

[210] S. Mika, B. Schölkopf, A. J. Smola, K.-R. Müller, M. Scholz, and G. Rätsch, "Kernel PCA and de-noising in feature spaces.," in *Advances in Neural Information Processing Systems*, vol. 4, p. 7, Citeseer, 1998.

[211] J. B. Tenenbaum, V. De Silva, and J. C. Langford, "A global geometric framework for nonlinear dimensionality reduction," *Science*, vol. 290, no. 5500, pp. 2319–2323, 2000.

[212] D. L. Donoho and C. Grimes, "Hessian eigenmaps: Locally linear embedding techniques for high-dimensional data," *Proceedings of the National Academy of Sciences*, vol. 100, no. 10, pp. 5591–5596, 2003.

[213] M. Belkin and P. Niyogi, "Laplacian eigenmaps for dimensionality reduction and data representation," *Neural Computation*, vol. 15, no. 6, pp. 1373–1396, 2003.

[214] Y. Bengio, "Learning deep architectures for AI," *Foundations and Trends in Machine Learning*, vol. 2, no. 1, pp. 1–127, 2009.

[215] G. E. Hinton and R. R. Salakhutdinov, "Reducing the dimensionality of data with neural networks," *Science*, vol. 313, no. 5786, pp. 504–507, 2006.

[216] G. Baudat and F. Anouar, "Generalized discriminant analysis using a kernel approach," *Neural Computation*, vol. 12, no. 10, pp. 2385–2404, 2000.

[217] K. Fukumizu, F. R. Bach, and M. I. Jordan, "Dimensionality reduction for supervised learning with reproducing kernel Hilbert spaces," *The Journal of Machine Learning Research*, vol. 5, pp. 73–99, 2004.

[218] R. Raina, Y. Shen, A. Mccallum, and A. Y. Ng, "Classification with hybrid generative/discriminative models," in *Advances in Neural Information Processing Systems*, p. None, 2003.

[219] J. Lasserre, C. M. Bishop, T. P. Minka, *et al.*, "Principled hybrids of generative and discriminative models," in *Computer Vision and Pattern Recognition, 2006 IEEE Computer Society Conference on*, vol. 1, pp. 87–94, IEEE, 2006.

[220] A. Bosch, A. Zisserman, and X. Muoz, "Scene classification using a hybrid generative/discriminative approach," *IEEE Transactions on Pattern Analysis and Machine Intelligence*, vol. 30, no. 4, pp. 712–727, 2008.

[221] H. Abdi, "Partial least square regression (PLS regression)," *Encyclopedia for Research Methods For the Social Sciences*, pp. 792–795, 2003.

[222] Y. Guo, T. Hastie, and R. Tibshirani, "Regularized linear discriminant analysis and its application in microarrays," *Biostatistics*, vol. 8, no. 1, pp. 86–100, 2007.

[223] Y. Ou, A. Sotiras, N. Paragios, and C. Davatzikos, "DRAMMS: Deformable registration via attribute matching and mutual-saliency weighting," *Medical Image Analysis*, vol. 15, no. 4, pp. 622–639, 2011.

[224] S. Subramony, W. May, D. Lynch, C. Gomez, K. Fischbeck, M. Hallett, P. Taylor, R. Wilson, T. Ashizawa, and for the Cooperative Ataxia Group, "Measuring friedreich ataxia: interrater reliability of a neurologic rating scale," *Neurology*, vol. 64, no. 7, pp. 1261–1262, 2005.

[225] H. E. Hooper, "The Hooper Visual Organization Test," *Western Psychological Services: Beverley Hills, CA*, 1963.

List of Publications

- Journal articles

    1. **Zhen Yang**, Chuyang Ye, John A. Bogovic, Aaron Carass, Bruno M. Jedynake, Sarah H. Ying, Jerry L. Prince. Automated Cerebellar Lobule Segmentation with Application to Cerebellar Structural Analysis in Cerebellar Disease. Neuroimage, accepted.
    2. Mao Ye, Henry M. Sanchez, Margot Hultz, **Zhen Yang**, Max Bogorad, Andrew D. Wong, and Peter C. Searson. Brain microvascular endothelial cells resist elongation due to curvature and shear stress. Scientific reports 4 (2014).
    3. Chuyang Ye, **Zhen Yang**, Sarah H. Ying, and Jerry L. Prince. Segmentation of the Cerebellar Peduncles Using a Random Forest Classifier and a Multi-object Geometric Deformable Model: Application to Spinocerebellar Ataxia Type 6. Neuroinformatics (2015): 1-15.
    4. Bennett A. Landman, John A. Bogovic, Aaron Carass, Min Chen, Snehashis Roy, Navid Shiee, **Zhen Yang** et al. "System for integrated neuroimaging analysis and processing of structure." Neuroinformatics 11, no. 1 (2013): 91-103.

- Conference and workshop papers

    1. **Zhen Yang**, S. Mazdak Abulnaga, Aaron Carass, Kalyani Kansal, Bruno M. Jedynak, Chiadi Onyike, Sarah H. Ying and Jerry L. Prince. Landmark Based Shape Analysis for Cerebellar Ataxia Classification and Cerebellar Atrophy Pattern Visualization. SPIE medical imaging, International Society for Optics and Photonics, 2016, submitted.
    2. **Zhen Yang**, Shenghua Zhong, Aaron Carass, Sarah H. Ying, and Jerry L. Prince. Deep Learning for Cerebellar Ataxia Classification and Functional

Score Regression. In Machine Learning in Medical Imaging, pp. 68-76. Springer International Publishing, 2014.

3. **Zhen Yang**, John A. Bogovic, Chuyang Ye, Aaron Carass, Bruno M. Jedynake, Sarah H. Ying, Jerry L. Prince. Automated cerebellar lobule segmentation using graph cuts, MICCAI Challenge Workshop on Segmentation: Algorithms, Theory and Applications, 2013.

4. **Zhen Yang**, John A. Bogovic, Aaron Carass, Mao Ye, Peter C. Searson, and Jerry L. Prince. Automatic cell segmentation in fluorescence images of confluent cell monolayers using multi-object geometric deformable model. In SPIE Medical Imaging, pp. 866904-866904. International Society for Optics and Photonics, 2013.

5. **Zhen Yang**, Aaron Carass, and Jerry L. Prince. Covariance shrinking in active shape models with application to gyral labeling of the cerebral cortex. In Biomedical Imaging (ISBI), 2013 IEEE 10th International Symposium on, pp. 1018-1021. IEEE, 2013.

6. **Zhen Yang**, Aaron Carass, Chen Chen, and Jerry L. Prince. Simultaneous cortical surface labeling and sulcal curve extraction. In SPIE Medical Imaging, pp. 831414-831414. International Society for Optics and Photonics, 2012.

Vita

Zhen Yang was born in Wuhan, Hubei, China. She received the B.S. degree in Optoelectronics Information Engineering and M.S. degree in Optical Engineering both from Beijing University of Aeronautics and Astronautics, Beijing, China. She is currently pursuing the Ph.D. degree in Electrical and Computer Engineering at The Johns Hopkins University. Her research interests include computer vision and medical image analysis.